Validation of Ice Cloud Optical Thickness Retrievals during CAMP2EX and PISTON using the UW-HSRL

Terence J. Pagano

A thesis submitted in partial fulfillment of

the requirements for the degree of

Master of Science

(Atmospheric and Oceanic Sciences)

at the

UNIVERSITY OF WISCONSIN – MADISON

May 2023

Approved by: _____ 05/09/2023
Robert Holz Date

Senior Scientist in the Space Science and Engineering Center (SSEC)

Approved by: _____ 9 May, 2023
Tristan L'Ecuyer Date

Professor of Atmospheric and Oceanic Sciences
Director of Cooperative Institute for Meteorological Satellite Studies (CIMSS)

Approved by: _____ 9 May 2023
Angela Rowe Date

Assistant Professor of Atmospheric and Oceanic Sciences

Table of Contents

List of Figures

List of Tables

1. Introduction

Ice clouds play an important role in the modulation of Earth's upper tropospheric and overall radiation budget. They can vary in their ice crystal morphology (habit) based on temperature, moisture, and other characteristics in the developmental life cycle of the cloud (Heymsfield et al. 2017). Ice clouds also have different radiative effects on the global climate depending on the physical characteristics of the cloud such as optical thickness and cloud top height. Optically thin ice clouds generally have an overall warming effect because the absorption of outgoing longwave radiation is larger than the cooling effect due to the reflection of incoming solar radiation. In contrast, optically thicker ice clouds generally have a larger shortwave reflectance component than longwave absorption. The International Commission on Clouds and Precipitation Commission states that we currently have an overall lack of understanding in how ice clouds' geographic distribution, properties, lifetimes, and cloud top heights will respond to anthropogenic climate change (ICCP, 2021).

Ice clouds also remain one of the more difficult components to represent in global climate models making accurate long-term satellite observation records of these parameters important for understanding climate change-related feedbacks. A misrepresentation of ice clouds in global climate models can lead to errors in climate and weather forecasting and is a source of uncertainty for climate change projections (Waliser *et al.*, 2009). Furthermore, observational data records on the order of three decades or more are required for accessing climate change signals in clouds (Wielicki *et al.*, 2013), highlighting the importance of inter-satellite data records.

Ice cloud optical thickness (IOT) is an especially important parameter for understanding the radiative impact of thin cirrus, however, it is a challenging parameter to retrieve from passive satellite instruments due to their extensive spatial scales, retrieval assumptions, and opaqueness.

Visible imagers must account for the scattering properties of the cloud as well as the reflective properties of the underlying surface to obtain an IOT measurement. Infrared radiometers must consider the height of the cloud as well as the emissive properties of the underlying surface. A historical lack of direct in-situ measurements motivates a validation and examination of the accuracy of passive IOT retrieved products. Recent advancements in geo-stationary earth orbit (GEO) capabilities with the launch of next generation imagers such as the Advanced Baseline Imager (ABI) and the Japanese Advanced Himawari Imager (AHI) provide new opportunities to leverage ground-based measurements due to greatly increased sampling over individual ground-based data collection sites within the field of view of the GEO satellite compared to individual low earth orbit (LEO) satellites. The geostationary spectroradiometers' advantage of increased sampling over individual validation sites is advantageous for validating satellite retrievals of cloud properties and obtaining a better understanding how they can be improved.

The goal of this thesis is to create an ice cloud property retrieval for the HSRL with uncertainty estimates to validate two inter-satellite IOT retrieval algorithms processed on AHI; the NASA Cloud Property Algorithm (NASA CLDPROP) and NOAA Enterprise IOT retrievals as well as examine the validity of some of the retrieval assumptions. To accomplish this goal, we utilize data collected by the University of Wisconsin High Spectral Resolution Lidar (HSRL) during the Cloud-Aerosol and Monsoon Process Philippines Experiment (CAMP2EX) (Reid *et al.*, 2023) in Manila, Philippines and the Propagation of Intra-Seasonal Tropical Oscillations (PISTON) (Sobel *et al.*, 2021) mission in the Philippines Sea and the resources of the Science Investigator-led Processing System (SIPS) to process the cloud retrieval algorithms on AHI. The data collected by the HSRL during the PISTON campaign provides a unique over-ocean dataset that can be used in conjunction with the CAMP2EX urban dataset to examine the validity of the

assumptions in the retrieval pertaining to the ice scattering models as well as the surface independently. We then expand on the HSRL-AHI validation results by comparing the NASA CLDPROP retrieval processed on AHI during the CAMP2EX and PISTON campaigns to co-located MODIS and VIIRS CLDPROP IOT CLDPROP observations in the PISTON domain. The AHI-MODIS-VIIRS comparison will then be used to examine if the HSRL-AHI validation effort can be translated to MODIS and VIIRS. To summarize, the objectives and goals of this work are as follows 1) Develop an HSRL ice cloud optical thickness retrieval. 2) Validate the NASA CLDPROP and NOAA Enterprise ice cloud optical thickness retrievals processed on AHI with the HSRL ice cloud optical thickness retrieval and examine the validity of the ice scattering and surface assumptions in the retrieval. 3) Compare the HSRL-validated NASA CLDPROP retrieval processed on AHI to the NASA CLDPROP retrieval processed on MODIS and VIIRS to determine if the HSRL-based validation effort can be translated to the LEO imagers.

The order of this thesis is as follows: In section 2, we discuss the characteristics and importance of ice clouds as well as the significance of passive remote sensing cloud datasets. In section 3, we examine the Advanced Himawari Imager, provide a brief description of the physical theory behind visible and infrared cloud optical thickness retrievals as well as introduce the NASA CLDPROP and NOAA NOAA Enterprise retrievals. In section 4, we introduce the High Spectral Resolution Lidar; its advantages over traditional lidars and the methods to obtain geophysical parameters of interest such as optical thickness, backscatter cross-section, depolarization ratio and the signal to noise ratio. In section 5 we propose an ice cloud optical thickness retrieval for the HSRL specifically developed for this validation effort that enhances the dynamic range and reduces uncertainty of HSRL IOT measurements through selective vertical averaging of raw photon counts before the forward model inversion process. The HSRL

IOT retrieval also includes uncertainty quantification using a Poisson bootstrapping methodology. In section 6, the constructed HSRL IOT retrieval is used to validate the two operational NASA and NOAA optical thickness products over an oceanic and urban environment. The thesis is concluded in section 7 with a discussion and conclusion.

The order of this thesis is as follows: In section 2, we present the necessary background information to understand why this research is important. The 2.1 subsection briefly describes the distribution of ice clouds on this planet as well as their diversity in terms of optical thickness, microphysical properties and radiative impacts. The above considerations are important because the HSRL's dynamic range limitation and fixed regional position in this study result in a specific subset of ice clouds being considered for retrieval evaluation. Without directly validating the full diversity spectrum of ice clouds with different microphysical properties and optical thickness values, it is unclear how the results in this thesis would translate to ice clouds excluded from this dataset. Section 2.1 also introduces the significance of long-term satellite observations as well as a brief history of the instruments providing inter-satellite data records. The construction of inter-satellite data records such as that of the NASA CLDPROP and NOAA Enterprise products motivates the validation of these retrieval algorithms. Section 2.2 introduces the Advanced Himawari Imager, a simplification of its optical design and data collection system as well as the recent advancements in geostationary spectroradiometer technology. The recent advancements in GEO technology such as an on-board calibrator and improvements in the number and position of its spectral channels facilitate the ability to accurately run stable inter-satellite cloud optical property retrieval algorithms such as NASA CLDPROP and NOAA Enterprise on AHI for retrieval evaluation.

Section 2.3 and 2.4 provide a brief theoretical description of the visible (NASA CLDPROP and NOAA Entperise visible) and infrared (NOAA Entperise infrared) retrievals used in this thesis with a focus on the assumptions within each retrieval as well as the methodology employed. The purpose of these sections is to provide a foundation to understand how we are able to make conclusions about specific retrieval assumptions in the results section of this paper (section 4). Section 2.5 introduces the UW-HSRL and describes why this instrument is currently the best in-situ lidar for measuring ice cloud optical thickness. Section 2.6 introduces the CAMP2EX and PISTON field campaigns. The section also outlines the validation methodology and why the HSRL is the best available tool to construct this comparison.

Section 3 is the methods section. Section 3.1 described the HSRL ice cloud optical thickness retrieval developed specifically for this study. It goes over the technique used to calibrate the HSRL data (section 3.1.1) and the forward model equations implemented in the retrieval (section 3.1.2). The section also outlines the algorithm used to retrieve an IOT measurement developed specifically for this study (section 3.1.3) and the methodology for estimating the uncertainty of those IOT measurements (section 3.1.4). Section 3.2 outlines the co-location of the AHI pixels with the ground-based HSRL and the quality control performed on both the NASA CLDPROP and NOAA enterprise products as well as on the HSRL ice cloud optical thickness retrieval.

Section 4 shows the results of this thesis. The first major subsection (4.1) outlines the evaluation of the NASA CLDPROP and NOAA Enterprise (visible and infrared) retrievals processed on AHI by the HSRL ice cloud optical thickness retrieval during the CAMP2EX and PISTON field campaigns. The retrieval algorithms assumptions are investigated relating ice scattering model used as well as the surface assumption employed. This is performed by the

approach outlined in section 2.6.2. The second section (4.2) uses the validation results in section 4.1 and determines if the AHI based validation effort for the NASA CLDPROP retrieval can be transferred to the same retrieval processed on MODIS and VIIRS. The thesis is concluded with summary and conclusions.

2. Background

2.1 Characteristics of Ice Clouds

2.1.1 Distribution and Climatology

In this section, we examine the physical climatology of ice clouds to show the frequency of ice clouds examined in the GEO-LEO comparison (full range of IOT) in section 4.2 as well as the subset of ice clouds validated by the HSRL (cirrus) in section 4.1. The reasoning for examining the climatology of ice clouds and their optical thickness frequencies are for the following reasons. 1) Provide an introduction to ice clouds and their global climatology, 2) contextualize their frequency in the validated region, 3) introduce how optical thickness impacts the ice cloud radiative effects and 4) examine the subset of ice clouds to be validated (within the dynamic range of the HSRL) and their radiative effects.

There are several works of literature that report different global ice cloud frequencies. These statistics are variable based on the optical thickness ranges, instrument/dataset sensitivities, and filtering criteria, as well as the metric in which they are reported (e.g. percentage reported relative to all sky conditions or percentage reported relative to cloudy conditions). One of the most effective methods for detecting ice clouds, especially cirrus, is by using an active lidar such as the Cloud-Aerosol LIDAR and Infrared Pathfinder Satellite

Observations (CALIPSO) (Sassen, Wang and Liu, 2008). Sassen et al. 2008 were the first to derive the global frequency distribution of cirrus clouds based on combined active CALIPSO and CloudSAT measurements. Using a variety of threshold conditions aimed at isolating only cirrus clouds (IOT < 3) as would be visible from a surface observer (i.e., multi-layered ice over water clouds not considered), they determined a global cirrus cloud frequency of 16.7%. Hong et al. 2015 estimated the global ice cloud frequency using the CloudSat Data Processing Center and radar/lidar product (DARDAR) measurements over a broad range of optical depth values for all ice clouds and found the frequency to be 53% for all clear and cloudy pixels globally. The

frequency of occurrence of all ice clouds is shown in Figure 1.

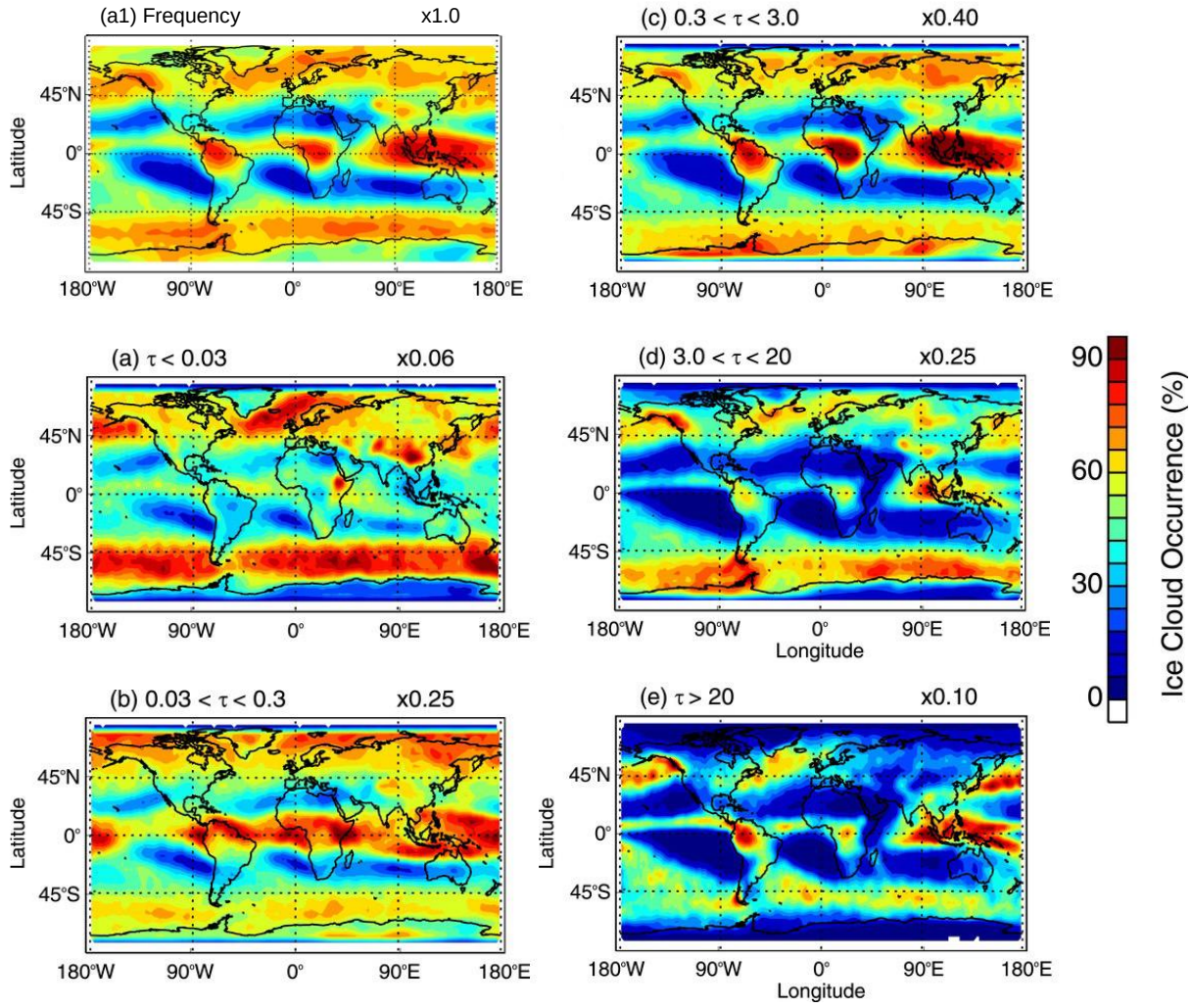

Figure 1- The frequency distribution of ice clouds by optical thickness(τ). The weighted frequency (ex: 0.06 for (a)) relative to the total frequency (ex: (1) for (a1)) (Adapted from Hong et al. 2015)

It can be observed that large ice cloud frequency of occurrence is associated with climate regimes; for example, in the tropics, they are prevalent due to deep convection from the Inter-Tropical Convergence Zone (ITCZ) and/or monsoonal activity. Examples of locations that experience deep convection as described above include the Pacific warm pool as well as the

Congo and Amazon basins. Ice clouds are also common in the mid-latitudes over the Southern Ocean in the southern hemisphere and the North Pacific and Atlantic in the northern hemisphere. Ice clouds are less common in the eastern portion of the southern hemisphere oceanic basins and regions of midlatitude upwelling. Vertically, ice clouds are commonly found above 10 km in the tropics and as low as 5 km in the mid-latitudes. The validation region in this study as will be outlined in section 2.6.1 is over the western Pacific near southeast Asia and over the maritime continent. The frequency of ice clouds in that region is very high approximately 85% by the look of Figure 1a. The study of Matus et al. 2016 further showed using combined CloudSAT/CALIPSO measurements that this region has some of the highest frequencies of multi-layered scenes on the planet, with multi-layer cloud scenes being as high as 50% in the region (Matus and L'Ecuyer, 2017).

Although ice cloud frequency is an important metric, the ice cloud property such as ice cloud optical thickness is an important parameter for determining ice cloud radiative effects. The optical thickness and distribution of clouds are also important for regional heating rates. For this study, we are mostly concerned with ice clouds within the dynamic range of our HSRL observations (Max τ < ~1.5), however, we do compare a larger range of optical thickness values in the GEO-LEO comparison in section 4.2. The global distribution of optical thickness values in the Hong et al. 2015 study are shown in Figure 1a-e. The overall distribution of ice cloud optical thickness is skewed towards optically thinner clouds, with approximately 79% having an optical thickness less than 3.0 and 40% having an optical thickness less than 0.3. Thin ice clouds (Figure 1b; τ ~ 0.03-0.3) are uniformly distributed over the tropics and are also present in northern hemisphere polar regions. Opaque ice clouds (Figure 1c; τ ~ 0.3 - 3) are the most common group and have high occurrence in convective regions such as the Pacific warm pool and over large

forest basins. Optically thicker ice clouds (Figure 1d; $\tau \sim 3 - 20$) are most prevalent over mid-latitude terrestrial surfaces and the Southern Ocean while the optically thickest group (Figure 1e; $\tau > 20$) occurs in regions of deep convection, mid-latitude storm tracks, and the Southern Ocean.

The distribution and optical thickness characteristics displayed in the above climatology figures combined with the dynamic range of the HSRL stress that a specific subset of ice clouds are being considered for retrieval evaluation. In regards to the region of interest for this study (west pacific and Southeast Asia), these are all thin and most opaque ice clouds. Without directly validating the full diversity spectrum of ice clouds with different microphysical properties and optical thickness values, it is unclear how the results in this thesis would translate to ice clouds excluded from this dataset. In the next section, we will examine the variety of different microphysical properties of ice clouds and state why the microphysical properties of the ice cloud are important.

2.1.2 Microphysical Properties

As the name implies, ice clouds are composed of ice particles which can take on a variety of shapes, sizes, orientation, and surface textures. The ice crystal morphology in turn influences the single scattering properties of a cloud, especially at the solar wavelengths and is important in determining its radiative effect along with other cloud macrophysical properties (Fu, 2007; Stephens *et al.*, 1990; Zhang, Macke and Albers, 1999). There have been many modeling, observational and laboratory studies investigating ice crystal morphology as well as the formation parameters and magnitudes that ultimately determine them. (Bailey and Hallett, 2009) were able to bring their laboratory results into an agreement with direct observations from a Cloud Particle Imager that images the ice crystals directly from aircraft and allows for later

categorization by shape and size by manual or automated methods (Xiao *et al.*, 2019). Figure 2 (Bailey and Hallett 2008), shows the impact of temperature and super saturation on ice crystal

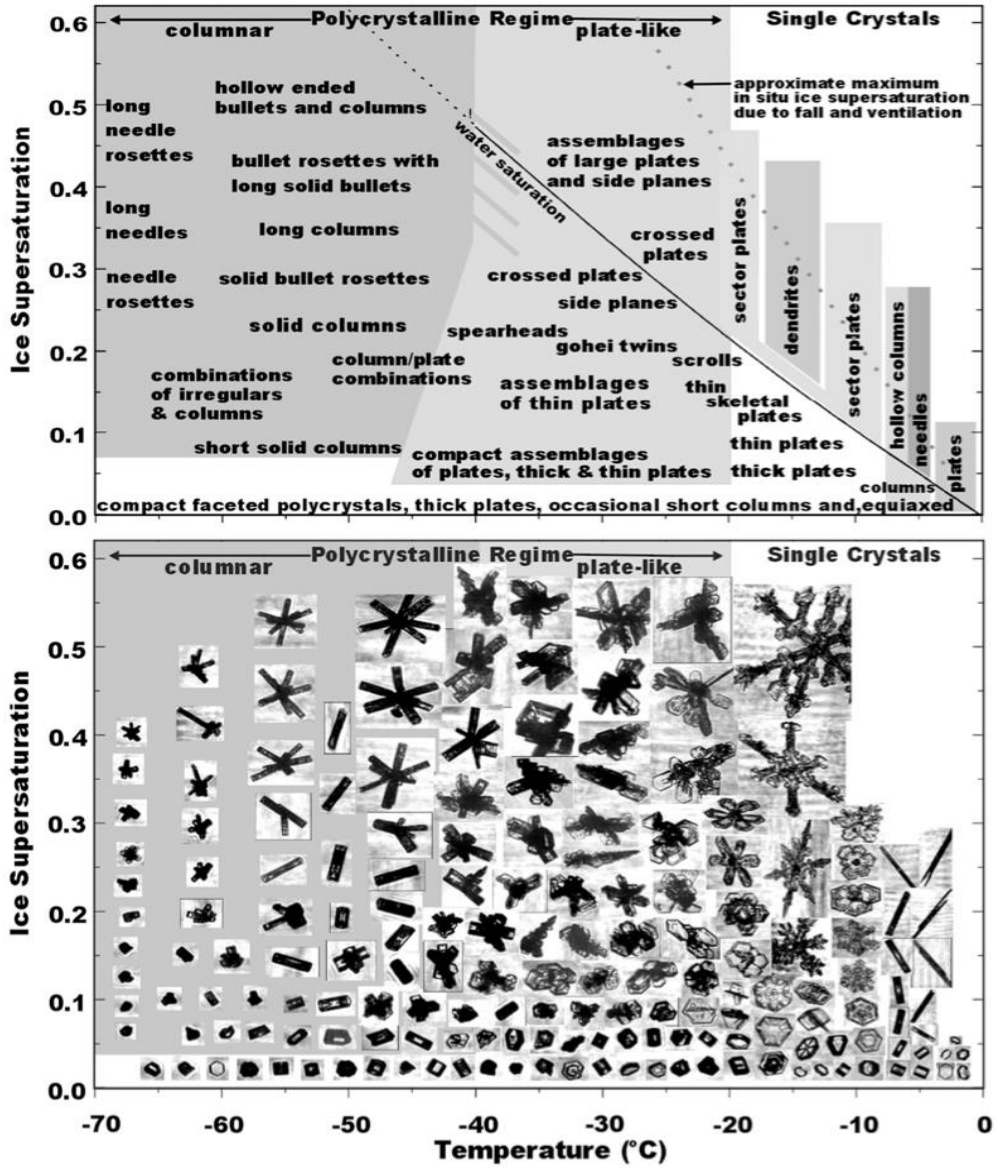

Figure 2 -Ice cystal morphology variation by temperature and super-saturation from (Bailey and Hallet 2008)

habit from laboratory studies. It is evident from the figure that there is a large variety of size and shapes of ice crystals that could be contained within an ice cloud, many of which are irregular. Furthermore, there may be inter-cloud ice crystal variability stratified by height, with the crystals near the cloud top being on the order of 10 um and crystals near the base being on the order of

thousands of microns (Baran, 2012). Despite the many irregularities, there appears to be distinct regimes within the diagram such as columnar crystals at very cold temperatures (~ - 60 C) and singular crystals at warmer temperatures and higher ice saturation. Nevertheless, as the habit of the ice cloud has a profound effect on the scattering phase function it is of utmost importance for radiation budget applications and passive cloud optical thickness retrievals, such as those in the visible and infrared, to correctly approximate the scattering associated with the ice crystal morphology.

2.1.3 Radiative Importance

Ice clouds have competing warming and cooling effects due to their reflection of solar radiation and the absorption of terrestrial radiation (Stephens *et al.*, 1990; Liou, 1986). The properties of the cloud such as cloud top height, optical thickness as well as the microphysical properties are important parameters for estimating their radiative effect. Using the passive Moderate Resolution Imaging Spectroradiometer (MODIS) and Atmospheric Infrared Sounder (AIRS) data in conjunction with a radiative transfer model, it was determined that thin tropical oceanic cirrus (optical depths between 0.02-0.3) have a net radiative forcing at the top of the atmosphere (TOA) between 0-20 Wm^{-2}, with the radiative forcing increasing semi-linearly with optical depth in that range (Lee *et al.*, 2009). More recently a larger spectr um of optical depth (0.01 - ~100) values were analyzed for the year of 2008 using combined CALIPSO/CloudSAT measurements as inputs into a radiative transfer model and were shown to have a net warming of ~5.1 +/- 3.8Wm^{-2} (Hong, Liu and Li, 2016). Figure 3 is borrowed from Hong et al. 2016 to show the significance of optical depth on ice cloud radiative effect.

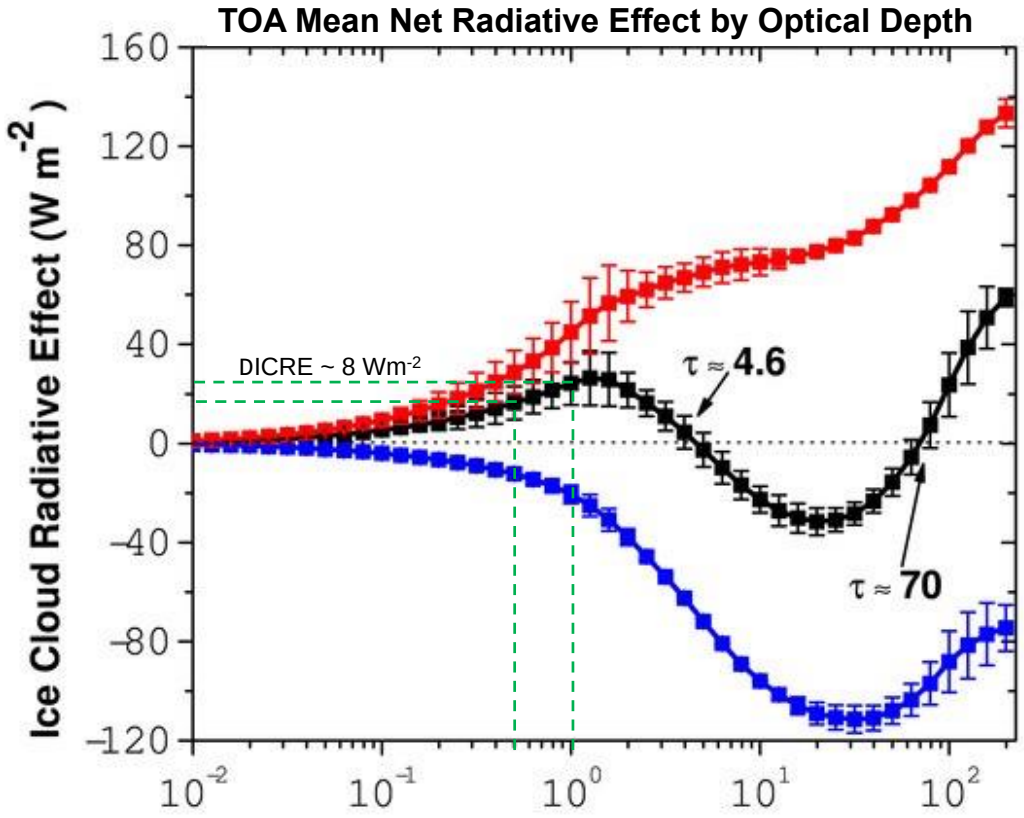

Figure 3- Radiative Effect of Ice Clouds by Optical Thickness (Hong et al. 2016). The redline is the longwave warming effect, the blue is the shortwave cooling effect and the black line is the net radiative effect. The green dashed lines overlayed on the authors figure shows the mean difference in radiative forcing between 0.5 and 1 optical depth units.

Ice clouds with $\tau < 4.6$ have a warming effect, with the largest warming contribution coming from $\tau \sim 1.2$. Of significance is the increase in slope of the longwave warming component relative to the shortwave cooling between optical depths from about ~ 0.2 – 1.1, which results in the peak of the warming contribution. Previous studies such as Holz et al. 2016 have shown visible retrieved optical depths, such as from the MODIS C5 retrieval, can have biases on the order of 2:1 relative to the CALIPSO unconstrained retrieval. By the results of Hong et al. 2016, the 2:1 bias would result in approximately a ~8Wm^{-2} disagreement in net ice cloud radiative forcing between the two products if the MODIS retrieved IOT was 1 and the unconstrained

CALIPSO IOT was 0.5. It should however be mentioned that this is a mean approximation based on the figure and when the error bars are considered the uncertainty is larger than the disagreement (~14W/m^2), meaning they are within the bounds of uncertainty for this optical depth. In addition, optical depth does not soley control radiative forcing and cloud altitude would also play a role in the radiative forcing of the cloud. This disagreement highlights the need to independently validate individual optical thickness products so they can be used to accurately quantify cloud radiative effects. Of particular importance are bringing legacy sensors that utilize visible channels for cloud property retrievals into an agreement with a validation standard such as the HSRL to enable the construct of accurate long-term climate data records.

2.1.4 Significance of Satellite Observed Ice Cloud Optical Thickness Products

The representation of ice clouds in global climate models (GCMs) are crucial for climate and weather forecasting as well as climate change projections (Waliser *et al.*, 2009; Liou *et al.*, 2008). However, ice clouds are one of the more difficult components to represent in GCMs (Jiang *et al.*, 2012). Currently, ice cloud mass is underestimated in climate models relative to observations (Waliser *et al.*, 2009) and GCM future simulations of ice clouds are not automatically applicable to the real climate system (Cesana and Storelvmo, 2017). Determining historical and future trends in the magnitude of ice cloud radiative effect which is related to regional and global cloud cover, cloud height, and cloud optical thickness is an important factor for climate sensitivity studies and the potential change of ice clouds can contribute to the sensitivity of our planet to increased warming due to greenhouse gasses. Due to the current deficiencies in GCM future simulations, historical and future remote sensing observations are crucial datasets to answer questions related to changes in ice cloud radiative impact.

Passive low earth orbit instruments have a long history of cloud remote sensing. The Advanced Very High-Resolution Radiometer (AVHRR) has been part of the NOAA satellite series going back to NOAA-1 in 1979, with last AVHRR launch taking place in 2019. The radiometer was designed for cloud top and surface temperatures as well as imaging applications. It has a visible channel at 0.64 um, as well as an 11- um surface window channel. The AVHRR however, has several disadvantages such as a limited n umber of channels, poor spectral resolution, and course spatial resolution. Furthermore, AVHRR relied on scene-based calibration methods (Nagaraja Rao and Chen, 1995; Vermote and Kaufman, 1995; Heidinger, Sullivan and Rao, 2003) which can result in large discrepancies between instruments for derived cloud products (Heidinger, Cao and Sullivan, 2002). In 1999, the TERRA MODIS instrument (Pagano *et al.*, 1996a; Barnes, Pagano and Salomonson, 1998; Pagano *et al.*, 1996b) launched from the Vandenburg Air Force Base in southern California ushering in a new age of passive cloud remote sensing. The launch of MODIS on TERRA was followed by a second MODIS instrument in 2002 on board the Aqua spacecraft. The MODIS instrument is capable of preforming the bi-spectral reflectance method (Nakajima and King, 1989) as it also has a 2.15 um channel that provides sensitivity to cloud particle size. The bi-spectral reflectance method will be described in more detail in section 2.3.1. In addition, it contains a variety of channels that provide other spectral information for cloud masking and cloud top height. The most important advancement for MODIS over AVHRR is the on-board calibrator, which contains a solar diffuser stability monitor, a blackbody and a spectral radiometric calibration assembly which all allow for the postlaunch implementation of radiometric calibration algorithms (Pagano *et al.*, 1996a). The two MODIS instruments have been providing high quality stable cloud products for over two decades as of the writing of this doc ument. However, to observe climate change feedbacks and trends

related to clouds, observations on the order of three decades or more are required (Wielicki *et al.*, 2013).

In 2011, NOAA committed to a new passive cloud imager, the Visible Infrared Imaging Suite (VIIRS) (Johnson *et al.*, 2010). Although the VIIRS instrument was an advancement over the already decade old MODIS instrument in many ways, such as having a higher spatial resolution, VIIRS lacked key spectral channels and had slightly different positions of other spectral channels utilized in the MODIS cloud retrieval algorithm and cloud mask. This poses challenges for creating a continuous cloud data product. One example is the CO_2 slicing channels that give sensitivity to cloud top height, as it was planned that the Cross-track Infrared Sounder (CrIS) instrument would provide additional infrared information. Another challengeis the spectral position of the 2.2 um channel in VIIRS relative to the 2.1 um channel in MODIS, due to the differential absorption of ice and water in that spectral region. The necessity to create a highly accurate inter-decadal cloud optical property record facilitated the development of the NASA MODIS-VIIRS Continuity Cloud Optical Properties Products known here after as NASA CLDPROP (Platnick *et al.*, 2021). This product aims to merge the data record of MODIS with current and future VIIRS data records. The hope is to create a data record long enough to observe climate-related changes in cloud frequency and/or optical properties. From these cloud property estimates, changes in cloud radiative effect can be determined. The NOAA Clouds from the AVHRR extended system (NOAA Enterprise) also aim to accomplish this goal. Both inter-satellite retrieval products (NASA CLDPROP and NOAA NOAA Enterprise) will be independently evaluated in this thesis using direct in-situ measurements from the HSRL deployed during the CAMP2EX and PISTON field campaigns. Unique to this study is the evaluation of the operational NASA CLDPROP and NOAA Enterprise daytime products

processed by AHI and validated by the HSRL over an extremely well-behaved surface Bidirectional reflectance distribution function (BRDF) environment: the ocean. This unique aspect enables the evaluation of retrieval assumptions such as the scattering phase function as well as the impact of different surface environments on the retrieval when compared to the over ocean measurements. The results of this evaluation will provide a snapshot into the validity of the assumptions and techniques used in the two retrieval algorithms.

2.2. Advanced Himawari Imager

2.2.1 Basic Description

The Advanced Himawari Imager (AHI) instrument on board the Himawari-8 satellite was launched on October 7th, 2013 and is a visible and infrared imager in geostationary orbit. AHI and the Advanced Baseline Imager (ABI) have heritage from the previous GEOS instruments (Schmit *et al.*, 2008; Hillger, Schmit and Daniels, 2003; Menzel *et al.*, 1998) , as well as adoption of spectral channels from the Moderate Resolution Imaging Spectroradiometer (MODIS). The Himawari-8 spacecraft's orbit altitude is at 35,786 kilometers and it is centered at 140.7 degrees longitude. It has sixteen spectral bands with a spectral range from 0.47 um to 13.3 um and has onboard calibration capabilities for all reflective and emissive bands. The spatial resolution ranges from 0.5 km for the 0.64 um channel to 2 km for the IR channels (Da, 2015). In the next section, we will take a closer look at the design and data collection system of AHI.

2.2.2 Simplified Optical Design and Data Collection

The AHI and ABI optical system consists of three major components that are used to collect observations of the earth, space and calibration targets (Kalluri *et al.*, 2018). Figure 4 from Kalluri et al. 2018 displays these components.

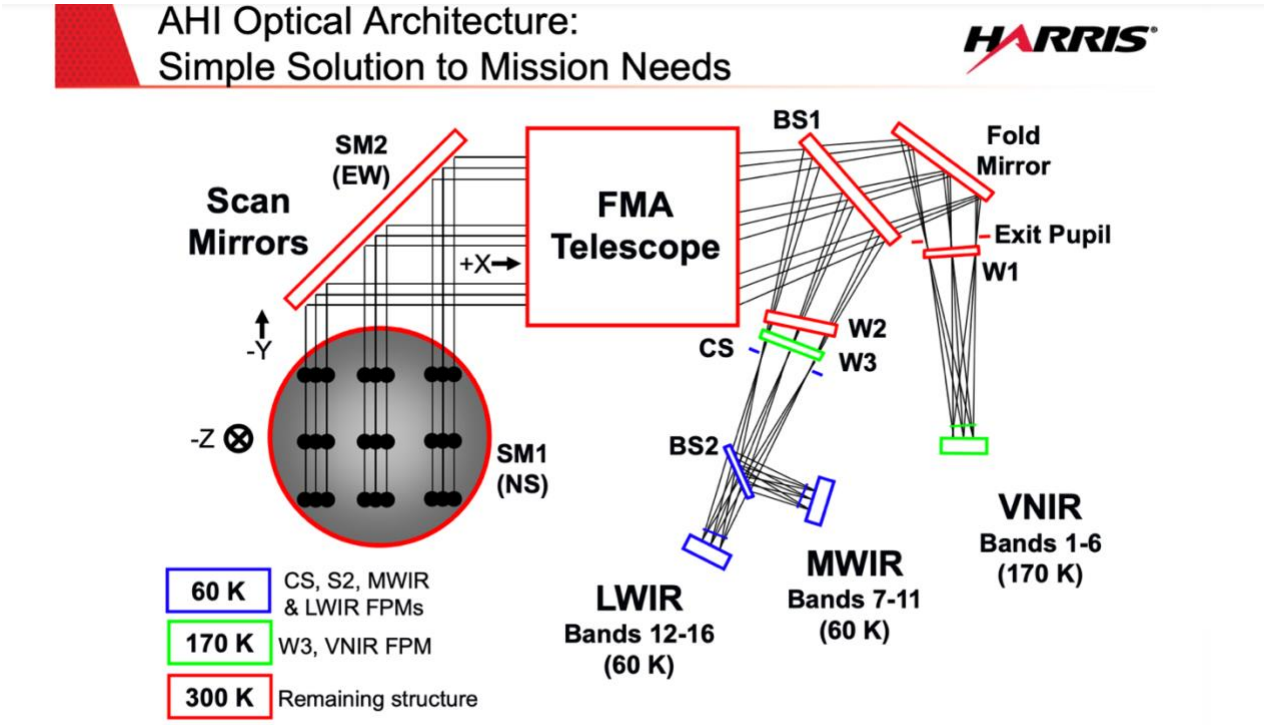

Figure 4- Simplified design of the AHI data collection system (Kalluri et al. 2018)

The first are two scan mirrors that operate independently and that control the north-south and east-west line of sight respectively. They are responsible for performing the scans for the full disc and CONUS views. Photons collected by the two scan mirrors from the earth are sent to the second component, the four mirror anastigmat (FMA) telescope. The FMA telescope consists of four reflective mirrors that focus the energy onto the detectors and aim to reduce spherical aberrations. By using an FMA instead of a lens, chromatic aberrations are eliminated. The last major component of the system are the three focal plane modules (FPM). The outgoing photon rays from the FMA are separated by several beam splitters then passed through spectral filters and finally imaged onto three different FPMs: The Visible/Near Infrared (0.47 um – 2.25 um), mid-wave infrared (3.9 um – 8.5 um), and the longwave infrared (9.61 – 13.3 um). Each focal

plane module consists of a linear detector array; each detector corresponds to an AHI channel. When enough photons are incident on the detector, electrons are emitted (photoelectric effect) corresponding to the sensitivity of the detector. The raw signal counts determined from the emitted electrons are then converted into radiances in accordance with the calibration equations. These calibration equations are derived using two onboard calibration targets: a blackbody for the thermal bands and the solar diffuser for the reflective bands, both of which are also present in MODIS (Kalluri *et al.*, 2018). The AHI/ABI system also utilizes observations of space and lunar irradiances for calibration purposes. The radiances can then be used to determine brightness temperatures using Planck's equation. Spectral radiances can then be used to construct retrieval products, such as the NASA CLDPROP and NOAA Enterprise products. In the next section, we will outline the improvements in the number of spectral channels as well as the increase in spatial and temporal resolution.

2.2.3 Improvements Over Previous Generation Geostationary Imagers

Table 1 and 2 shows the spatial, spectral, and temporal advancement of the GEOS-16 and Himawari-8 satellite channels over previous generations of the GEOS series. The information for Himawari-8 was compiled from Japanese Meteorological Agency webpage: https://www.data.jma.go.jp/ .

GOES 12-15 Central Wavelength (um)	*GOES-16/ Himawari-8* Central Wavelength (um)	Purpose
----	0.45	Blue
0.63	0.64	Red
----	0.86	Veggie
----	1.37	Cirrus
----	1.6	Snow/Ice
----	2.2	Cloud particle size
3.9	3.9	Shortwave window
----	6.2	Upper-level water vapor
6.48	6.9	Midlevel water vapor
----	7.3	Lower-level water vapor
----	8.4	Cloud-top phase
----	9.6	Ozone
----	10.3	"Clean" longwave window
10.7	11.2	Longwave window
----	12.3	"Dirty" longwave window
13.3	13.3	CO_2 longwave

Table 1 - Comparison of spectral channels from the previous GEOS series and the AHI/GEOS 16 series

Resolution	*GOES 12-15*	*GOES-16/ Himawari-8*
Spatial (VIS / IR)	1km / 4km	0.5km / 2km
Temporal	30 mins	10 mins

Table 2 - Spatial and temporal resolution improvements from the previous GEOS series and the AHI/GEOS 16 series

The combination of the onboard calibration system and the improvements in the n umber and position of spectral channels over previous generations of GEOS series allows for MODIS and

VIIRS-like cloud optical property retrievals from geostationary orbit, such as that of the NASA CLDPROP and NOAA NOAA Enterprise algorithms. More specifically, the AHI instrument has all the spectral channels necessary to perform the bi-spectral reflectance method (0.64, 0.86 and 2.2 um) and the split window method (11.2 um and 12.3 um), both of which will be introduced in more detail in the following sections. In addition, the spatial resolution increased from 4km to 2km for the infrared channels and the temporal resolution is finer at 10 minutes relative to the previous 30-minute measurements. Collectively, these advancements facilitate the investigation of the assumptions required in cloud retrieval algorithms that have been applied consistently across geostationary and polar observations. The spectral channels and calibration of the instrument facilitate the use of these retrieval products on the GEO instruments, while the spatial and temporal resolution allow for a more precise co-location with in-situ surface-based measurements and an increase in the n umber of GEO-HSRL match ups. The HSRL on board the ship-based PISTON field campaign provides a unique opportunity to independently examine the validity of the retrieval assumptions under a well quantified surface albedo environment.

2.3 Visible Ice Cloud Optical Thickness Retrievals and Theory

2.3.1 The Bi-Spectral Reflectance Method

The bi-spectral reflectance method utilizes the relationship between reflected sunlight, cloud optical depth and the scattering properties of the cloud (Twomey and Seton, 1980). The method utilizes a visible non absorbing channel (ex: 0.64 or 0.86 um) that is a primarily a function of optical thickness and a weakly absorbing shortwave IR channel (ex: 2.25 um) that has additional sensitivity to particle size to simultaneously determine both parameters. The premise of this two channel approach is that the backscatter signature of the cloud can be described by the amount of radiation being scattered (optical thickness) and the direction in

which the radiation is scattered (effective radius) (Walther, 2013). The method was first proposed for terrestrial clouds by (Twomey and Seton, 1980) and was popularized by Nakajima and King 1989 when they applied the technique to airborne MODIS simulator data (Nakajima and King, 1989). They preformed radiative transfer calculations for water clouds with a variety of optical thickness and effective radius over different zenith angles to simulate top of the atmosphere spectral reflectance values. These spectral reflectance values for the two spectral channels of interest (one non absorbing and one weakly absorbing channel) were stored in a look up tables and compared to the observed spectral reflectance functions.

There are several retrieval assumptions that may be a potential source of uncertainty if not correctly parameterized that must be acknowledged when retrieving an IOT measurement using the bi-spectral reflectance approach. Equation 1 shows the reflectance function of a non-absorbing wavelength from King et al. 1987.

$$(1)\ R(\tau_c,\ \mu\,\mu_o,\phi) =\ R_{atm}(\tau_c,\ \mu\,\mu_o,\phi) + \frac{\boldsymbol{A_g}}{1-\boldsymbol{A_g}\overline{r_{atm}}(\tau_c)}\, t_{atm}(\tau_c,\mu)\ t_{atm,o}(\tau_c,\mu_o)$$

Where

$$R_{atm}(\tau_c,\ \mu\,\mu_o,\phi)\ = R_{\infty}(\mu\,\mu_o,\phi)\ - \frac{4K(\mu)K(\mu_o)}{3(1-g)(\tau_c+2q_o)}$$

And

$$t_{atm}(\tau_c;\mu\,\mu_o,\phi) =\ \frac{4K(\mu)K(\mu_o)}{3(1-g)(\tau_c+2q_o)}$$

The reflection function ($R(\tau_c,\ \mu\,\mu_o,\phi)$) observed at the sensor is primarily a function of the atmosphere contribution ($R_{atm}(\tau_c,\ \mu\,\mu_o,\phi)$) and the surface contribution modified by the transmission of the atmosphere. R_{atm} is primary a function of cloud optical thickness (τ_c) and

the asymmetry parameter (g), while q_0 is the extrapolation length and $K(\mu)$ is the escape function. The asymmetry parameter (g) is the first Legendre moment of a phase function, which describes the directional intensity of scattered radiation. This parameter is directly tied to ice crystal morphology; size, shape, texture, etc. If the phase function is incorrectly modeled the reflectance value observed at the sensor will correspond to an incorrect optical thickness, with higher asymmetry parameters than the true value corresponding to more forward scattering and a high bias in optical thickness relative to the true value. Thin cirrus are more sensitive to small deviations in reflectance due to surface/ocean BRDF and phase function related errors than optically opaque clouds. This can be seen in the NASA CLDPROP look up table in Figure 7 in the section 2.3.4 which describes that retrieval. The surface reflectance is the second term in Equation 1 and is largely a function of ground albedo (A_g) and the atmospheric transmission (t_{atm}). Again, the uncertainties associated with this term are largest for optically thinner clouds and smallest for optically thick clouds. As the surface reflected outgoing shortwave radiation travels through an optically thicker cloud layer the radiation will be attenuated and atmospheric transmission decreases. The larger τ_c will result in a smaller t_{atm} and a smaller overall surface reflectance contribution to the satellite observed reflectance.

In addition to the assumptions made within the retrieval for scattering or surface properties there are several other uncertainties. One such uncertainty is that large vertical inhomogeneity in ice particle size for thin cirrus can impact the determination of effective radius and optical thickness (Zhang *et al.*, 2010). Another is that the spectral dependencies of cloud heterogeneity and cloud 3-D effects can induce uncertainties in a multi-channel approach for thicker ice clouds (Fauchez *et al.*, 2018). This effect increases at higher spatial resolution; however, these are less apparent for uniform thin cirrus. Lastly, as discussed in the previous

paragraph, the surface reflectance and scattering phase function assumptions must be appropriate.

Despite uncertainties in the bi-spectral reflectance approach to solving for IOT, there are several advantages compared to other methods. The first advantage is that in contrast to lidars, the bi-spectral reflectance method has a large dynamic range and can obtain optical properties for opaque and thick ice clouds. In addition, as with all passive imagers, sampling is greatly increased compared to lidar and radar observations due to a large swath (LEO) instruments, or a full CONUS view in GEO instruments. Spaceborne visible imagers can also be cheaply manufactured allowing for numerous instruments in orbit. Lastly as discussed in previous sections, there is a large historical cloud dataset obtained from current and legacy instruments using the bi-spectral reflectance method that allow for cloud continuity studies (Platnick *et al.*, 2021; Wind *et al.*, 2021). However, radiometric consistencies between analogous channels for different instruments must be accounted for otherwise there may be differences in high ice cloud frequency and properties and uncertainties may arise (Meyer *et al.*, 2020). In the next section we will examine one of the retrieval assumptions of interest the asymmetry parameter (g) as shown in equation 1.

2.3.2 Ice Scattering Models for Retrievals

One of the major assumptions required for passive observations of ice cloud optical thickness using the bi-spectral reflectance method as well as infrared methods (although scattering is far weaker in the IR than in the visible for ice crystals) is that of the ice scattering phase function. The importance of the ice scattering phase function to account for ice crystal morphology was briefly stated at the end of the microphysical properties section. In the previous section, the

asymmetry parameter (g) represents this scattering component. Due to the impossibility of measuring the exact shape (habit), surface texture and size of all ice crystal particles within a real cloud, many studies have been conducted to better understand the single scattering properties for the purpose of more consistent retrievals. One such study by (Yang *et al.*, 2013), compared 11 crystal habits from 0.2 to 100μm with 3 different roughness for texture at random orientations using a combination of geometric models (Amsterdam Discrete Dipole Approximation, T-matrix method and Improved Geometric Optics Method) to calculate the scattering properties while incorporating the edge effect for larger particles. From these results, a library was constructed for the use of a look up table for the asymmetry pattern (g), extinction efficiency (s) and the single scattering albedo (ω) for each crystal habit. Libraries such as the one developed by Yang et al. 2013, containing the bulk scattering properties of ice crystals, are used as a look up tables to infer ice cloud optical thickness and particle size from remote sensing observations (King *et al.*, 2004; Platnick *et al.*, 2003; Platnick *et al.*, 2021; Walther, 2013). An example of the impact of ice crystal habit on the asymmetry parameter for a given effective radii at wavelengths used in the bi-spectral reflectance method is shown in Figure 5. The figure is borrowed from Holz et al. 2016, where the Yang et al. 2013 database is utilized and compares 3 ice crystal habits as well as

the previous MODIS C5 ice scattering database.

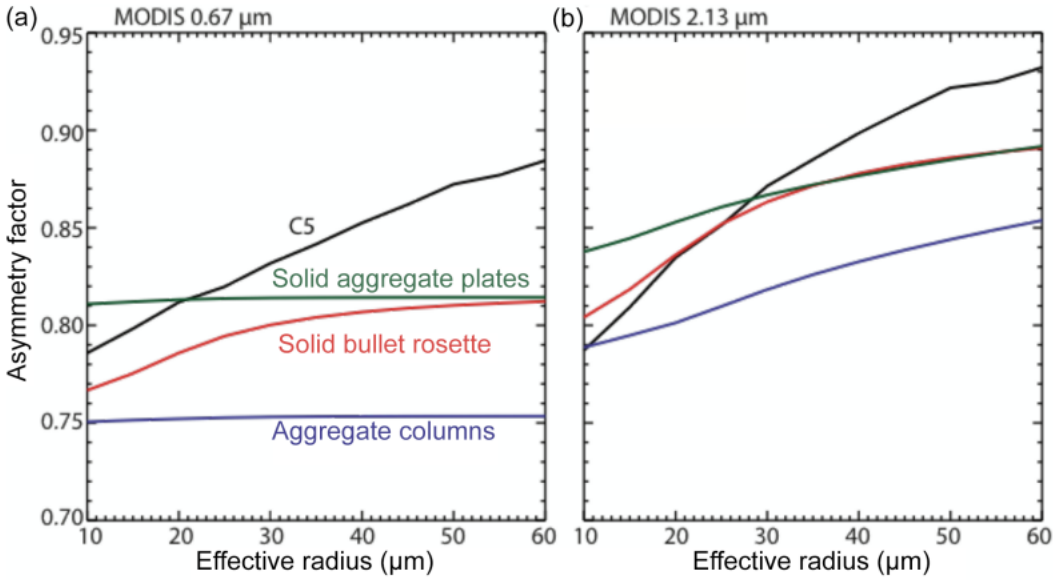

Figure 5- The sensitivity of ice crystal morphology on the asymmetry factor for the a) 0.67 um and b) 2.13 um channels (Holz *et al.*, 2016).

The figure shows different asymmetry parameters for the 3 example habits and how they vary with size and wavelength. In addition to the constructed library by Yang et al. 2013, a significant result from this study is the assumption of homogeneous severely roughened crystals outperform their smoother counterparts for reflective wavelengths. This result agrees with laboratory experimentation showing that high crystal complexity, or severe roughness, dominates the microphysics of a simulated cloud with the available vapor playing a key role in growth (Schnaiter *et al.*, 2016). Furthermore, the work of Holz et al. 2016 determined that the scattering characteristics of severely roughened aggregate columns within Yang et al. 2013 database brought the MODIS C6 visible retrievals into agreement with an infrared retrieval. The severely roughened aggregate columns from the Yang et al. 2013 database is the scattering assumption

used in the NASA CLDPROP and NOAA Enterprise visible retrievals and the validity of this assumption will be examined in the validation section (4.1) of this thesis.

2.3.3 NOAA Enterprise visible (VIS)

The NOAA Enterprise VIS retrieval utilizes an optimal estimation approach to statistically determine the optical thickness value within a given pixel. All equations and the optimal estimation approach shown in this section can be attributed to (Walther and Heidinger, 2012). The general approach is as follows: a radiative transfer model is used to simulate the top of atmosphere spectral reflectance at these channels for a variety of atmospheric conditions using the bi-spectral reflectance method. These simulated radiances and atmospheric conditions are stored in look up tables and are used as the basis for the forward model inversion during the optimal estimation process. The forward model output operator is shown in equation 2

$$(2)\quad F(x) = R_c(x) + \frac{A_v t_{atm,0}(x) t_{atm}(x)}{1 - A_v S(x)} + R_e(x)$$

Where $R_c(x)$ is the reflection function of the cloud, A_v is virtual surface albedo parameter, $t(x)$ is the transmission of the atmosphere and $S(x)$ is the albedo of the cloud. The optimal estimation iterates over the atmospheric states (x) within the look up table until the cost function criteria as shown in equation 3 is met (J < 3) and outputs the corresponding optical thickness (x).

$$(3)\quad J = [y - F(x,b)]^T S_y^{-1} [y - F(x,b)] + (x_a - x)^T S_a^{-1} (x_a - x)$$

The cost function is minimized when there is good agreement between the measured radiances (y) and the forward model output ($F(x,b)$) as well as the state vector (x) and the a priori (x_a) both weighted by the corresponding error covariance matrices (S_y and S_a). The variance between the forward model and the observation vector (S_y) is constructed by s umming up variance terms related to the parallel plane, calibration, forward model, spatial heterogeneity errors weighted by the measured reflectance in each channel and other uncertainties. S_a is the variance in the optical thickness and effective radius between the a priori and the state vector. An example of the output satellite product as observed in figure 6.

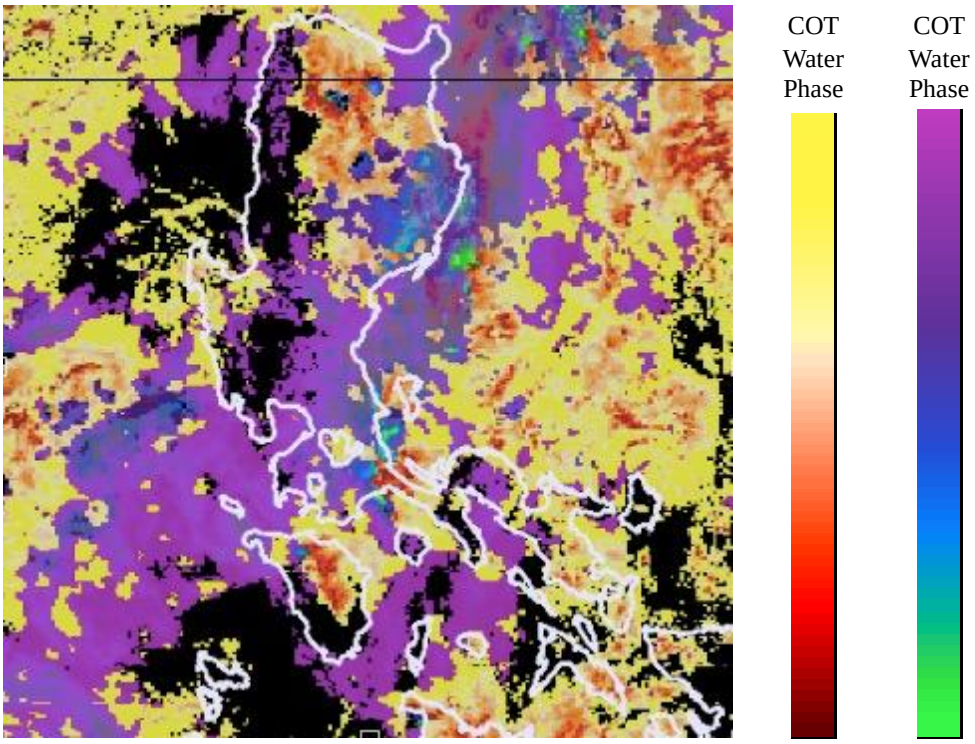

Figure 6- NOAA Enterprise visible optical depth product as observed on UW-SSEC worldview webpage for November 29th, 2019 at 23:50 UTC over the Northern Philippines.

The asymmetry parameter assumption in the NOAA Enterprise VIS retrieval is ass umed to be 0.75 globally. This value has been shown to be a globally average through an IR radiative

closure approach using MODIS and CALIOP (Holz *et al.*, 2016), polarimeter experiments using POLDER and MODIS (van Diedenhoven *et al.*, 2020) and modeling experiments (Yang *et al.*, 2013). The surface albedo assumption is also a potential source of uncertainty and is taken from the MODIS white sky albedo ancillary dataset (Schaaf et al. 2011)

2.3.4 NASA Cloud Property

The NASA CLDPROP retrieval (Platnick *et al.*, 2021) was originally designed for MODIS-VIIRS cloud continuity products and processed on AHI using the SSEC/NASA Atmosphere SIPS specifically for this CAMP2EX and PISTON validation efforts. The algorithm only utilizes analogous spectral channels common to both instruments and has a direct heritage to the MODIS optical property retrievals (MOD06 and MYD06). NASA CLDPROP uses the bi-spectral reflectance method as outlined in section 2.3.1(King, 1987; Nakajima and King, 1989; Platnick *et al.*, 2003; Walther, 2013) to simultaneously retrieve optical thickness and effective radius. The bi-spectral reflectance method in CLDPROP is implemented by first performing forward radiative transfer calculations using the discrete ordinates radiative transfer model (DISTORT) for a variety of cloudy (ice and water) atmosphere scenarios and solar/viewing geometries. From these simulations, the top of the atmosphere reflectance values convolved to the spectral response of the instrument are produced for the 0.64um (0.86um) channel over land (ocean) and the 2.2um channel. The cloud optical thickness (COT) and effective radius (CER) values as well as the resulting reflectance values from these sumulations are stored in look-up tables to determine cloud optical properties from spectral reflectance measurements. Figure 7 from Platnick et al. 2021 shows the look-up table for the VIIRS instrument on SNPP, which is more AHI than MODIS due to the spectral position of the NIR cloud-effective radius channel.

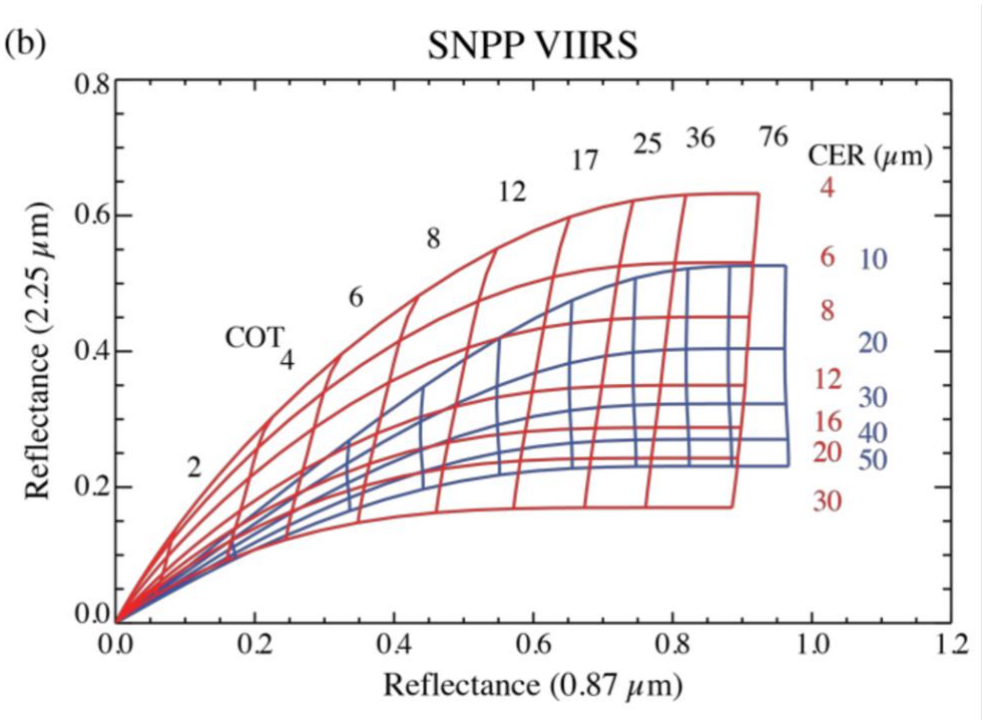

Figure 7 - NASA CLDPROP look up table for SNPP VIIRS (Platnick et al. 2021). The blue shows the solution space for ice phase, while red is the solution space for water clouds and the overlap is ambiguous.

The retrieval has a thermodynamic phase algorithm that chooses a given solution space with heritage from previous MODIS optical property retrievals (Platnick *et al.*, 2017). If the observed reflectance values by the sensor are within the solution space of the look-up table, then a corresponding cloud optical thickness and effective radius measurement are output. If the solution is not within the solution space of the lookup table, no retrieval value is given.

The retrieved optical thickness and effective radius values are dependent on the retrieval assumptions in the forward model to generate the look-up tables as well as the inputs into the retrieval. The inputs into the NASA CLDPROP algorithm for this specific processing version are the Enterprise Cloud Mask (ECM) (Heidinger, 2020) as COT and CER values are determined only for cloudy pixels, the AHI level 1-B data and NCEP GDAS for surface temperature and emissivity. The assumptions made are the surface BRDF from the white sky maps (Schaaf *et al.*,

2011), NCEP GDAS for surface temperature and emissivity, and the assumption of a single habit severely roughened aggregated columns (Yang *et al.*, 2013; Holz *et al.*, 2016), which replaced previous C5 version of the size-dependent multi-habit ice scattering model (Baum *et al.*, 2005).

2.4 Infrared Ice Cloud Optical Thickness Retrieval and Theory

2.4.1 The Split Window Method

Cloud retrieval methods utilizing the emission of infrared radiances for thin ice clouds are typically formulated as surface radiation being attenuated through a single cloud layer with a given emission temperature. The split window method is based on the differential absorption and emission of ice or water between two channels, typically a window channel (e.g., ~11 um) and a weakly absorbing (dirty window) channel (~12 um). The difference between observed brightness temperatures is then related to optical depth differences at those wavelengths with particle size sensitivity. This method was first utilized by (Inoue, 1985) to calculate cloud emissivity and temperature using AVHRR radiances and (Prabhakara *et al.*, 1988) to determine cirrus cloud optical properties from the high-resolution infrared inter-ferrometer spectrometer (IRIS) aboard the Nimbus-4 satellite. Modern applications of the split window method typically involve the use a radiative transfer model to generate top of the atmosphere radiances that can then be utilized in an optimal estimation framework to determine optical depth (Cooper, L'Ecuyer and Stephens, 2003). Figure 8a from (Stephens and Kummerow, 2007) borrowed from (Cooper, L'Ecuyer and Stephens, 2003) shows the theoretical relationship between the split window temperature difference ($\Delta T_{b} = T_{10.8\ um} - T_{12\ um}$) and the window channel ($T_{10.8\ um}$) generated using a radiative transfer model for three different cloud emitting temperatures.

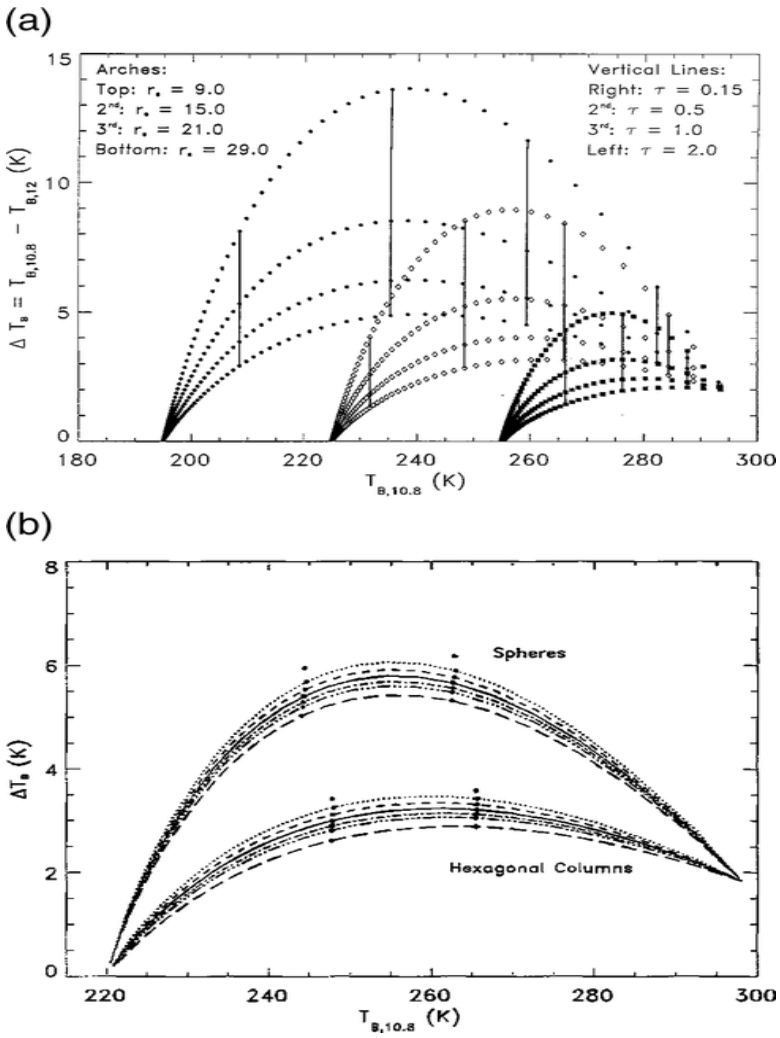

Figure 8 - a) Theoretical relationship between the split window difference (ΔT_b) and the window channel ($\Delta T_{10.8\ um}$) for 3 emitting cloud temperatures. b) As above, but for a single cloud emission temperature with two different ice crystal habits (Stephens and K ummerow 2007)

A relationship between optical depth ΔT_b and $\Delta T_{10.8\ um}$ is clearly shown for a given cloud emission temperature. It can be observed that warmer a window channel per a given cloud emission temperature is related to a smaller cloud optical depths as more surface radiation from the underlying surface is partially transmitted through the cloud layer contributing to the top of the atmosphere radiances. As the optical depth increases beyond unity, the cloud emissivity also increases and ΔT_b approaches zero as the window channel temperature approaches the cloud

emission temperature at that wavelength. The surface radiance contribution to the top of the atmosphere radiances decreases with increasing optical depth. Particle size also modifies the idealized arches with smaller effective radii increasing the ΔT_b. Ice crystal morphology further modifies the relationship as seen in Figure 8b.

The use of infrared channels provides several advantages. One such advantage is that this technique does not utilize solar reflection (0.64 or 0.86 channel or equivalent) allowing for sampling to be extended into nighttime observations. Another advantage is that the strong absorption in the IR region results in the retrieval being less sensitive to assumptions relating to the phase function (Yang *et al.*, 2005). It has been shown that the split window channel method is advantageous for investigating optically thin cirrus under known surface emissivity conditions (Heidinger and Pavolonis, 2009). A well-known surface emissivity and temperature result in a well-constrained surface emission (I_{clr}) term and if the surface is warm, it can provide good thermal contrast to the cold ice cloud allowing for an accurate cloud emissivity calculation. Furthermore cloud vertical location is an important parameter for the split window method as no knowledge of the cloud top height can result in errors between 60-80% (Miller *et al.*, 2000). Disadvantages include a decrease in accuracy in geometrically or optically thick ice clouds due to a difference in emission from the cloud base and cloud top. It also becomes more difficult to retrieve an optical thickness value under cold surface conditions.

2.4.2 NOAA Enterprise Infrared (IR)

The NOAA Enterprise IR retrieved optical depth product is an optimal estimation-based retrieval that uses satellite-measured infrared radiances to combine information on cloud top height from the CO_2 slicing method with the sensitivity of the split window approach to cloud microphysics and optical properties (Heidinger, 2015). The CO_2 slicing method utilizes the

spectral opacity of the atmosphere between the 13 – 15-micron region, allowing for the emitted radiances to have sensitivity at different layers (Menzel *et al.*, 2008; Chahine, 1974). This method allows for the determination of a temperature profile and cloud top pressure and helps constrain the cloud emissivity. The split window approach in this retrieval utilizes the emissivity at the 11- and 12-micron channels to construct the beta parameter (β) which is a proxy for particle size, with smaller beta values implying smaller particles (Inoue, 1985). The differential absorption of the two wavelengths also aids in the calculation of optical thickness. All equations in this section are credited to Heidinger and Pavolonis 2009 or (Heidinger, 2015) unless otherwise stated. As in the visible retrieval, a forward model shown in equation 4 simulates a variety of atmospheric conditions which is used to construct a state vector to be utilized in the optimal estimation.

$$(4)\quad I_{calc} = \epsilon_c I_{ac} + T_{ac}\epsilon_c B(T_c) + I_{clr}(1 - \epsilon_c)$$

Where I_{calc} is the simulated top of the atmosphere spectral radiances to compare to the observed radiances at the sensor, I_{clr} is the emitted clear sky radiances (surface contribution), ϵ_c is the emissivity of the cloud, $B(T_c)$ is the emitted radiances by the cloud from the Planck function and I_{ac} is the above cloud radiance contribution. The optimal estimation uses the brightness temperatures at the 11, 12 and 13 microns with the forward model to converge on a solution for the cloud top temperature, 11-micron emissivity, and the beta parameter. The cloud emissivity and the scattering characteristics determined from the beta parameter are then used to calculate the optical thickness as shown in equation 5.

$$(5)\quad \tau_{vis} = \frac{\sigma_{vis}}{\sigma_{11\mu m}}\left[\frac{-\mu ln\,(1-\epsilon_C)}{1-\omega_{11\mu m}g_{11\mu m}}\right]$$

Where μ is the cosine of the view angle, σ_{vis} is the extinction coefficient at the visible wavelength, $\sigma_{11\mu m}$ is the extinction coefficient at 11 µm, $\omega_{11\mu m}$is the single scattering albedo at 11µm and $g_{11\mu m}$ is the asymmetry parameter at 11µm. In s ummary, the 11-micron cloud emissivity is used to calculate optical thickness in the IR, while the extinction ratio and scattering parameters modify the calculated IR optical thickness to what would be observed at the visible wavelengths. An example of the output satellite product is shown in Figure 9.

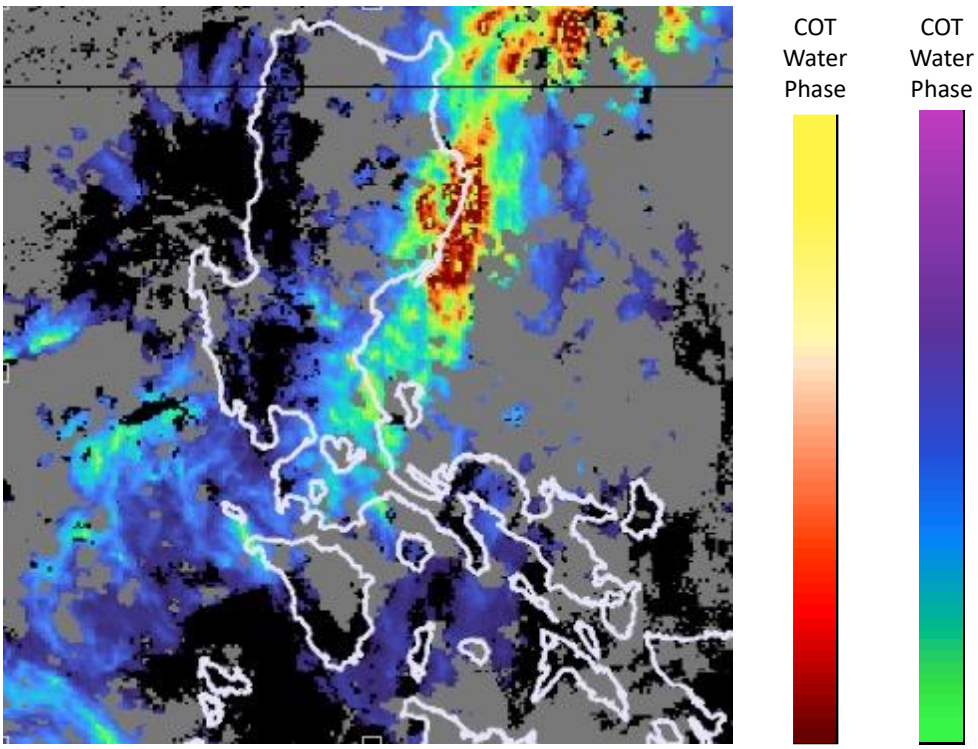

Figure 9 - NOAA Enterprise IR optical depth product from GEO Worldview for November 29th, 2019 at 23:50 UTC for the Northern Philippines.

2.5. The High Spectral Resolution Lidar

2.5.1 Traditional Lidar Principles

Lidars are powerful tools for atmospheric science research and validation due to their ability to directly profile the atmosphere. A lidar works by transmitting a pulse at a given central wavelength through an atmospheric col umn. If positioned vertically upwards, the beam at any given level may be transmitted, absorbed, or scattered as it ascends to higher altitudes. When the beam interacts with a cloud or aerosol particle a portion of the radiation will be scattered according to the phase function which will depend on the microphysical properties of the substance (size, phase, shape, refractive indices, etc). The energy received at the receiver on the ground will correspond to the 180-degree phase function. Because the time from the initial pulse and the speed of light is known, you can infer the amount of power incident on the receiver at each vertical bin level which translates to altitude. The traditional lidar equation is show in equation 6 and obtained from http://lidar.ssec.wisc.edu/.

$$(6)\quad P(r) = E_o \frac{cA_r}{2r^2}\left(\beta_a(r)\frac{P(\pi,r)}{4\pi} + \beta_m(r)\frac{3}{8\pi}\right)e^{-2\tau(r)}$$

where

P = Received power

E_o= Laser Pulse energy

c = Speed of light

A_r= Collection area of receiver

R = Range to scattering vol ume

β_a = Aerosol back scattering cross section

β_m = Molecular back scattering cross section

$\frac{P(\pi,r)}{4\pi}$ = Backscatter phase function

$\frac{3}{8\pi}$: Molecular backscatter phase function

$\tau(r)$ = Optical Thickness

The optical thickness is simply the range dependent integral of extinction as shown in equation 7.

$$(7)\quad \tau = \int_0^r \beta_e(r)dr$$

For traditional lidars, the unknown quantities in equation 6 are the aerosol backscatter cross section, the backscatter phase function, and the extinction. It should be noted however that the backscatter cross-section and extinction are related by the backscatter phase function. This means there is an insufficient amount of information to independently retrieve the optical thickness/extinction and the particulate backscatter cross section without making assumptions. The Klett method has been used to solve the lidar equation by ass uming a power law relationship between the backscatter and attenuation (Klett, 1981), however, this method does induce uncertainty as it assumes an a priori lidar ratio which can be highly variable (Holz et al. 2002).

2.5.2 HSRL Lidar Principles

The University of Wisconsin High Spectral Resolution Lidar is a ground, ship or aircraft based lidar that operates in the visible and near IR part of the spectr um at 532nm and 1064nm. The current Atmospheric Observing System ((AOS) formerly ACCP (Aerosols Clouds Convection Precipitation)) is considering a satellite based HSRL to improve estimations of aerosols and optically thin ice clouds. The HSRL is designed to overcome the limitations of a traditional backscatter lidar and does so by not only having a combined and cross-polarization

channel, but also molecular channel. Unlike traditional lidar instruments, the molecular channel has an iodine molecular filter that allows the instrument to separate particulate and molecular signals (Eloranta, 2005). The separation of the molecular signal is possible because thermal molecules travel at thermal velocities while aerosols, which generally travel with atmospheric flow are far slower. Because the wavelength of the lidar pulse is known, when the laser interacts with a molecule and is backscattered, there is an offset in wavelength/frequency due to doppler broadening, whereas aerosols have negligible Doppler broadening. Figure 10 shows the frequency offset from the known lidar pulse frequency (Goldsmith, 2016).

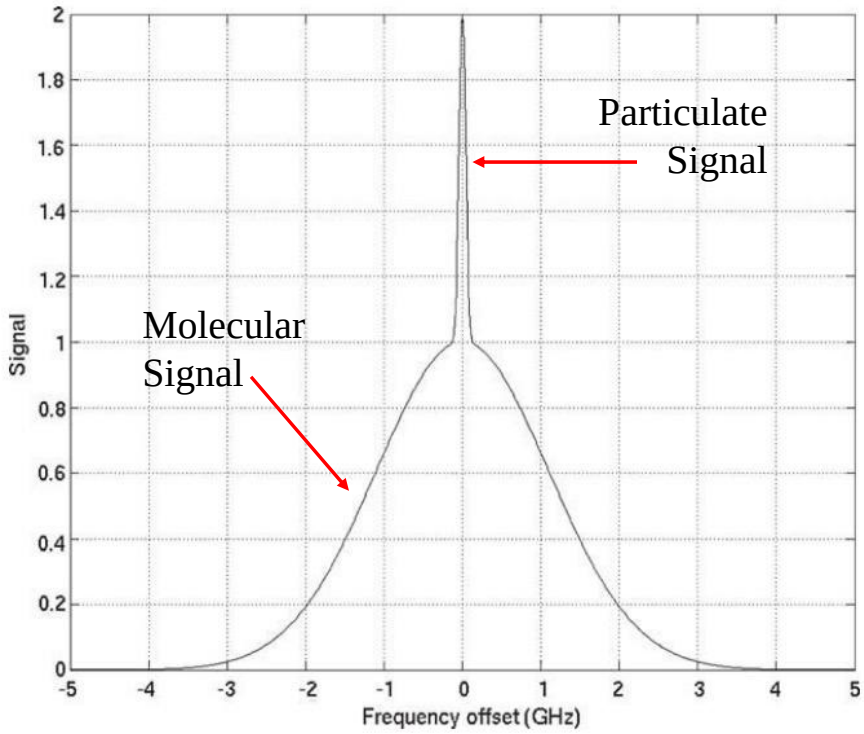

Figure 10 - Frequency offset of HSRL return signal due to aerosols and molecules (Goldsmith 2016)

The gaussian like distribution shows the doppler broadening due to thermal molecules, while the sharp peak in the center is the non Doppler broadened aerosol signal. The HSRL laser is then

tuned to the iodine absorption line and the molecular signal is cropped from the aerosol signal. With a molecular and combined channel, the lidar equation can be broken down from the traditional lidar equation (equation 6) to the aerosol/particulate and molecular components (equation 8 and 9).The physical separation of these signals by the iodine filter is significant because this eliminates assumptions that must be made for traditional lidars that allow for the separation of the aerosol and molecular return components in the traditional lidar equation. The following equations in this section are from http://lidar.ssec.wisc.edu/.

$$(8)\quad P_m(r) = E_o \frac{cA_r}{2r^2} \beta_m(r) \frac{3}{8\pi} e^{-2\tau(r)}$$

$$(9)\quad P_a(r) = E_o \frac{cA_r}{2r^2} \beta_a(r) \frac{P(\pi,r)}{4\pi} e^{-2\tau(r)}$$

The two unknowns in the equation 8 are τ and β_m, while in equation 9 the unknowns are $\beta_a(r)\frac{P(\pi,r)}{4\pi}$ and τ .Due to the exponential decay of atmospheric molecules with height the molecular back scattering cross section can be explained by Rayleigh scattering theory and atmospheric density as shown in equation 10. This is typically done using radiosonde data.

$$(10)\qquad \beta_m = C\rho(r)$$

$$(11)\qquad S_m(r) = \frac{P_m(r)\, r^2}{E_o}$$

Optical depth τ can then be determined by combining equations 8, 10 and 11 and the optical depth of a layer can be found by taking the difference between two optical depth ranges:

$$\tau(r) - \tau(r_o) = \frac{1}{2} ln(\frac{\rho(r)}{\rho(r_o)}) - \frac{1}{2} ln(\frac{S_m(r)}{S_m(r_o)}) \quad (12)$$

This displays the potential of HSRL to utilize the molecular signal to determine the optical depth of the cloud with minimal prior assumptions. The optical depth is also the time range integral of extinction.

$$\tau = \int_0^r \beta_e(r) dr \quad (13)$$

The aerosol backscatter cross-section can be determined by combining equations 8 and 9 to determine the backscatter ratio

$$R(r) = \frac{P_a(r)}{P_m(r)} \quad (14)$$

And isolating the aerosol backscatter cross-section

$$\beta_a(r) \frac{P(\pi,r)}{4\pi} = R(r)\beta_m(r) \frac{3}{8\pi} \quad (15)$$

The ability for the HSRL to filter its signal into a molecular component allows for the calculation of optical thickness/extinction without prior assumptions. It also allows for the determination of the aerosol backscatter cross-section when utilizing information from the two lidar equations. In the next section, we will introduce the two field campaigns that carried the HSRL and explain

the advantages the ground/ship-based HSRL has for IOT retrieval evaluation relative to other validation methods used in previous studies.

2.6 HSRL as a Validation Tool

2.6.1 Relevant CAMP2EX and PISTON Field Campaign Information

Data collected by the UW-HSRL during the CAMP2EX and PISTON field campaigns are used to evaluate the NASA CLDPROP and NOAA Enterprise IOT retrievals processed on AHI. The CAMP2EX field campaign (Reid *et al.*, 2023) officially took place in late summer of 2019 with a plethora of instrument platforms mounted on a Learjet 35 aircraft, which flew around the maritime continent of the Philippines. More crucially for the validation effort in this thesis, the UW-HSRL was positioned at the Manila observatory (14.6361° N, 121.0775° E) in support of the program, and was deployed from December 2018-2020. The concept of CAMP2EX was to utilize multiple passive and active ground, airborne and space-based sensors to better characterize aerosol-cloud interactions, cloud microphysics and quantify the radiative environment over and around the Philippines during the southwest monsoon. The scientific sub-objectives beyond these overall primary goals stated above are beyond the scope of this thesis as the objective of this work is to simply utilize the HSRL data collected during this campaign to evaluate the NASA CLDPROP and NOAA Enterprise IOT retrievals. However, it should be stated that the region has heavy cirrus cloud cover and thus the quantification of ice cloud radiative effects and optical thickness would be a major observable to accurately quantify the radiative environment in and around the Philippines. The UW Lidar program supports several HSRL instruments designed to collect autonomous measurements. The UW-HSRL positioned at the Manila observatory is the Artic HSRL (AHSRL) system which will provide IOT information in this urban environment.

Also utilized in this thesis is data from the PISTON 2018 field campaign (Sobel *et al.*, 2021). The PISTON 2018 field campaign took place from August - October 2018 and consisted of two cruises by the R/V Thomas G. Thompson in the Philippine sea. The original purpose of the campaign was to target the Boreal Summer Intraseasonal Oscillation, however, the HSRL carried during this field campaign provides a unique opportunity to evaluate satellite retrieved IOT in an oceanic environment. The UW-HSRL deployed in this field campaign is the BagoHSRL and was originally designed to be a trailer-mounted system to be used in combination with other instruments. Figure 11 from Sobel et al. 2021 shows the ship paths that carried the BagoHSRL during the PISTON field campaign and thus the spatial region in which the NASA CLDPROP and NOAA Enterprise IOT retrievals will be evaluated over the ocean.

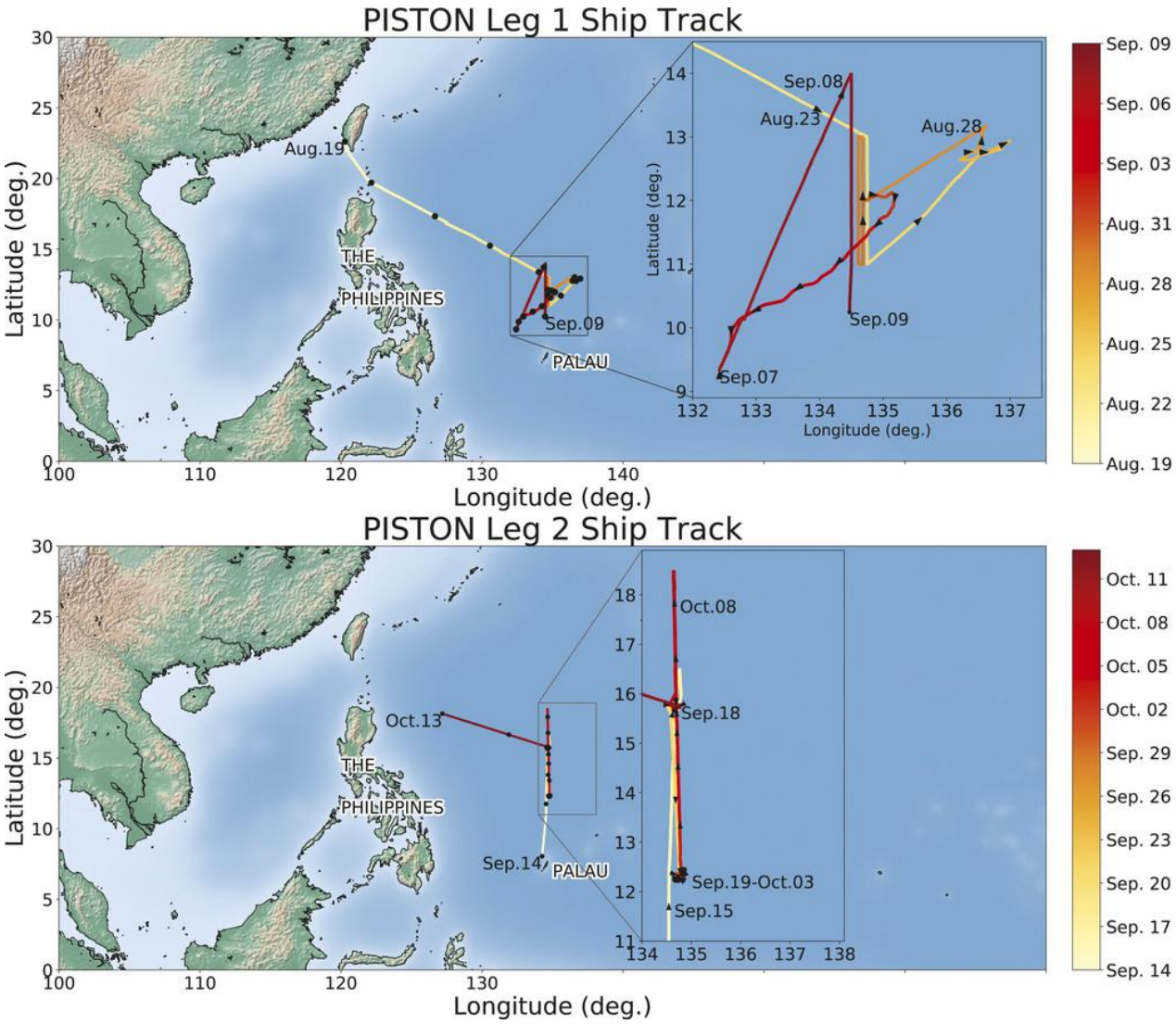

Figure 11 – PISTON 2018 ship tracks in the Phillipine sea from Sobel et al. 2021. These tracks show the regions in which the HSRL collected over ocean data and where the AHI IOT retrievals will be validated. The red line shows the AHI longitudinal position in GEO

2.6.2 Advantage of the HSRL deployed during CAMP2EX and PISTON for Validating Satellite Retrieved IOT

The HSRL deployed during the CAMP2EX and PISTON campaigns provides a unique opportunity to evaluate satellite-based IOT retrievals using both urban and oceanic environments. Section 2.5.2 showed that the HSRL has a distinct advantage for retrieving IOT

compared to traditional backscatter lidars due to the system's ability to directly measure extinction and particulate backscatter without making erroneous assumptions. To re-iterate, the HSRL advantage comes from physically separating the molecular signal with an iodine absorption filter, allowing for the lidar equation to be separated and solved. Furthermore, accurate estimates of uncertainty can be determined as will be seen in the methods section in 3.1.4. Because the HSRL is the most accurate lidar system for retrieving IOT, it is one of the best retrieval evaluation tools currently available. Past literature suggest that the NOAA Enterprise IR retrieval will have high sensitivity to ice clouds within the dynamic range of the HSRL (thin ice clouds)(Heidinger and Pavolonis, 2009), while the retrieval of thin ice clouds has historically been a challenge (Holz *et al.*, 2016). As was seen in the visible and infrared IOT retrieval theory sections (2.3 and 2.4), an IOT measurement from space-borne sensors requires an accurate surface BRDF in the visible and surface emissivity and temperature in the infrared. When refrencing the "surface assumption" we are refering to the surface BRDF in the visible and the surface emissivity and temperature in the infared. In addition, the ice crystal scattering assumption must be valid to correctly model the directional intensity of radiation as it interacts with the cloud layer. Due to these retrieval constraints, and the HSRL's ability to directly measure extinction/optical thickness, an HSRL over a well-quantified surface BRDF environment such as the ocean is the most optimal method to evaluate IOT. This is optimal for two reasons: 1) The ocean's BRDF and emissivity is well quantified over the ocean negating the impact of the surface contributions to the satellite-observed reflectances and/or radiances. 2) Due to the absence of the surface contribution, the validity of the assumptions about the cloud such as the ice scattering assumption can be independently examined from the surface. These optimal retrieval evaluation conditions are provided by the HSRL deployed during the 2018 PISTON

campaign. 3) The over-ocean satellite retrieval evaluation results can then be compared with the same experiment over land to examine the impact of surface as well as the validity of the surface assumptions within the satellite-derived IOT retrievals. In this study, we use the HSRL deployed at the Manila observatory in support of the CAMP2EX campaign. Because both field campaigns are positioned within the AHI's field of view, and the AHI can run accurate high-quality stable cloud retrievals (section 2.2) such as the NASA CLDPROP (section 2.3.1) and NOAA Enterprise algorithms (section 2.3.2 – 2.3.2), the combination of these two datasets provides a unique opportunity to leverage AHI's superior co-location frequency with these HSRL observations to evaluate these IOT products.

Unfortunately, before this work ocean-based co-located satellite-HSRL measurements have been historically limited due to operational logistics and the cost of a ship-based HSRL for an extended period. That constraint hindered the crucial oceanic dataset required to implement this study's validation strategy. Furthermore, the advancements in geostationary technology as stated in section 2.2allows for the first time MODIS-like cloud retrievals from geostationary orbit. Previously, co-locating ship-based HSRL measurements with LEO spectroradiometers for IOT retrieval evaluation was not possible due to limited single-layer ice cloud co-location opportunities during the time duration of the field campaign. Past efforts to evaluate passive ice cloud optical thickness retrievals have largely centered on utilizing CALIPSO, such as the retrieval evaluation work performed on MODIS (Holz *et al.*, 2016; Heidinger *et al.*, 2015; Wang *et al.*, 2016). The wealth of validation work involving MODIS and CALIPSO is because CALIPSO once flew in the A-Train with MODIS on Aqua, providing numerous co-located measurement opportunities.

Past efforts to evaluate passive ice cloud optical thickness retrievals have largely centered on utilizing CALIPSO, such as the retrieval evaluation work performed on MODIS (Holz *et al.*, 2016; Heidinger *et al.*, 2015; Wang *et al.*, 2016). However, CALIPSO has several disadvantages that the ground-based HSRL does not share. CALIPSO works best for infrared retrieval evaluation as the performance of its extinction measurement and thus IOT product is diminished during the daytime. CALIOP's daytime signal-to-noise ratios (SNRs) are significantly lower due to required changes in the calibration coefficients of the 532 nm channel from solar radiation, complicating daytime validation of visible cloud optical property retrievals. Another disadvantage is that CALIOP also must assume a lidar ratio for their IOT retrieval and multiple scattering regardless of day or night status, while the HSRL does not share these disadvantages as was shown in sections 2.5.1 and 2.5.2. Lastly, in-situ-based measurements such as that from a ground-based lidar also have the advantage of typically having higher SNR values than space-borne lidars due to great distances between the atmospheric target and the spacecraft, onboard power limitations, as well as a combination of relatively low pulse rates and high speeds across the target (Hlavka *et al.*, 2012).

In this thesis, we utilize an in-situ-based (ground and ship) HSRL to evaluate the NASA CLDPROP and NOAA Enterprise daytime retrievals processed on the AHI instrument. The GEO-in-situ-based combination allows for superior continuous colocation and sampling relative to an LEO-in-situ combination because the in-situ measurements are always within the field of view of the GEO. Analogous past literature for GEO-HSRL retrieval evaluation is that of Kox et al. 2014, who utilized data collected from an HSRL on the airborne FALCON campaign over continental Europe to validate an infrared machine learning cloud optical thickness retrieval run on SEVERI and trained on CALIOP data. However, unique to this study is the evaluation of the

operational NASA CLDPROP and NOAA Enterprise daytime products by the HSRL over an extremely well-behaved surface Bidirectional reflectance distribution function (BRDF) environment: the ocean. This unique aspect enables the evaluation of retrieval assumptions such as the scattering phase function as well as the impact of different surface environments on the retrieval when compared to the over-ocean measurements. The results of this evaluation will provide a snapshot of the validity of the assumptions and techniques used in the two retrieval algorithms.

3. Methods

3.1 HSRL Ice Cloud Optical Thickness Retrieval

As seen in section 2.6, the HSRL provides several distinct advantages relative to past validation efforts. The material contained in the methods section is no longer background material and was used to produce the HSRL Ice Cloud Optical Thickness retrieved product that was used to validate the NASA CLDPROP and NOAA Enterprise IOT retrievals. Section 3.1.1 will show how the HSRL is calibrated while section 3.1.2 show the forward model equations used in the algorithm. These two sections are directly implemented into the HSRL IOT retrieval but are borrowed from past work and are referenced. Section 3.1.3 shows the algorithm developed by the author of this thesis and is unique to this work. Section 3.1.4 shows the method in which is used to quantify uncertainty, and was developed by working with the HSRL lidar group.

3.1.1 Calibration of HSRL Data

Before geophysical variables can be calculated from the return signal, the raw photon counts received by the avalanche photodiodes (APDs) must be corrected for after pulsing (i.e., the internal scattering of photons within the instrument). Figure 11 shows a visual timeline of the

APD pulse timing for the HSRL, which contain important photon counting correction information.

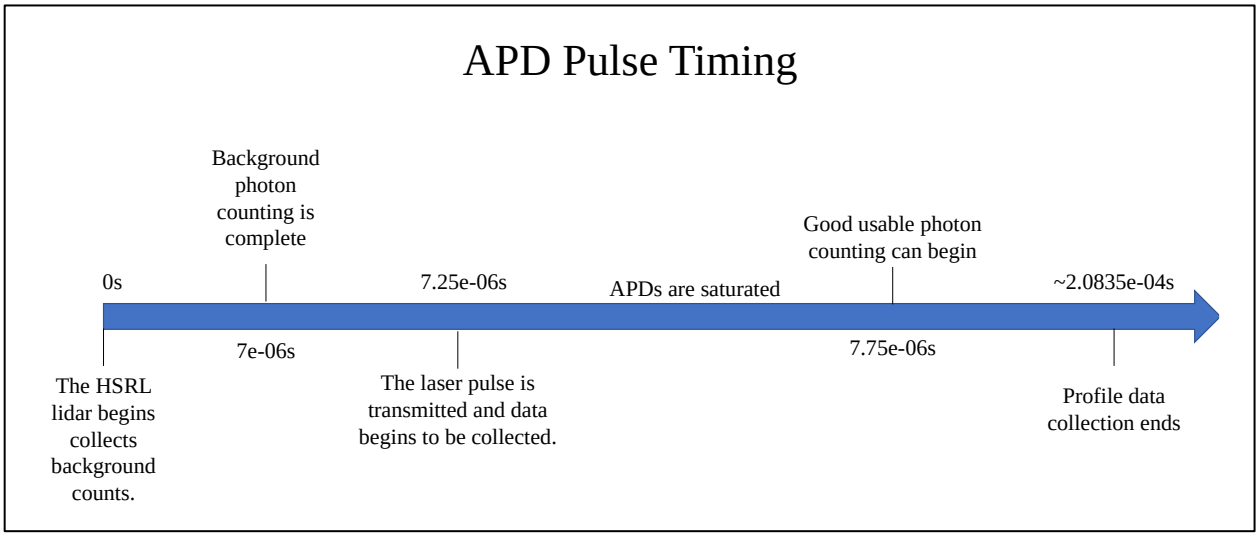

Figure 11- Data collection and calibration timeline for the avalanche photodiodes

The first correction is for the background photon counts ($N_{background}$). The background photon counts are determined by exposing the detectors to background solar radiation and detector dark current for approximately 7e-06 seconds. After the background photon counts are quantified, the laser pulse is transmitted from the HSRL, and data collection begins. There are initially photons scattered from the laser pulse that saturate the APDs ($N_{baseline}$) (Razenkov, 2010), however good usable photon counts begin 0.25e-06 seconds later. The photon counts collected during this time are binned into ranges corresponding to the collection rate of the detector that defines the native resolution of the HSRL (7.5m). The background counts and baseline correction are then subtracted from the photon counts in each bin range as shown in equation 16.

$$N_{corrected} = N_{total} - N_{baseline} - N_{background} \quad (16)$$

Now that the photon counts have been corrected at the detector level, we must consider the attenuation and leakage of photons as they travel through the optical system. For the molecular channel there are two calibration coefficients corresponding to the transmission and leakage of photons through the iodine absorption filter onto the detector. The correction from Razenkov 2010 is used for the molecular and combined signals to obtain the molecular N_{mol} and particulate N_a calibrated photon counts. The molecular signal is:

$$S_{mol} = C_{am}N_a + C_{mm}N_{mol} \quad (17)$$

C_{mm} corrects for the attenuation of the molecular photons through the iodine filter, while C_{am} corrects for the leakage of aerosol photons that are not removed by the iodine filter. The signal in the combined channel is:

$$S_{cmb} = C_{ac}N_a + C_{mc}N_{mol} \quad (18)$$

Where C_{ac} is the relative contribution of the aerosol onto the combined channel and C_{mc} is the relative contribution of molecules onto the combined channel. These coefficients are precomputed (Eloranta, 2005). The calibrated corrected photon counts are then found by inverting equations 17 and 18.

$$N_{mol} = \frac{S_{mol} - S_{cmb}C_{am}}{C_{mm} - C_{am}C_{mc}} \quad (19)$$

$$N_a = \frac{S_{cmb}C_{mm} - S_{mol}C_{mc}}{C_{mm} - C_{am}C_{mc}} \quad (20)$$

3.1.2 HSRL Atmospheric Measurements and Inverted Forward Models Equations

Geophysical variables of interest must be calculated from the raw photon counts before ice clouds can be identified and their optical properties calculated for validation purposes. Due to the Poisson bootstrapping methodology outlined in the uncertainty quantification section in 3.1.4, the level 2 products produced on the HSRL website cannot be used and the geophysical parameters must be demined from the photon counts using the HSRL forward model equations. The HSRL has 3 forward model equations, one for each channel that are inverted to obtain the optical thickness, backscatter cross-section and depolarization ratio (Marais, 2021; Holz, 2002). These equations slightly differ from the more simplified HSRL lidar principles section as they include calibration, polarization considerations, and other important information related to HSRL processing (Marais 2021). Below are the equations used to calculate the geophysical variables used in the ice cloud optical thickness retrieval:

The depolarization (δ_p) is

$$\delta_p = \frac{N_{pol}}{N_{cmb}} \quad (21)$$

Where N_{pol} is the calibrated photon counts in the cross-polarization channel.

$$N_{pol} = G\left(S_{pol} - C_0 S_{cmb}\right) - C_{mc} N_{mol} \delta_m \quad (22)$$

G is the combined to cross polarization gain ratio, C_0 is the polarization cross talk and δ_m is the molecular depolarization. The particulate backscatter cross-section (v_a) is:

$$v_a = \frac{v_{mol}^{\parallel}(N_{cmb}C_{mm} - N_{mol}C_{mc})}{N_{mol} - N_{cmb}C_{am}}(1 + \delta_p) \quad (23)$$

Where $v_{mol}^{\parallel}$ is the molecular backscatter. The optical thickness is:

$$\tau = -\frac{1}{2}\log\left(\frac{(N_{cmb}C_{am} - N_{mol})r^2}{0v_{mol}^{\parallel}(C_{am}C_{mc} - C_{mm})e^{-2t_m}}\right) \quad (24)$$

The signal to noise ratio is

$$SNR = \frac{\mu}{\sigma} \quad (25)$$

Photon counting noise follows a Poisson distribution and thus the standard deviation is:

$$\sigma(N) = \sqrt{N} \quad (26)$$

The molecular signal to noise ratio is:

$$SNR_{mol} = \frac{N_{mol}}{\sigma(N_{mol})} \quad (27)$$

The photon counting noise in each channel utilized for the calculation of the particulate backscatter cross-section must be considered, therefore the law of error propagation is used to determine the total uncertainty as shown in equation 28.

$$\sigma(v_a)^2 = \sqrt{\left(\frac{\partial v_a}{\partial N_{cmb}}\right)^2 \sigma(N_{cmb})^2 + \left(\frac{\partial v_a}{\partial N_{mol}}\right)^2 \sigma(N_{mol})^2 + \left(\frac{\partial v_a}{\partial N_{pol}}\right)^2 \sigma\left(N_{pol}\right)^2} \quad (28)$$

Where the partial derivatives of the geophysical with respect to the photon counts for each channel are solved and multiplied by the photon counting noise determined by equation 26. The particulate SNR is then:

$$SNR_{part} = \frac{v_a}{\sigma(v_a)} \quad (29)$$

3.1.3 Algorithm Description

To examine the validity of the AHI NASA CLDPROP and NOAA Enterprise retrieved products an HSRL ice cloud optical thickness retrieval (HSRL ICOTR) was created to calculate the IOT. The HSRL data was downloaded from the HSRL web interface at http://hsrl.ssec.wisc.edu/ and the raw photon counts generated from these files are used in the HSRL IOT retrieval. The inverted HSRL forward model equations shown in the previous section are utilized to output backscatter cross-section, depolarization ratio, signal to noise ratios and optical thickness from the photon counts. There are three main parts of the retrieval algorithm, the first determines all vertical levels that contain an ice or water cloud with adequate signal, the second confirms that the detected ice layers belong to an ice cloud structure and determines where the attenuation level occurs and attempts to determine cloud boundaries, while the third

calculates the optical thickness and averages the signal vertically if necessary to increase SNR. A flow chart of the algorithm is shown in figure 12.

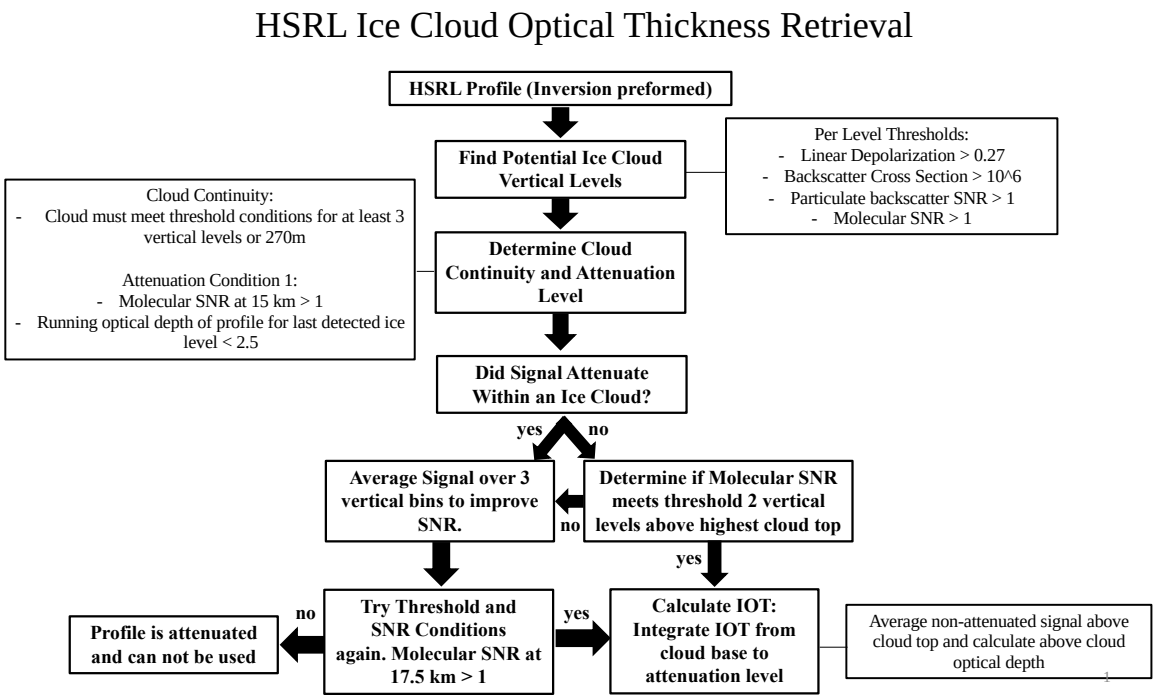

Figure 12 - HSRL Ice Cloud Optical Thickness Retrieval Flowchart

The first part of the algorithm utilizes thresholds to define a potential cloud in each layer. We seek vertical levels with adequate backscatter signal and SNR. To achieve this, a hard threshold of greater than $10^{-6}\,m^{-1}sr^{-1}$ with a molecular and particulate SNR > 1 is used to define potential cloud layers. These parameters where determined through personal communication with the UW-HSRL team earlier in the development of the algorithm. To determine if the layers are composed of ice, we use the knowledge that spherical particles such as suspended cloud droplets generally have low depolarization ratios (less than 5%), whereas ice particles have a relatively larger depolarization ratio (Turner and Eloranta, 2008). Although the minim um depolarization ratios for ice cloud detection may vary by region, for the subtropics we use a value of 0.27. This

value was determined by visual examination of ice clouds throughout the PISTON and CAMP2EX datarecords. The detected ice levels are shown in Figure 16b-d with red dots, with the thresholds for each geophysical indicated by the red dashed vertical line.

The potential ice cloud levels then advance to the second phase of the algorithm where they are examined to ensure they are part of a larger cloud structure, and the first quick check attenuation condition is performed. For each profile, if the molecular signal is attenuated (SNR < 1) before 15km, the algorithm moves onto the next profile. The 15km altitude threshold on SNR is implamented because ice clouds can be found as high as 17km in this region. If this check is passed, the detected ice cloud layers from the previous phase of the algorithm move onto the next phase where they must be continuous for at least 3 vertical levels or 450m, yielding a continuous cloud for a minim um vertical geometric thickness. This approach also establishes the cloud boundaries if the signal is not attenuated within the cloud structure. The cloud base height and cloud top height are labeled as one vertical level before and one level after the first and last vertical levels in this continuous structure to ensure the optical thickness is calculated through the whole of the cloud structure. If the signal is attenuated within the cloud, a special condition is initiated to optimize the dynamic range of the HSRL. The signal is averaged over 3 vertical bins to improve SNR and the threshold conditions are applied again with an additional constrain of the SNR > 1 at 17.5km to determine if the cloud top can be found.

Once the boundaries of the cloud have been determined, the calculation of the IOT is initiated. The lower bound of the IOT calculation is the optical depth recorded at the cloud base height (cbh). The upper bound (*atten_level*) is determined by taking all vertical levels (minim um of 3) above the cloud top height that are not attenuated (molecular SNR > 1) and calculating the signal-averaged above-cloud optical thickness. This is The above cloud running optical thickness

is determined by averaging the photon counts from the cloud top height to attenuation level, then running the averaged photon count value through the inverted forward model equation for optical depth.

$$\tau_{abv\_cld} = -\frac{1}{2}\log\left(\frac{mean(r^2(N_{cmb}C_{am}-N_{mol})[cth:atten\_level])}{mean(0v_{mol}^{\parallel}(C_{am}C_{mc}-C_{mm})e^{-2tm}\,[cth:atten\_level])}\right) \quad (30)$$

Where the calibration coefficients are defined in the calibration of HSRL data section. This is done because the optical thickness recorded by the HSRL is an increasing function with the variation at levels corresponding to higher altitudes being caused by noise as shown in figure 13.

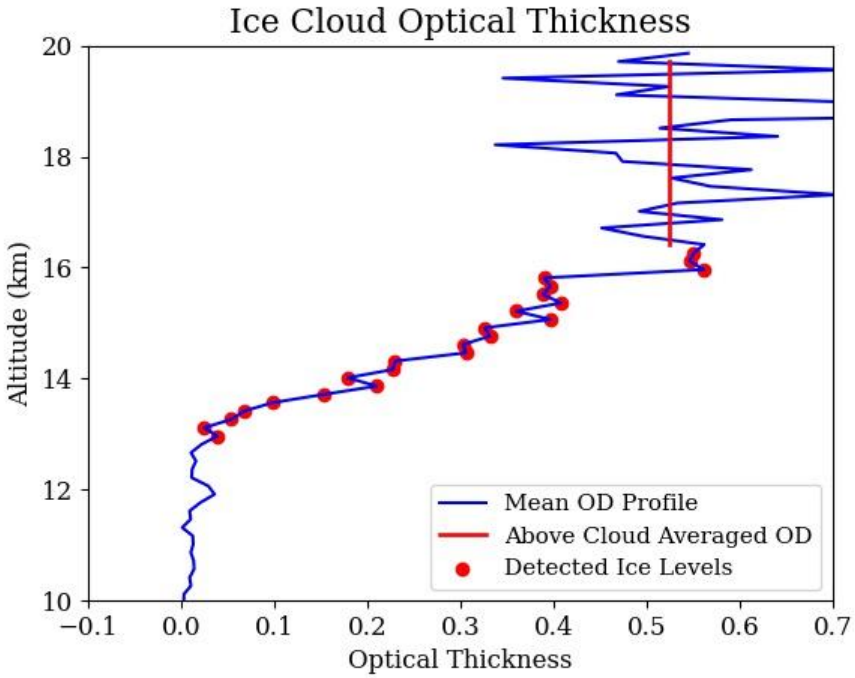

Figure 13 - Ice cloud optical thickness profile - Shows the detected ice cloud levels (red dots) as well as the above cloud averaged optical thickness value used to calculate IOT

These levels are averaged together therefore gaining higher SNR to get a more certain cloud top height optical thickness value as shown by the solid vertical red line in the figure. The ice cloud optical thickness is then calculated by taking the difference between the above cloud OD

calculated value from equation 30 (τ_{abv_cld}) and the OD value at the recorded cloud base height using equation 24.

$$IOT = \tau_{abv\_cld} - \tau_{cbh} \quad (31)$$

If there is more than one ice cloud in the profile, the boundaries of each cloud is logged and the cloud base of the lowest ice cloud is used as the lower bound to calculate the total IOT. Detected ice cloud boundaries for a case study on November 29th, 2019, are shown in figure 14C, and can be compared to the calculated backscatter cross section in figure 14A and the linear depolarization ratio in figure 14B.

The presence of a water cloud is detected in a similar way to the first phase of the algorithm. Although not the focus of this research, water cloud contamination can impact the satellite retrievals making the detection important. Therefore, the layer with the largest backscatter in the profile with a depolarization less than 0.27 is logged for later QC screening. In addition, a thick planetary boundary later can also have an impact on the retrieved optical thickness for the visible channels. To mitigate this problem, we record the integrated backscatter from the surface up to 4km and use this as an indicator in QC.

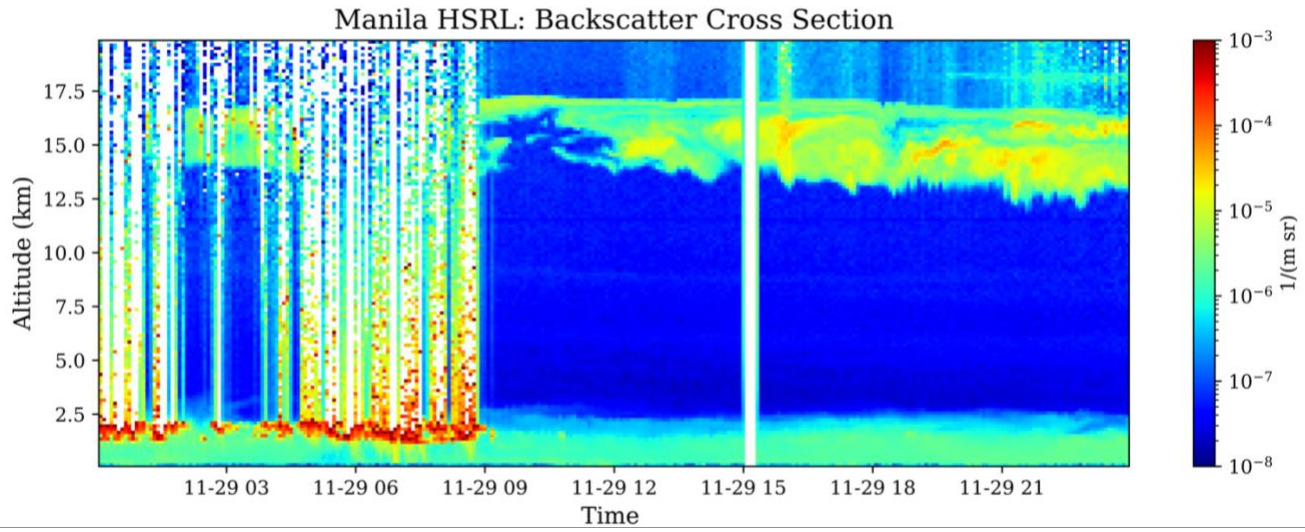
Manila HSRL: Backscatter Cross Section
Altitude (km)
17.5
15.0
12.5
10.0
7.5
5.0
2.5
11-29 03
11-29 06
11-29 09
11-29 12
11-29 15
11-29 18
11-29 21
Time
10^{-3}
10^{-4}
10^{-5}
10^{-6}
10^{-7}
10^{-8}
1/(m sr)

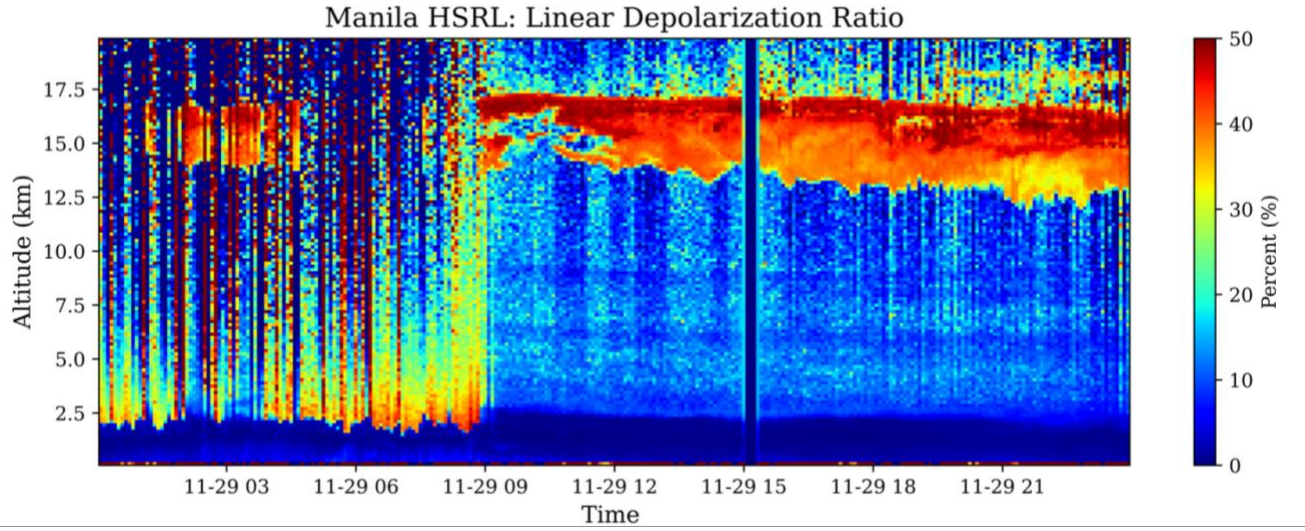
Manila HSRL: Linear Depolarization Ratio
Altitude (km)
17.5
15.0
12.5
10.0
7.5
5.0
2.5
11-29 03
11-29 06
11-29 09
11-29 12
11-29 15
11-29 18
11-29 21
Time
50
40
30
20
10
0
Percent (%)

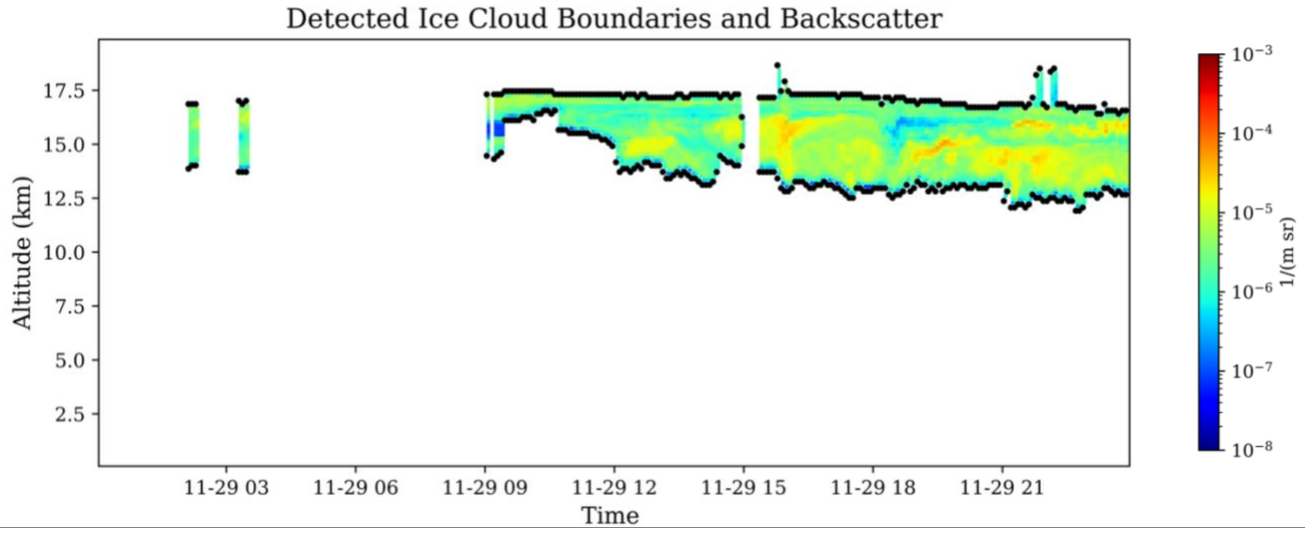
Detected Ice Cloud Boundaries and Backscatter
Altitude (km)
17.5
15.0
12.5
10.0
7.5
5.0
2.5
11-29 03
11-29 06
11-29 09
11-29 12
11-29 15
11-29 18
11-29 21
Time
10^{-3}
10^{-4}
10^{-5}
10^{-6}
10^{-7}
10^{-8}
1/(m sr)

Figure 14 -A) HSRL Inversion results for the backscatter cross-section. B) HSRL inversion results for the linear depolarization ratio. C) Detected ice cloud boundaries output from the ICOTR.

3.1.4 Uncertainty Quantification

The bootstrapping method is used to obtain uncertainty estimates in the ice cloud optical thickness measurements outlined in the previous section. The approach for calculation of uncertainty is shown in the flow chart in Figure 15.

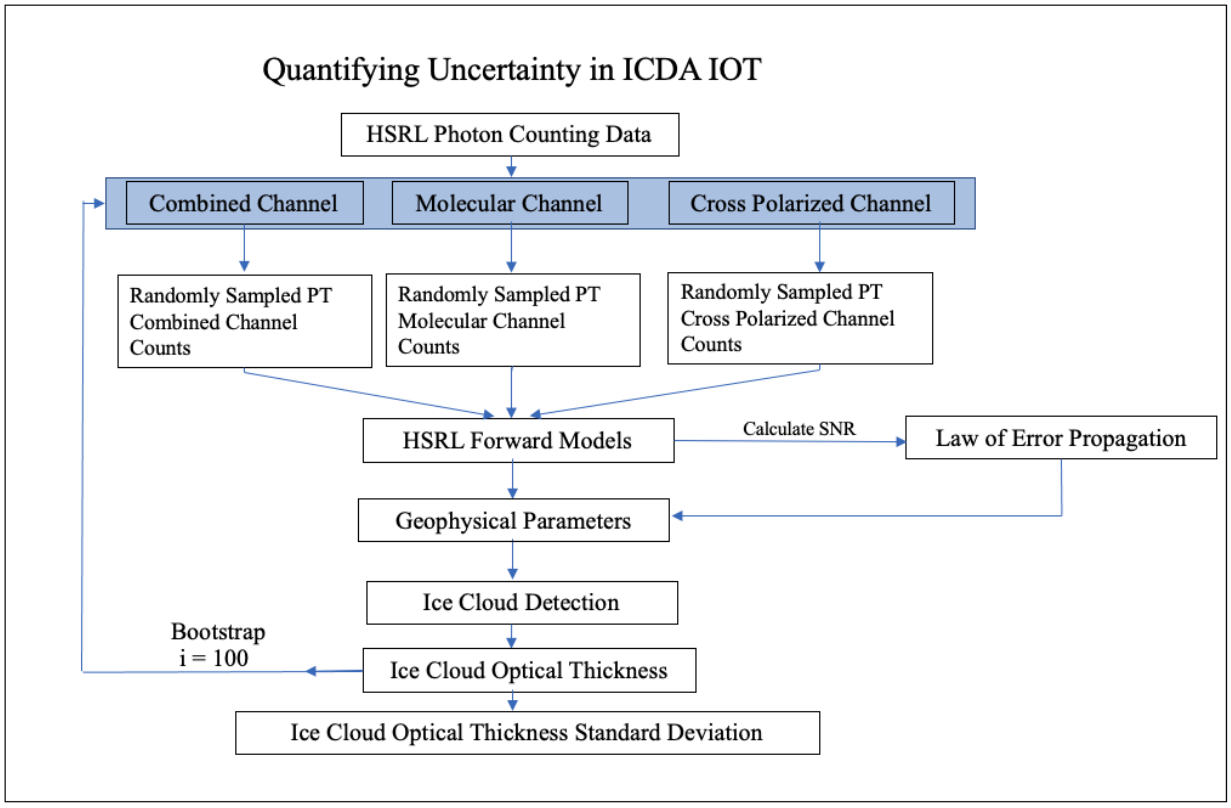

Figure 15 - The methodology for determining the ice cloud optical thickness uncertainty

The uncertainty of the photon counts measured in each of the 3 HSRL channels (combined, molecular and cross-polarization) can be ass umed to follow a Poisson distribution. We construct

a Poisson distribution about the mean photon count measurements and randomly sample with replacement using a Bernoulli distribution parameter of 0.5, this is known as Poisson thinning (PT). An example of the Poisson distribution about the mean (actual value of the photon counts shown by the red line) is shown in Figure 16 for the combined channel.

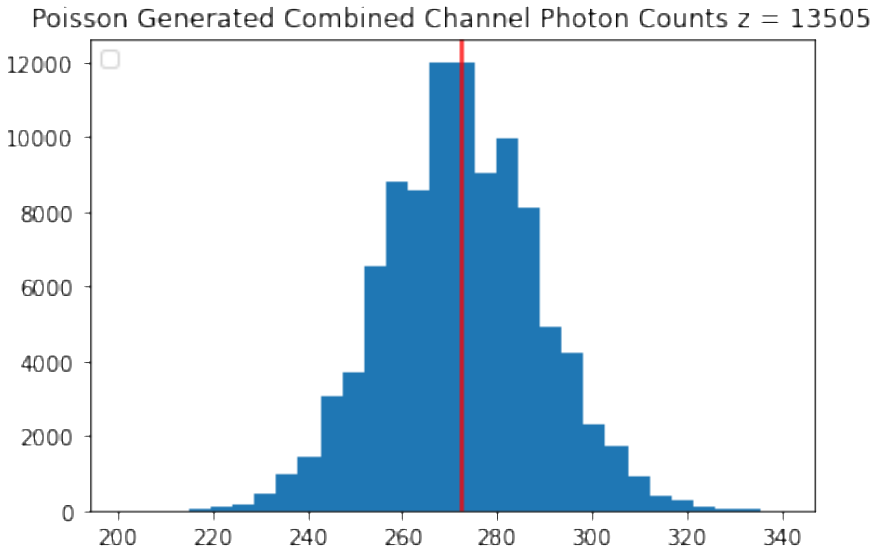

Figure 16 - Generated Poisson distribution of photon counts for the combined channel

The randomly sampled acc umulated photon counts can then be multiplied by the Poisson thinning parameter (0.5 in this case) and ran through the inverted forward model equations to obtain our geophysical parameters (optical thickness, backscatter cross section, linear depolarization ratio and unique SNR estimates for each iteration), then the ICOTR to obtain IOT this method is again shown in Figure 15. This process is repeated for 100 iterations, resulting in 100 IOT measurements from this resampling technique. Figure 17A shows the impact of the photon counting noise on the IOT measurement, with the mean of all iterations shown as the dashed vertical redline. The standard deviation is taken from all the iterations as well as the mean, for this profile (November 29th 23:30). It should be noted that the integer rounded mean

of all iterations is the actual photon count value. The statistical variation in the optical depth, backscatter and molecular SNR induced by the bootstrap method is shown in figures 17B-D, with the blue shading indicating one standard deviation at each level.

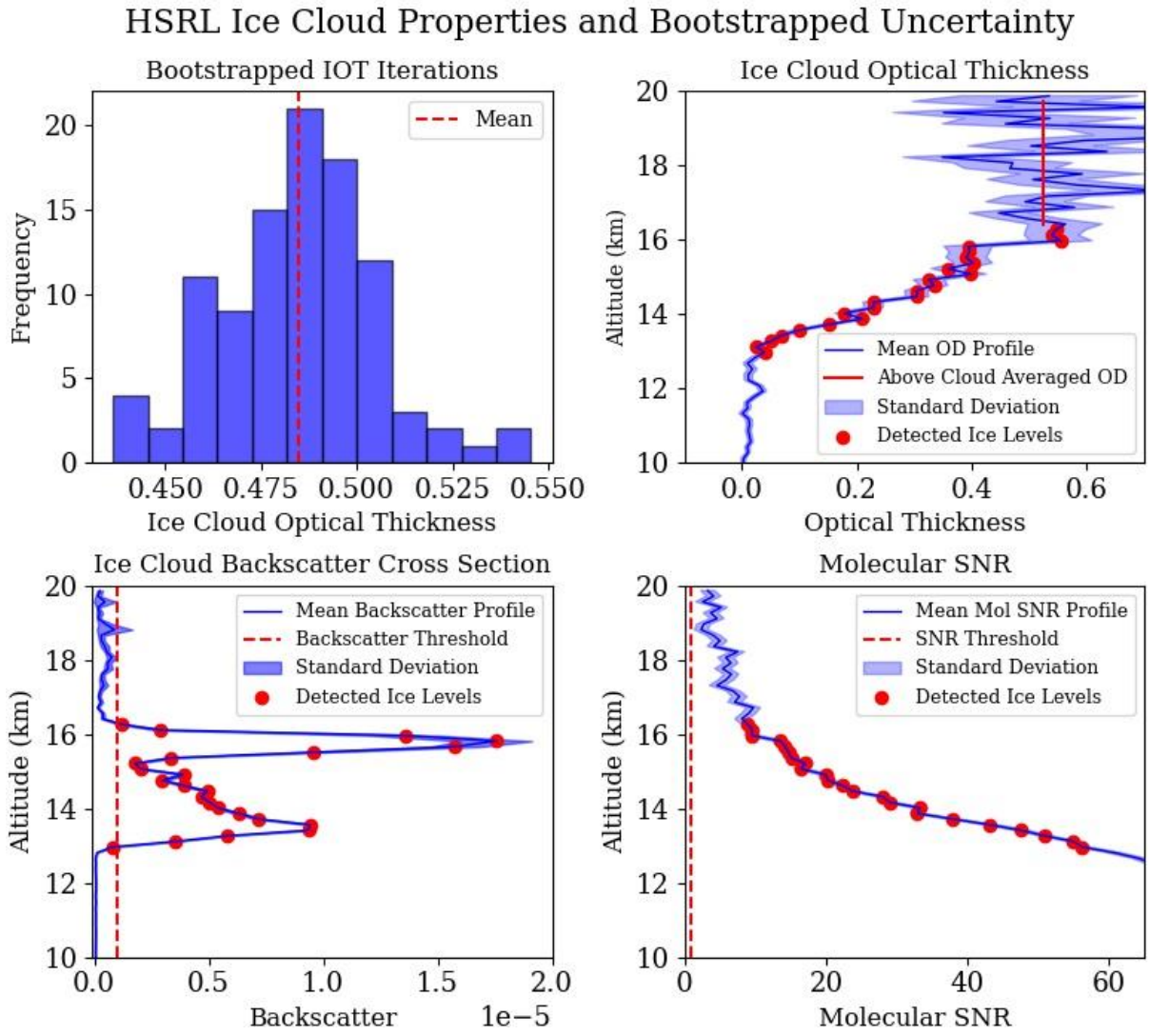

Figure 17 – Bootstrapped Results for a profile containing an ice cloud on November 29th, 23:30. A) Bootstrapped IOT histogram for 100 iterations using the ICOTR designed for this study. B) Bootstrap optical depth. C) Bootstrapped backscatter cross-section. D) Bootstrapped molecular SNR

It can be observed that at higher levels, where the SNR is lower, the variation in the optical thickness increases. Most of the variation in the IOT measurements occurs at higher altitudes despite our attempts to minimize this variation. In addition, the level of attenuation derived from the molecular SNR may change slightly in thickener cloud cases. Despite these considerations, the ICOTR is robust for ice clouds with IOT < 1.2 where its boundaries are mostly driven by the backscatter threshold condition, where the signal is far greater than the statistical variation. The statistically determined uncertainty as a function of optical thickness is shown in figure 18 for both the PISTON and Manila observatory HSRL.

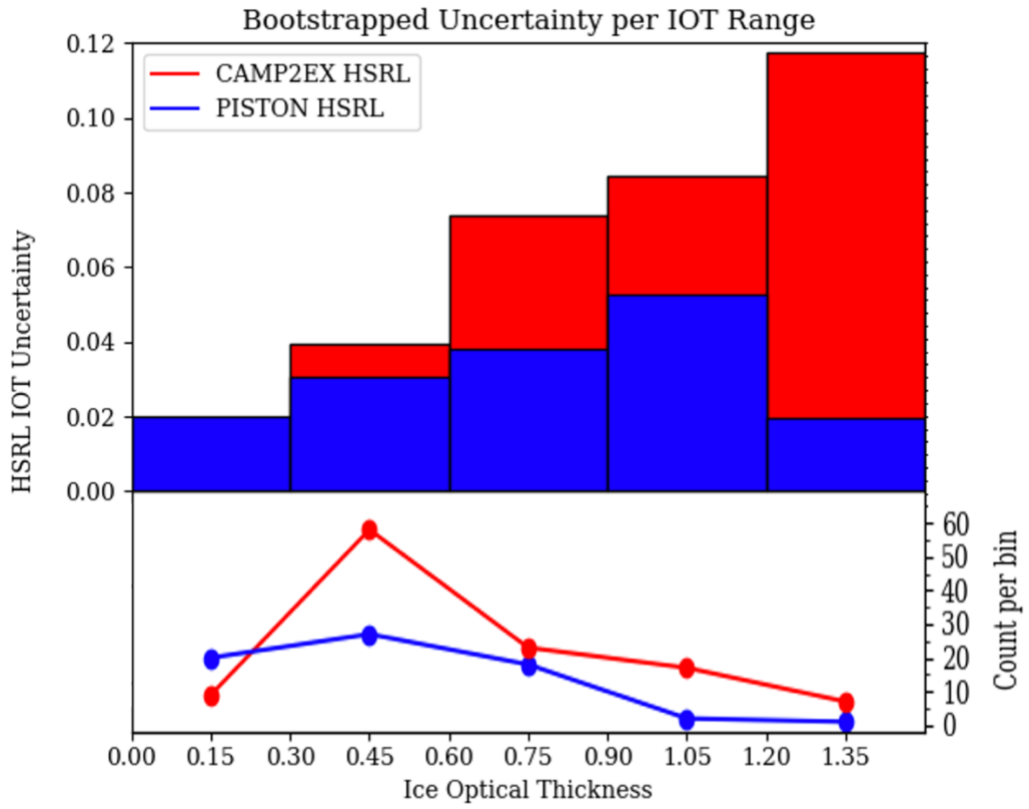

Figure 18 - HSRL IOT Uncertainty per optical depth range

It can be seen that the HSRL based in Manila (CAMP2EX) has higher uncertainty than the PISTON ship based HSRL. This is likely because of the boundary layer aerosol at the Manila

observatory having higher concentrations relative to the pristine oceanic environment during the PISTON campaign. As can be seen, the uncertainty also increases with optical thickness for both sites, with the exception of the highest optical thickness bin for the PISTON ship due to limited sampling.

3.2 Preparation of AHI Cloud Products and HSRL Retrieved IOT for Comparison

3.2.1 Co-Location of the AHI with the HSRL

The HSRL data at the land-based Manila Observatory and on board the PISTON field campaign are matched up to AHI for each HSRL 10-minute sampling interval by finding the closest pixel centroid distance to the location. The AHI cloud products have a temporal resolution of 10 minutes, and a standard product spatial resolution of 2 km. In this study, we only consider daytime observations indicated by NOAA Enterprise since we are utilizing visible retrievals. Equations 32 and 33 show how to extract the closest AHI pixel as:

$$\Delta s = \sqrt{(AHI_{lat} - HSRL_{lat})^2 + (AHI_{lon} - HSRL_{lon})^2} \tag{32}$$

$$lat_{idx}, lon_{idx} = np.argmin(\Delta s) \tag{33}$$

The minim um distance (Δs) is found and that index is extracted. It should be noted that the AHI position is parallax corrected. If the distance is less than 1.5km, that AHI pixel is used. For the ship-based HSRL, the index changes regularly as the ship moves. The movement of the ship can be seen in section 2.6.1. We always compute the minimum distance even over the stationary Manila Observatory because the parallax corrected position of the cloud sometimes results in a different pixel being chosen, furthermore, the two retrieval products were on different

geolocation grids and had to be matched up separately to the HSRL. The indices are then used to extract the optical depth at that location for comparison.

3.2.2 Quality Control of Products

Once the desired AHI pixels are extracted, the AHI data is already on the same temporal scale as the HSRL data (10 min resolution) and the actual CLDPROP and NOAA Enterprise products are quality controlled. Pixels that have a cloud fraction of less than 80% are not used in this comparison, this is because we want the cloud structure measured by the HSRL to be as representative of the entire AHI pixel as possible. There are several quality control conditions that are applied to the HSRL data. Since the HSRL is an upward looking lidar fixed at a given spatial location, we use the temporal dimension as a sudo-spatial dimension in comparison with AHI. As we seek scenes that are uniform over the AHI pixel without major radiative contaminants to the ice cloud signal, we examine the geophysical parameters over a 30-minute range (+/- 10 minutes) of the central HSRL profile. This spatial uniformity condition allows for a more accurate comparison as this is essentially an approximate cross section of the AHI pixel by the HSRL. HSRL ICOTR measurements are screened for cloud uniformity by accepting values that have a standard deviation in cloud top height of less than 1 km over the 30-minute range. In addition, measurements that are missing an adjacent temporal measurement in cloud top height and optical thickness are not used as the spatial uniformity cannot be ensured. Figure 19A shows two ice cloud scenarios that fail the spatial uniformity condition.

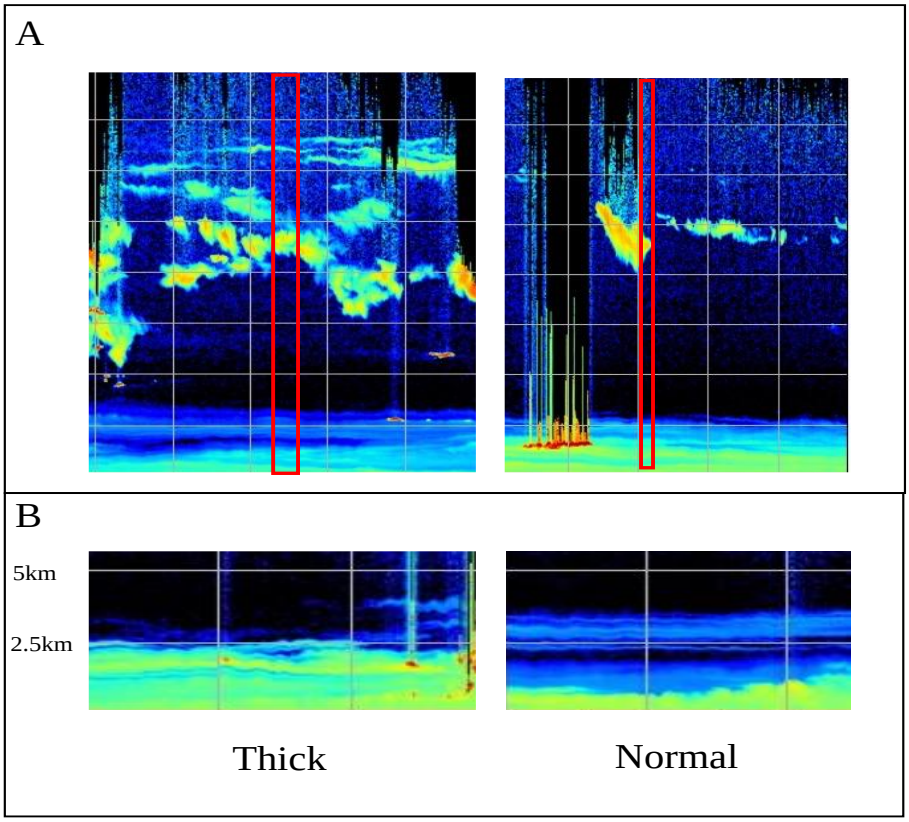

Figure 19- A) Two Ice cloud scenes shown as the backscatter cross section that fail the spatial uniformity condition. B) Example of a thick PBL that does not pass the integrated backscatter condition and a PBL that is accepted.

The lower atmosphere and PBL is screened by examining the extracted max backscatter of the water clouds and the integrated backscatter below 4 km. If a water cloud is below the ice cloud with a max vertical level backscatter of 2.5e-05 over the 30-minute range the sample is discarded. In addition, the integrated of the backscatter cross section in the lowest 4 km must be less than 8e-06, otherwise this indicates a thick lower atmosphere. Figure 19B show conditions in which the integrated backscatter condition fail (Thick) and when it is passed (Thin). Although not all of the pixel is profiled by the HSRL, we believe that the ice clouds in this comparison are relatively uniform due to these threshold conditions. Additionally, most of these ice clouds

measured in the Philippines have extensive spatial scales that are related to upper-level divergence from convective activity from the Pacific warm pool. Lastly, all HSRL IOT measurements must have less than 10% uncertainty as indicated by the bootstrap method outlined in previous section. In the next section we outline the statistical method for comparing the HSRL derived IOT with the cloud property products.

3.2.3 Statistical Method for Dataset Comparison

The retrievals will be validated by computing the square root of the correlation coefficient (R^2) value between the HSRL derived IOT and each retrieval. This approach provides a measure of linear correlation between the two datasets and is appropriate due to the two compared variables being the same geophysical parameter. The R^2 value in this case is defined in equation 34:

$$R^2 = \left(\frac{\Sigma(x-\bar{x})(y-\bar{y})}{\sqrt{\Sigma(x-\bar{x})^2\Sigma(y-\bar{y})^2}}\right)^2 \quad (34)$$

Where y is the HSRL IOT vector and $\bar{y}$ is the mean of y. x is the passive retrieved optical thickness (NASA CLDPROP or NOAA NOAA Enterprise) vector being compared to the HSRL and $\bar{x}$ is the mean of x.

4. Results

4.1 Validation of GEO Ice Cloud Property Retrievals

4.1.1 Infrared IOT Validation

4.1.1.1 Oceanic Environment

To validate the NASA CLDPROP and NOAA Enterprise infrared retrievals over ocean, the HSRL data collected during the 2018 PISTON campaign is utilized. The 2018 PISTON campaign took place in the Philippine Sea between the months of August to October during the south Asian Monsoon season. It should be re-iterated that these measurements are extremely important for retrieval evaluation as they ensure optimal surface conditions. The following comparison is the first over ocean ice cloud optical property retrieval evaluation using a well-constrained direct IOT measurement with uncertainty estimates. For the infrared channels, this is because the ocean surface temperature and emissivity are well-known and allow us to examine other retrieval assumptions. Most of the daytime data is polluted by water clouds from that campaign. The position of the ship was matched up to the AHI following the methodology outlined in the previous section. Figure 20 shows the validation of the AHI NOAA Enterprise IR retrieved IOT against the HSRL on board the PISTON 2018 campaign.

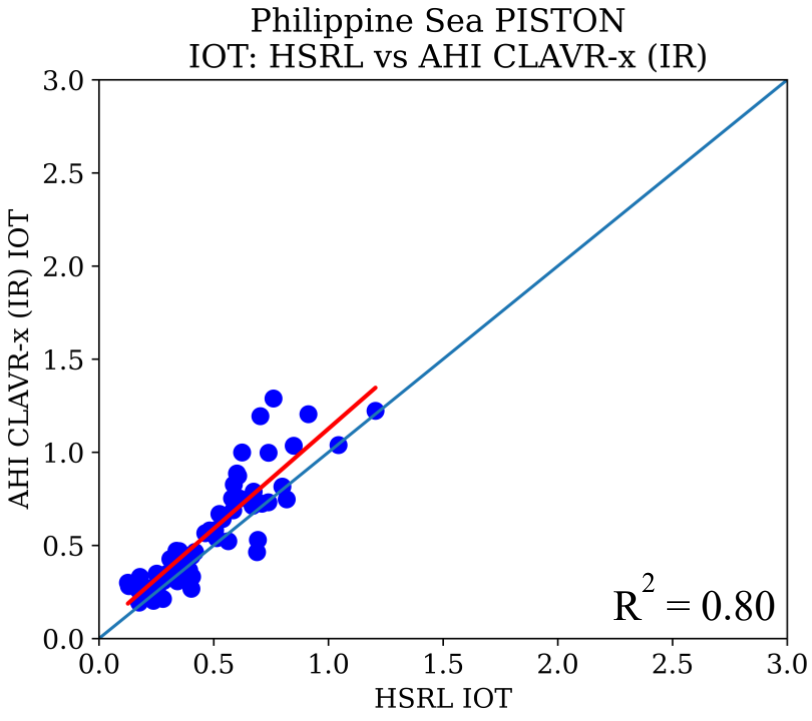

Figure 20 - Validation of the NOAA NOAA Enterprise IR optical thickness retrieval by the HSRL over ocean during the PISTON Campaign

The correlation coefficient (R^2) relative to the HSRL IOT is 0.8. It is evident that this is a robust single layer ice cloud optical thickness retrieval over ocean, especially over small optical depth values. These results agree with previous literature that suggested the split window approach is particularly sensitive to thin cirrus (Heidinger and Pavolonis, 2009; Stephens and Kummerow, 2007). Within this retrieval, surface temperature and emissivity are important parameters in order to quantify the extinction of spectral radiation through the cloud layer. It is shown that these parameters are well quantified in this oceanic environment. Although we do not have IOT values larger than 1.5 at this site, it has been suggested that the technique loses sensitivity with larger optical thickness values(Stephens and Kummerow, 2007). Although all water clouds were removed for this analysis, the IR channels also have some degree of sensitivity to ice cloud optical thickness in multi-layer ice clouds over shallow very warm water clouds as it is most sensitive to thermally cold clouds.

4.1.1.2 Urban Environment

The analysis preformed for the PISTON campaign is repeated for 1 year of observations at the Manila Observatory site during CAMP2EX. A visual of the surface properties of the city

of Manila in the Philippines is shown from google earth in Figure 21.

Figure 21 - Google maps view centered on the Manila observatory, the location of the CAMP2EX HSRL.

It can be observed that the environment is complex with dense urban housing and a mixture of terrestrial surfaces near the observatory. The developed ICOTR was run using the HSRL data at the observatory and co-located with the AHI NOAA Enterprise IR retrieval, the results are shown in Figure 22.

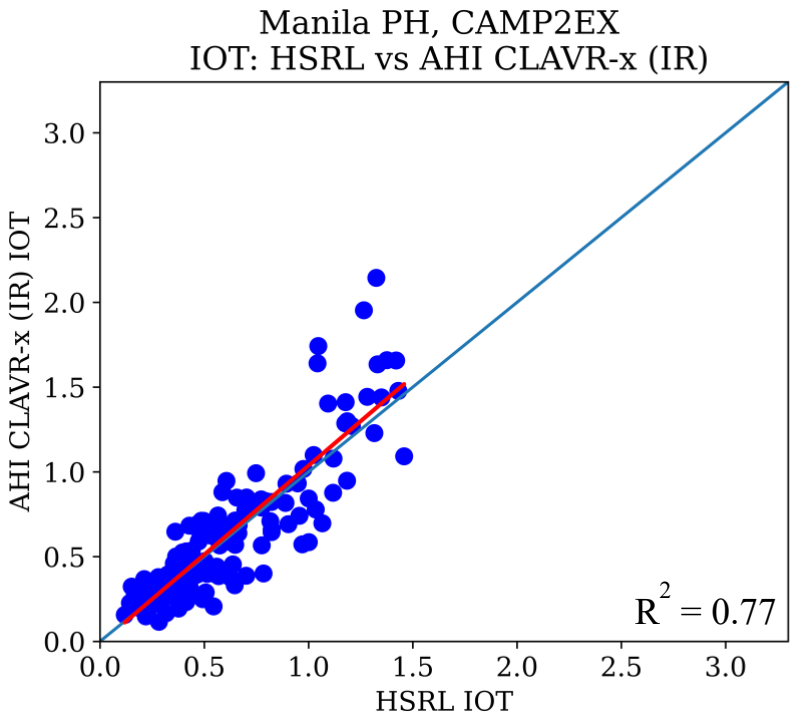

Figure 22 - Validation of the NOAA NOAA Enterprise IR optical thickness retrieval by the HSRL over an urban environment during the CAMP2EX campaign

The comparison with the HSRL suggests that the NOAA Enterprise ACHA infrared retrieval is an accurate and stable retrieval algorithm for measuring the optical thickness of thin ice clouds, even over a complex urban environment such as Manila. The correlation coefficient relative to the HSRL only drops by 0.03 from to the over ocean comparison (From $R^2 = 0.80$ to $R^2 = 0.77$) . Furthermore, this shows that the assumptions in the retrieval are well constrained such as surface temperature and emissivity that result in the I_{clr} term from equation 4 into the PFAAST radiative transfer model. These results suggest that when examining IOT over urban environments, the infrared channels should be used. In the next section, we examine the visible retrieved IOT product.s

4.1.2 Visible IOT Validation

4.1.2.1 Oceanic Environment

The corresponding NASA CLDPROP and NOAA NOAA Enterprise VIS retrieved products for the same pixels and datetimes as the infrared plots shown in the previous section for the PISTON campaign are now examined. The HSRL ICOTR developed for this study now compared to the visible retrievals with Figure 23 shows the NASA CLDPROP comparison with the HSRL.

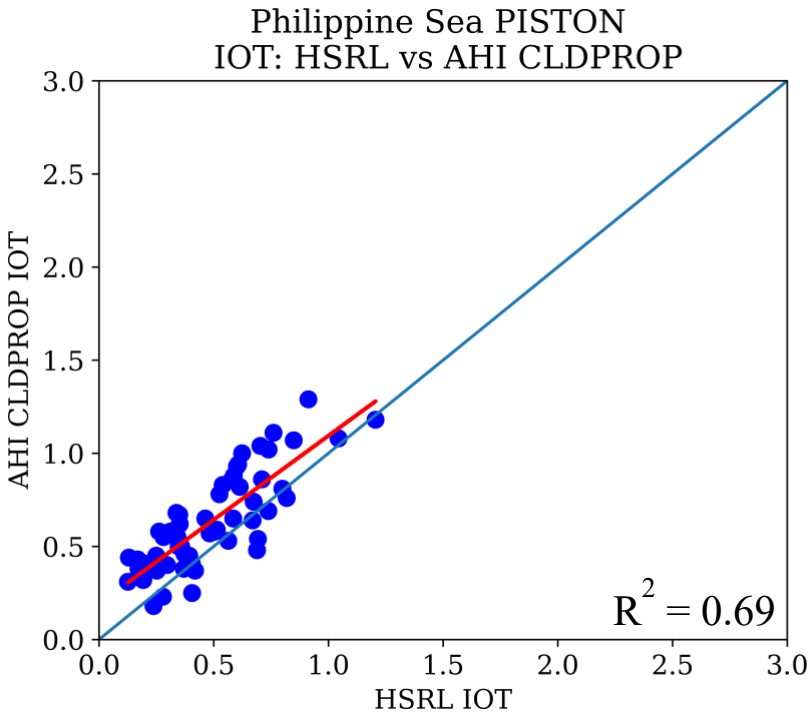

Figure 23 - Validation of the NASA CLRPROP visible optical thickness retrieval by the HSRL over ocean during the PISTON Campaign

It is observed that the NASA CLDPROP retrieval agrees well with the HSRL IOT relative to the HSRL ($R^2 = 0.69$), with a minor high bias. However, the NOAA Enterprise infrared retrieval performed better. Using the bi-spectral reflectance method, there are two major potential sources of uncertainty as we showed using equation 1 from Nakajima and King 1989. The first is the

ground albedo ($\boldsymbol{A_g}$) and the second is the scattering phase function/ asymmetry parameter (g) for the ice crystals in the cloud. As we are over ocean and the ocean surface doesn't reflect or emit heavily in the visible, only sun glint observations would positively bias the observed surface reflectance thus the optical thickness values. Because this data is quality controlled, sun glint is not an issue. These co-located observations with the HSRL provide a unique opportunity to evaluate the validity of the ice crystal scattering phase function as well as the methodology used in the retrieval. The results from the NASA CLDPROP retrieval suggests that the phase function ass umed in the retrievals is valid for the ice clouds observed in the Philippine Sea during this ship campaign. The NOAA NOAA Enterprise visible optical thickness retrieval is shown in Figure 24.

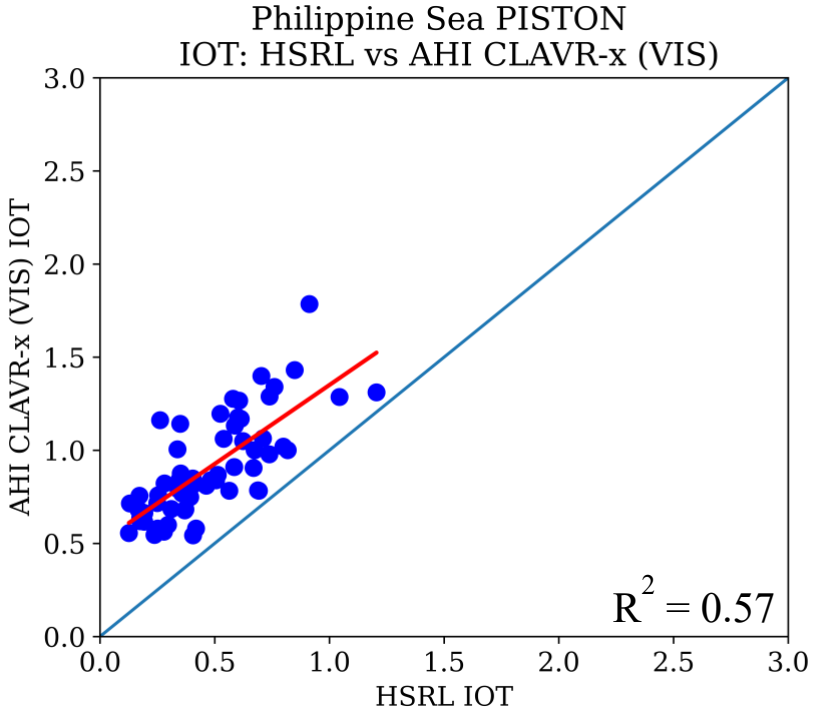

Figure 24 - Validation of the NOAA NOAA Enterprise visible optical thickness retrieval by the HSRL over ocean during the PISTON Campaign

The NOAA Enterprise visible retrieval exhibits a consistent high bias over all optical thickness values and a lower correlation than CLDPROP and NOAA Enterprise IR relative to the HSRL (R^2 = 0.57). Both the CLDPROP and NOAA Enterprise products use the MODIS white sky albedo maps (Schaaf *et al.*, 2011) and the same asymmetry parameter /phase function, that is severely roughened aggregate col umns (Yang *et al.*, 2013; Holz *et al.*, 2016). Due to these mutual assumptions, differences between the NASA CLDPROP and NOAA Enterprise products likely arose due to the different retrieval methodologies. One potential reason could be that within the optimal estimation framework if the observed reflectance values (y) have a decent agreement with the forward model output $F(x, b)$, and the chosen a-priori is higher than the IOT measured by the HSRL, the retrieval may be pulled high towards a-priori (x_a) while still meeting the cost function. The a-priori for the NOAA Enterprise visible retrieval is from CALIPSO climatology. As the ice clouds measured here are a subset of the climatological record, this is not entirely unexpected. The implications of these results suggest that the phase function used in these retrievals is valid for this part of the world and that the NASA CLDPROP optical thickness retrieval can be used for single-layer ice cloud observations for energy budget and other science applications over the ocean in the validated region.

4.1.2.2 Urban Environment

With the NASA CLDPROP retrieval agreeing well with the HSRL over the ocean, we now have confidence that the asymmetry parameter assumed in the retrieval is valid for this region. We can now examine the validity of both retrievals over an environment with the added uncertainty of a complex surface Bidirectional Reflectance Distribution Function. The BRDF describes the angular reflection of radiation off an opaque surface. Figure 25 shows the HSRL-

derived IOT compared to the NASA CLDPROP (A) and the NOAA NOAA Enterprise retrieval (B).

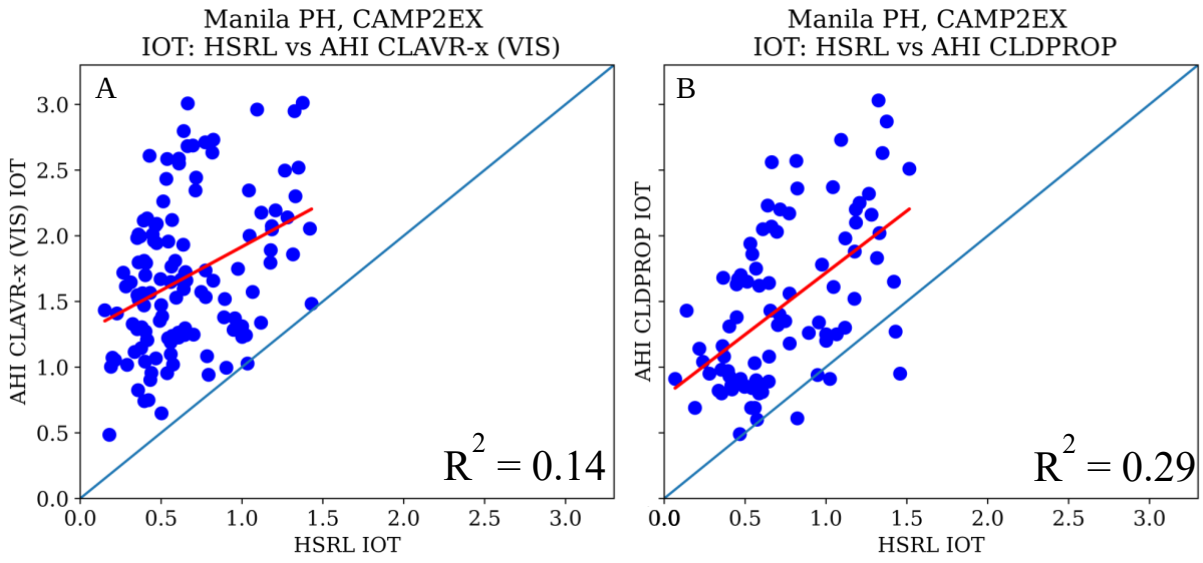

Figure 25 - Validation of the NOAA NOAA Enterprise visible (A) and NASA CLDPROP (B) optical thickness retrievals by the HSRL over an urban environment during the CAMP2EX campaign

The two retrievals both exhibit a similar large high bias and increased uncertainty within the spread of that bias. The correlation is low with the HSRL for both the NOAA Enterprise VIS ($R^2 = 0.14$) and CLDPROP ($R^2 = 0.29$). Due to the results of the NASA CLDPROP retrieval over ocean, and the comparison of the infrared NOAA Enterprise retrieval over both land and ocean, we can safely assume that the uncertainty associated with the NASA CLDPROP and NOAA Enterprise visible retrievals shown here stem from an under-estimation of the surface reflection function. The high bias in each retrieval product is further examined in figure 26 by plotting the HSRL IOT against the optical thickness ratio as shown in equation 44.

$$39.\ Optical\ Thickness\ Ratio = \frac{AHI\ Retrieved\ Optical\ Thickness}{HSRL\ Optical\ Thickness}$$

Where the HSRL IOT is taken as the "truth" measurement. A value of 1 represents perfect agreement with the HSRL IOT and is indicated by the horizontal black line, while a value of 2 or 3 would correspond to a high bias with double or triple the value of the HSRL respectively.

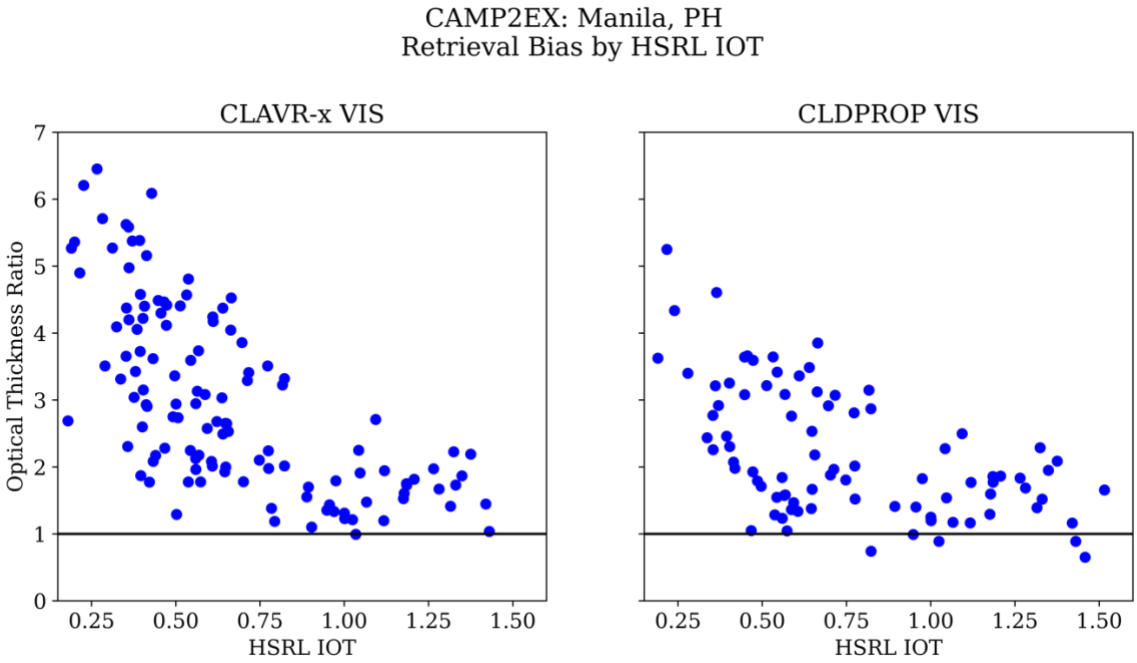

Figure 26 - Optical Thickness Ratio (Bias) by HSRL IOT for the NASA CLDPROP and NOAA Enterprise visible retrievals

The figure shows a logarithmic decrease in the bias as the HSRL IOT approaches unity. This is likely due to the decrease in transmitted reflected upwelling surface radiation through the cloud layer due to higher IOT values. As shown in equation 1, the higher optical thickness values result in a smaller atmospheric transmittance (t_{atm}), which results in a decrease in the surface reflectance terms (2nd term) contribution to the top of the atmosphere reflectance. Some of the

low IOT values from the HSRL with the highest biases in the NOAA Enterprise data are not present in the CLDPROP data. This is likely because the reflectance values fall out of the look-up table, while in the NOAA Enterprise the optimal estimation is driven to higher values by the a priori that still meet the cost function condition. The surface BRDF for both retrieval algorithms is derived using clear sky observations of the surface using MODIS. Figure 21 shows high-resolution visible imagery from google earth regarding the surface environment of Manila. It can be seen that this region has a very complicated surface, with asphalt, sheet metal roofs, and occasional vegetative pockets. These results suggest that one should use extreme caution when using visible optical property retrievals of ice cloud optical thickness for thin ice clouds over urban environments without validation at that location via lidar.

4.1.2.3 Impacts of Radiometric Calibration on NASA CLDPROP Yield

The NASA Cloud Property Algorithm was originally designed for the MODIS and VIIRS sensors. The early implementation of the NASA CLDPROP algorithm on MODIS and VIIRS resulted in inter-sensor biases in the optical property retrievals (Meyer *et al.*, 2020). These inconsistencies were traced back to relative radiometric inconsistencies between analogous channels of the two instruments. When the NASA CLDPROP algorithm was implemented on the AHI, there was a small difference in the calibration of the 2.25 channel used for the bi-spectral reflectance method. The 2.25 um channel was dimmer. The reflectance values measured by the sensor at the 0.86 and 2.25 are used to simultaneously determine optical thickness and effective radius over ocean. As shown in Figure 7, the solution space in the look up table becomes smaller with decreasing IOT values and decreasing reflectance in the used channels The radiometric correction in the 2.25 channel resulted in an increase in the 0.84 and 2.25 channel point in the

look up table falling into the solution space. As shown in Figure 27, the increase in yield was highest for small IOT values indicated by the HSRL, especially for values under one.

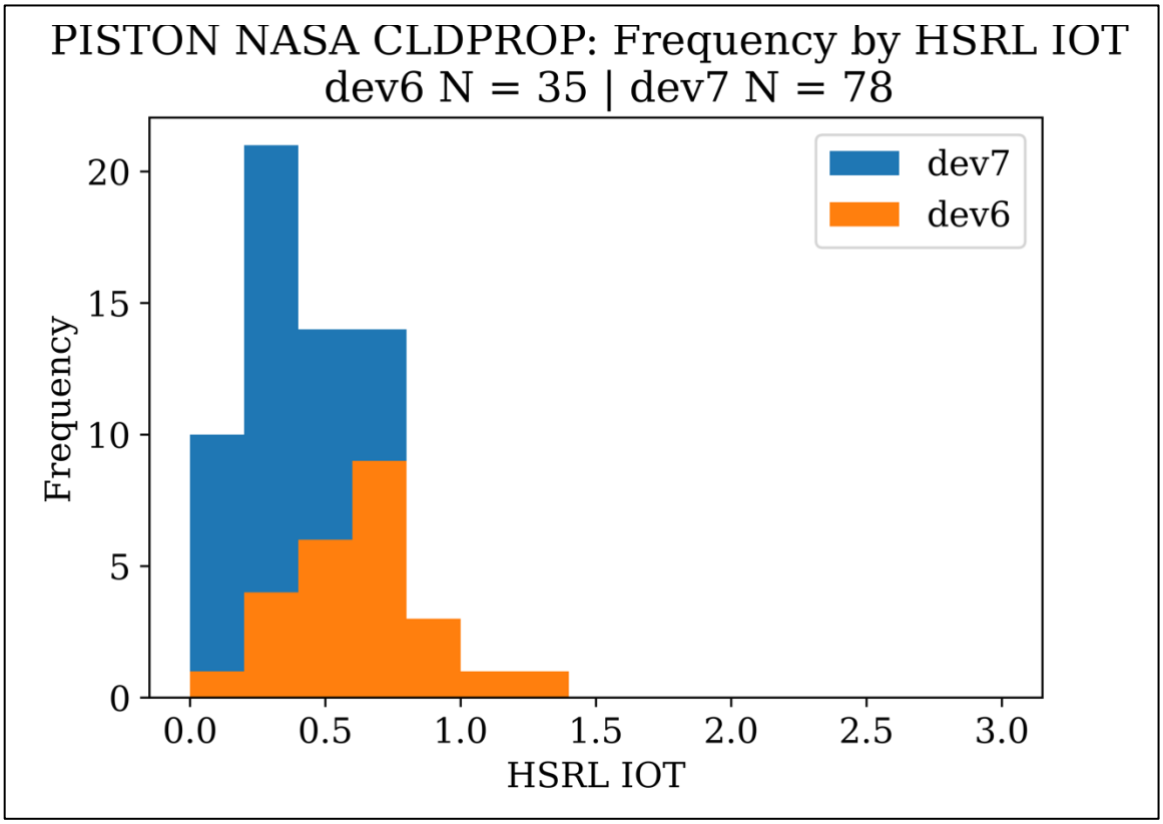

Figure 27 – Improvement in yield due to improved radiometric calibration by binned HSRL optical depth for the NASA CLDPROP

The overall yield relative to the previous version without radiometric corrections in the 2.25 channels was 120.5 % for the optically thin ice clouds during PISTON.

4.2 Comparison of NASA Cloud Property Retrieval from AHI with MODIS and VIIRS

In the previous sections, the NASA CLDPROP and NOAA NOAA Enterprise retrievals run on the AHI instrument for both urban and ocean environments were validated. The NASA CLDPROP retrieval agreed very well with the HSRL data collected over ocean during the

PISTON campaign for single layer homogeneous ice clouds. The SSEC SIPPS had preprocessed NASA CLDPROP data available for AHI on Himawari-8, MODIS on AQUA and VIIRS on SNPP for the mutual time period of September 2019, enabling the comparison of the same retrieval on multiple platforms. NOAA NOAA Enterprise data during the months of the PISTON campaign for MODIS and VIIRS will not be analyzed due to lack of available data. There are two goals of this section; the first is to compare one month of CLDPROP data processed on AHI over the PISTON domain to CLDPROP data processed on MODIS and VIIRS. The second is to use AHI as an anchor to determine qualitatively how well the AHI-HSRL based result can translate to MODIS and VIIRS for optically thin ice clouds (IOT < 3). This approach is taken due to the difficulty of obtaining a statistically significant n umber of HSRL co-locations with individual LEO sensors during the PISTON campaign.

The dataset is first constrained to only ice clouds indicated by both instruments' optical phase retrievals. Then, to ensure the most accurate comparison possible, the co-located dataset is filtered to include MODIS and VIIRS averaged IOT values with low spatial homogeneity across the AHI pixel. The impact of reducing the absolute scattering and view angle differences is investigated for the entire IOT range and the statistical correlation between the GEO and LEO products are calculated for thin, opaque, and thick cloud indicated by Hong et al. 2017. The data is also constrained to low view and scattering angle differences to produce a better statistical comparison.

4.2.1 All Optical Depth Ranges

Figure 28a and Figure 29a show the IOT product from AHI compared to its MODIS and VIIRS counterpart products respectively.

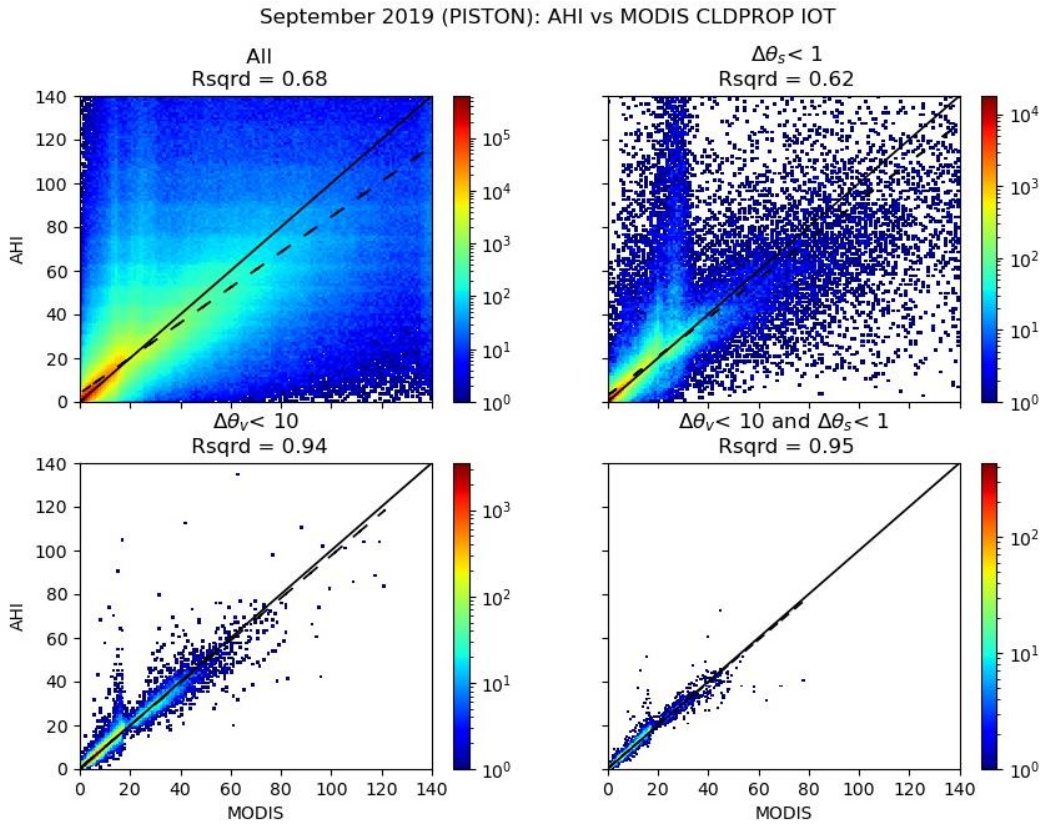

Figure 28- Comparison of the NASA CLDPROP retrieved IOT for AHI and MODIS for the entire optical depth range over the PISTON domain

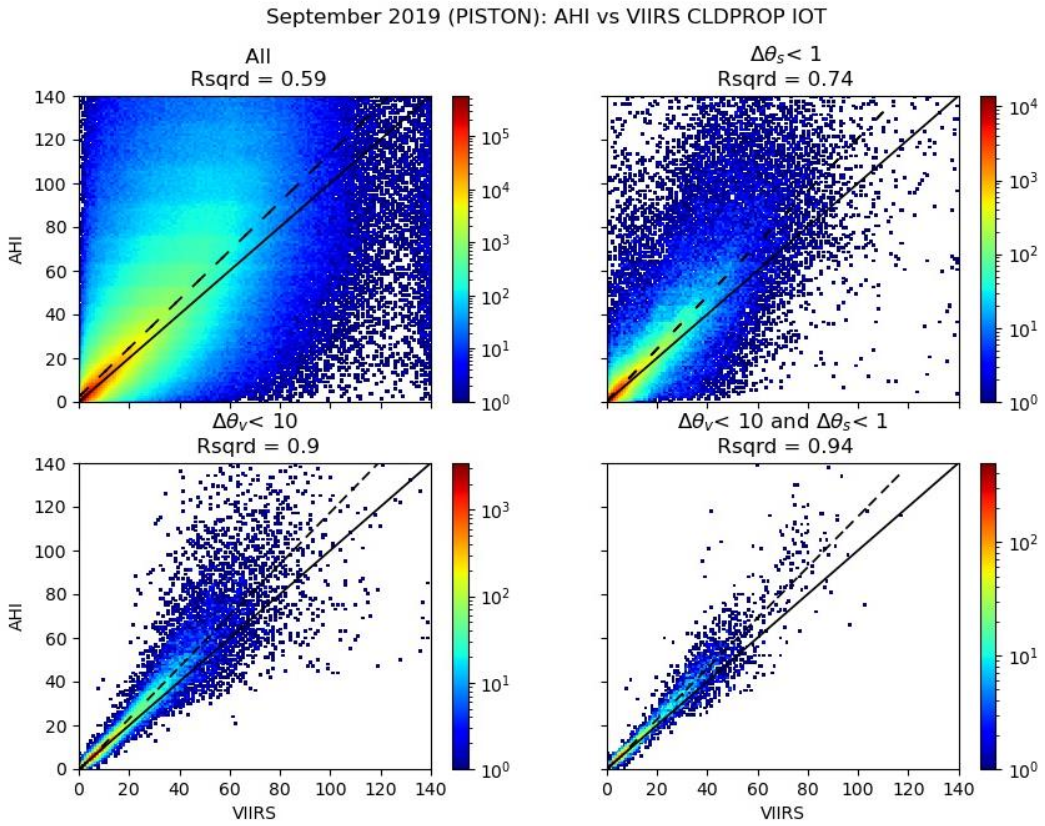

Figure 29- Comparison of the NASA CLDPROP retrieved IOT for AHI and VIIRS for the entire optical depth range over the PISTON domain

It can be observed that the correlations for all ice phase cloud are moderate (MODIS: R^2 = 0.68 ; VIIRS: R^2 = 0.59), however this can be expected as view angle geometries have not yet been accounted for. The view angle difference is the angular difference between two line of sight vectors from the ground to the two respective imagers. Figure 30 shows the linear correlation between VIIRS and AHI as a function of the maxim um absolute view ($\Delta\theta_v$) and scattering angle

($\Delta\theta_s$) differences.

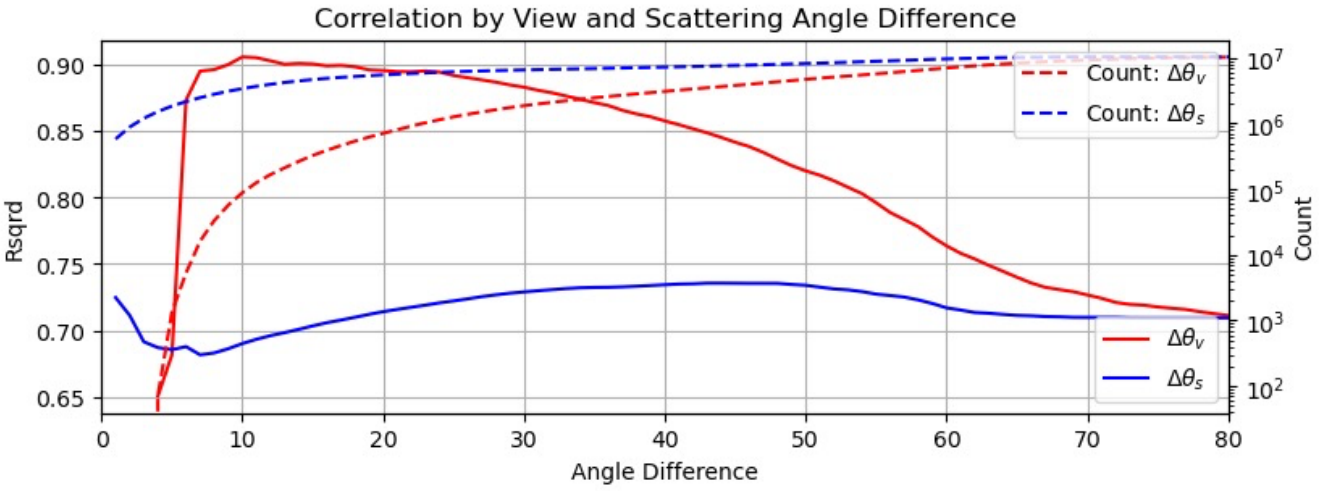

Figure 30 – Correlation of AHI and VIIRS for different maxim um view angle and scattering angle differences

The solid blue line is the absolute scattering angle difference, and the solid red line is the absolute view angle difference with the dashed lines being the total count. The correlation from the scattering angle alignment was minimal overall but showed some improvement for the minimal extremes $\Delta\theta_s < 1$ for VIIRS. Alignment in view angle differences were unsurprisingly shown to have a large impact and accounted for about 31% (VIIRS) and 26% (MODIS) of the unquantified uncertainty between the datasets when confined to $\Delta\theta_v < 10$ relative to all view angles considered. Figure 28d and figure 29d show the MODIS and VIIRS IOT products constrained by $\Delta\theta_s < 1$ and $\Delta\theta_v < 10$ over the entire optical depth range and yield a correlation coefficient of 0.95 and 0.94 respectively. This is a very positive result over the entire optical depth range, and it also suggest that when comparing visible cloud products, the view angles must be aligned to investigate inter-sensor uncertainties. In the following section we will examine how this comparison holds up over difference optical depth ranges categorized by their radiative impact as outlined in Hong et al. 2017.

4.2.2 Comparison for Thin, Opaque and Thick IOT

Here, we repeat the above comparison in the previous section, but for the subset of optical depth ranges described in Hong et al. 2017. These optical depth ranges are thin (IOT = 0.3 – 3), opaque (3 < IOT < 20) and thick (IOT > 20). We will start with thin ice clouds because this is the optical depth range that is closest to the PISTON HSRL dataset. For thin ice clouds, the correlation for non-angle aligned IOT measurements is low, (MODIS: $R^2 = 0.37$; VIIRS: $R^2 = 0.32$) and is shown in Figures 31A and 32A. It can be observed that the n umber density of the spread (red in density plot) is larger for VIIRS than MODIS. When only considering measurements that meet the view angle and scattering angle alignment criteria, the correlation is significantly higher (MODIS: $R^2 = 0.82$; VIIRS: $R^2 = 0.75$). This increase in correlation due to the angle alignment is higher for optically thin clouds than any other optical depth range (as indicated by the $+R^2$; MODIS: $+R^2 = 0.45$; VIIRS: $+R^2 = 0.43$). It should also be noted that MODIS has higher agreement with AHI than VIIRS for this range ($+R^2 = 0.07$) and could be due MODIS being closer in spatial resolution to AHI. Overall, MODIS and VIIRS agree well with AHI for optically thin ice clouds that have an overall net warming effect.

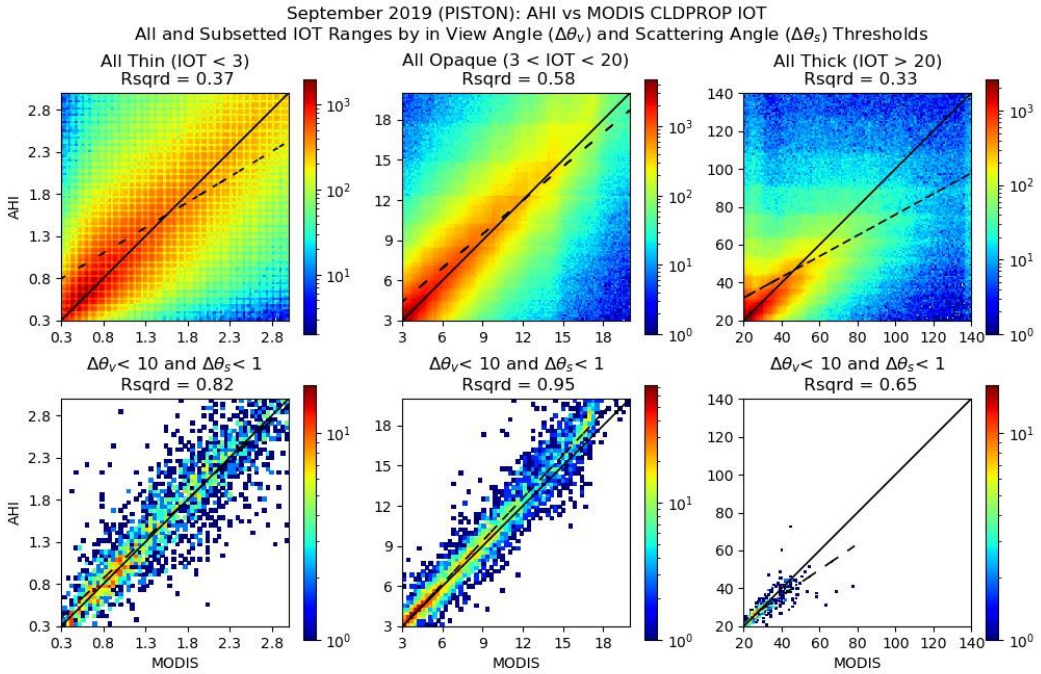

Figure 31 - Comparison of the NASA CLDPROP retrieved IOT for AHI and MODIS for thin, opaque and thick optical depth ranges

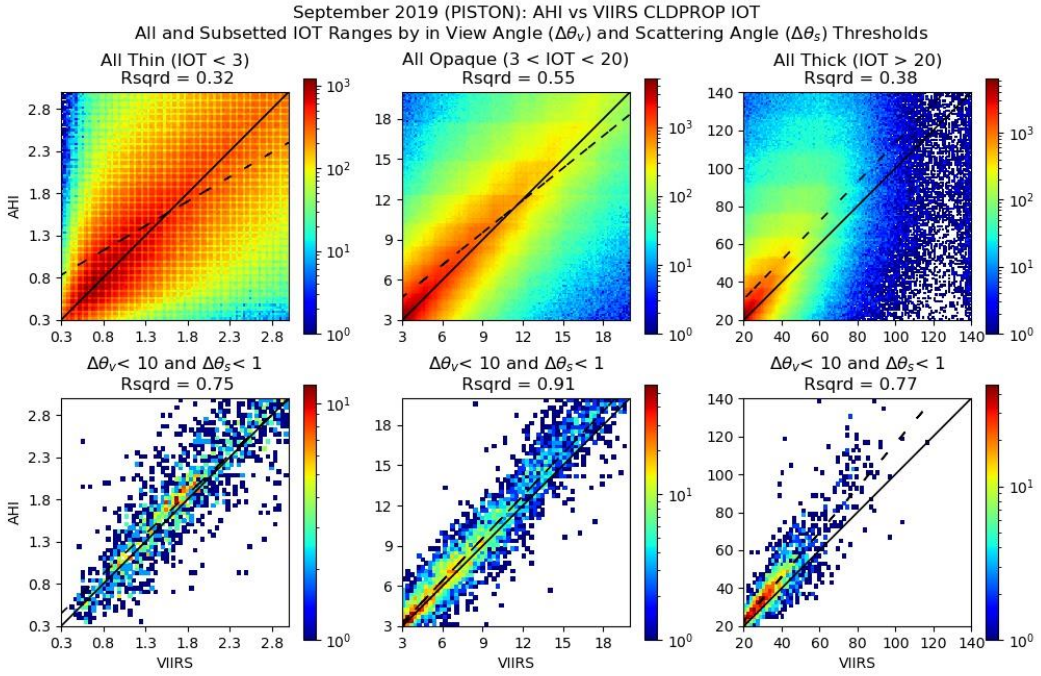

Figure 32 - Comparison of the NASA CLDPROP retrieved IOT for AHI and VIIRS for thin, opaque and thick optical depth ranges

Opaque ice clouds (3 < IOT < 20) have higher agreement with AHI for both instruments than any other optical depth range. Both instruments are moderately correlated before the view angle subset criteria (MODIS: $R^2 = 0.58$; VIIRS: $R^2 = 0.55$) and highly correlated after the subset (MODIS: $R^2 = 0.95$; VIIRS: $R^2 = 0.91$). MODIS and VIIRS agree extremely well with each other in regards to opaque ice clouds, which can have a net warming or cooling effect depending on their exact optical depth. Thick ice clouds (20 < IOT < 140) are weakly correlated before the view angle subset criteria (MODIS: $R^2 = 0.33$; VIIRS: $R^2 = 0.38$) and moderately and highly correlated after the subset (MODIS: $R^2 = 0.65$; VIIRS: $R^2 = 0.77$) respectively. The correlation is overall moderate for this subset of ice clouds with a net cooling effect.

4.2.3 Comparison of Regression Coefficients

In this section, we will examine if the HSRL validation of CLDPROP on AHI is statistically translatable to CLDPROP on MODIS and VIIRS. This will be done by comparing the regression coefficients generated by regressing the HSRL, MODIS and VIIRS against AHI. Before the regression, we roughly restrict the optical depth range of MODIS and VIIRS to the PISTON HSRL dataset. Figure 33 shows the best fit line generated by the regression for the HSRL validation of AHI IOT during PISTON as well as the MODIS and VIIRS AHI

comparisons during PISTON

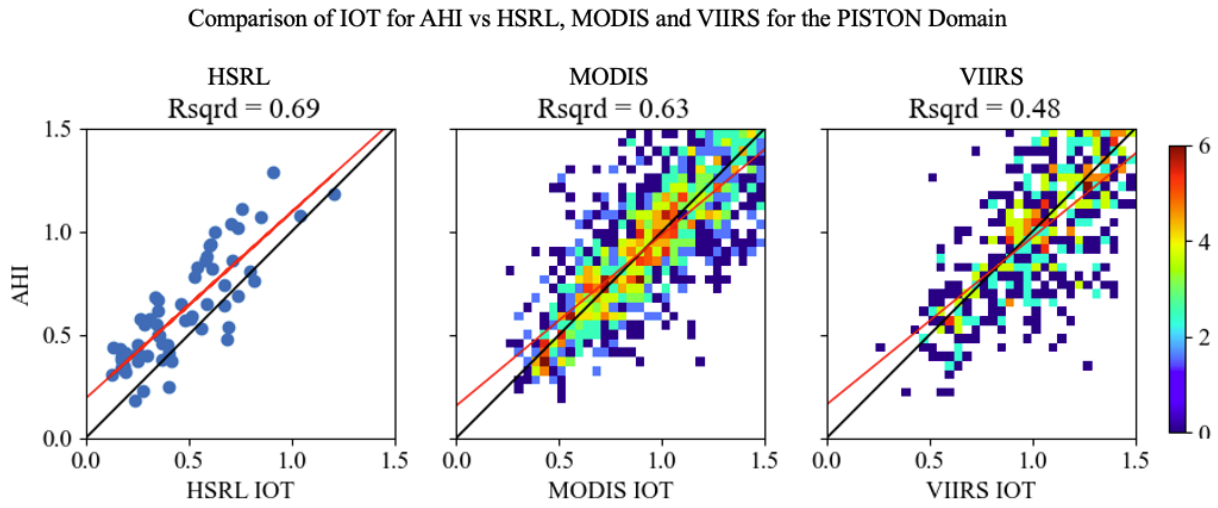

Figure 33 - Comparison of the NASA CLDPROP retrieval processed on AHI with the HSRL, MODIS and VIIRS over the PISTON domain for IOT < 1.5.

It can be observed that the regression line (red) is visually similar in all figures and that each instruments product shows a low bias relative to AHI for IOT < ~0.85. Furthermore, it can be seen that VIIRS is lacking measurements for IOT < 0.5. The regression coefficients such as the slope, y-intercept (mean linear bias) as well as their associated uncertainties are extracted for

each comparison and are shown in figure 34.

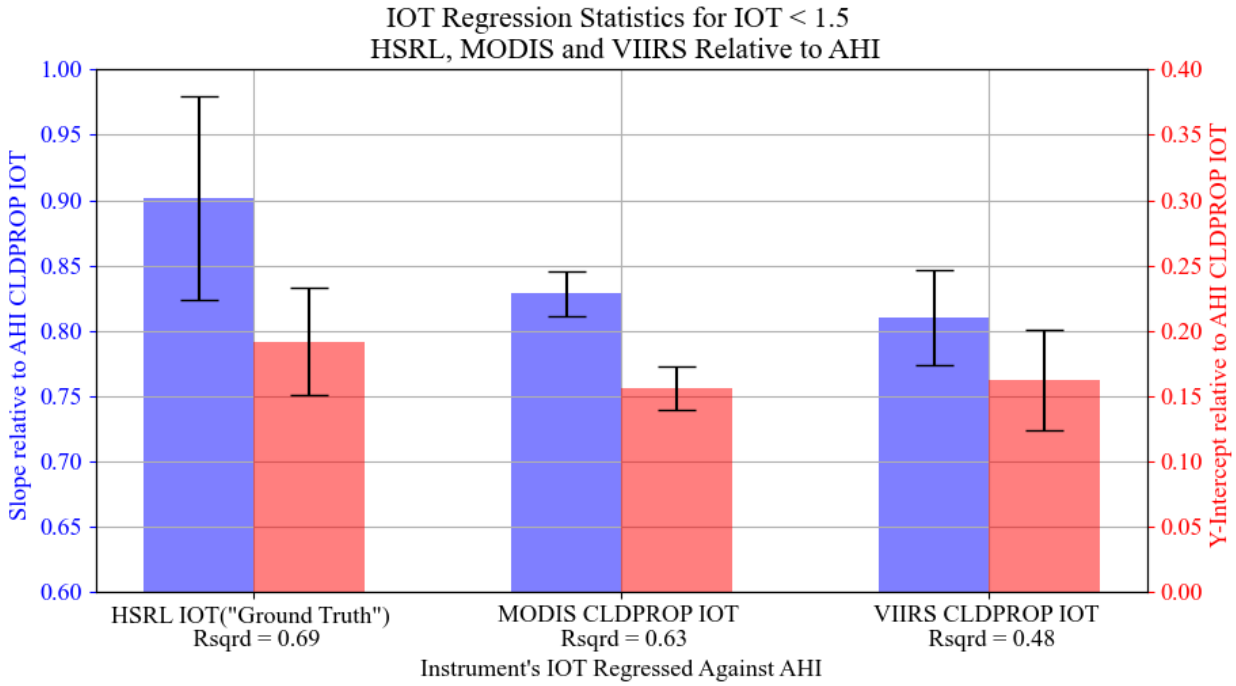

Figure 34 – Comparison of regression coefficients for the comparison of NASA CLDPROP retrieval processed on AHI vs the HSRL, MODIS and VIIRS over the PISTON domain. The blue bar corresponding to the left y axis is the slope relative to AHI and the red bar is the mean linear bias relative to AHI

The comparison of the regression coefficients of the HSRL-AHI and MODIS-AHI regressions show that the slopes (0.9 +/- 0.08 and 0.83 +/- 0.02) and y-intercepts (0.19 +/- 0.04 and 0.16 +/ 0.02) are within the bounds of uncertainty of each other. The same is true for the VIIRS-AHI slope (0.81 +/- 0.04) and y-intercept (0.16 +/- 0.04). This suggests that these results may translate to MODIS and VIIRS. It should be stated however, that direct in-situ validation using the HSRL directly co-located with MODIS and VIIRS over a well behaved BRDF environment is the best way to validate these retrievals on each instr ument.

5. Summary and Conclusions

The necessity to examine changes in cloud frequency and optical properties due to greenhouse gases for energy budget applications and climate sensitivity studies facilitate the

need to construct a highly accurate and stable cloud data record extending three decades or more. The MODIS-VIIRS cloud continuity (NASA Cloud Property Retrieval) and the NOAA Enterprise (NOAA Clouds from the AVHRR extended system) algorithms aim to construct an inter-satellite data record to investigate these trends. The optical depth plays a primary role in the net radiative effect of an ice cloud, which motivates the validation of this key parameter. The goal of this thesis was to create an ice cloud property retrieval for the HSRL with uncertainty estimated to validate the cloud optical thickness products from the NASA CLDPROP and NOAA NOAA Enterprise retrievals during the CAMP2EX and PISTON field campaigns as well as examine the validity of the assumptions made in these operational retrievals. The advancement in GEO satellite technology allows for these LEO retrieval algorithms to be accurately run on the AHI instrument. Utilizing the HSRL's unique ability to determine optical depth and particulate backscatter by separating the molecular and particulate signals, a highly accurate ice cloud optical thickness retrieval with quantifiable uncertainties was developed for this validation effort to detect ice clouds and determine IOT. Using extremely rare and valuable HSRL ship-based measurements during PISTON, all three retrievals were validated under the most optimal conditions possible. The over-ocean measurements allowed for the investigation into the validity of the scattering phase function and surface assumptions independently. The NASA CLDPROP from AHI is also compared to CLDPROP processed on MODIS AQUA and VIIRS SNPP.

It was shown that the NOAA Enterprise infrared retrieval has the highest agreement with the HSRL instrument ($R^2 = 0.80$, Ocean; $R^2 = 0.77$, Urban), with the NASA Cloud Property retrieval performing well over the ocean ($R^2 = 0.69$, Ocean; $R^2 = 0.29$, Urban). The NOAA Enterprise visible retrieval has a high bias over both land and ocean ($R^2 = 0.57$, Ocean; $R^2 =$

0.14, Urban), likely due to its optimal estimation methodology as it shared assumptions regarding the phase function and surface albedo with NASA CLDPROP. All R squared values for all validation efforts are s ummarized below in Table 3.

Correlation Coefficients (R^2) for the AHI – HSRL Validation Effort

	NOAA CLAVR-x Infrared	NASA CLDPROP	NOAA CLAVR-x Visible
PISTON Philippine Sea (Oceanic)	0.80	0.69	0.57
CAMP2EX Manila, PH (Urban)	0.77	0.29	0.14

Table 3 - R squared values for all validated retrievals

The results of the NASA Cloud Property retrieval suggest for the ice clouds in the Philippine Sea region during August – September of 2018 the assumed phase function in the retrieval was valid. This is a significant finding and builds upon the work of Holz et al. 2016. Overland at the urban site of Manila, the only retrieval that performed well was the NOAA Enterprise infrared retrieval, with the two visible retrievals performing poorly due to a poorly constrained surface BRDF. Furthermore, the quantifiable variance in the R^2 only decreased by 0.03, showing the robustness of this retrieval algorithm to the urban surface environment. This validation effort suggests that the visible retrievals should not be used over urban environments for scientific investigations where thin ice clouds are an important parameter until the surface reflection contribution has been better constrained. The high bias in optical thickness would result in an overestimation of the shortwave cooling and an overestimation of the longwave warming. Future

research must be done to better constrain the surface BRDF of urban environments for visible retrievals. Over the ocean, the NASA CLDPROP retrieval could be used, however, the NOAA Enterprise infrared retrieval has higher agreement with the HSRL. Overall, there are two important findings from this work: 1) The first is that the phase function utilized in the visible retrieval is valid for the clouds measured in PISTON (ei: severely roughened aggregate crystals from Yang et al. 2013 and Holz et al. 2016). 2) The infrared channels are the most effective passive method to obtain IOT for thin ice clouds. With the fact that these passive observations also offer night-time coverage, infrared radiometers should be heavily considered for any future mission that wants to measure cirrus cloud optical thickness.

Obtaining a statistically significant number of MODIS and VIIRS co-located measurements with the HSRL for single-layer optically thin ice clouds that meet the requirements outlined in this study for the PISTON ship campaign was not possible. Therefore, the validated NASA CLDPROP retrieval processed on AHI is compared to the CLDPROP retrieval processed on MODIS AQUA and VIIRS SNPP over the PISTON domain. It was shown that the MODIS and VIIRS products agree very well with those validated on AHI for view angle differences less than 10 degrees over all optical depth ranges (MODIS $R^2 = 0.95$ and VIIRS $R^2 = 0.94$). This shows that to compare geostationary and low earth orbing visible cloud optical depth measurements, the view angle difference should be restricted to less than 10 degrees for an accurate comparison. For all optical depth ranges, the instruments agreed best with AHI for optically opaque clouds. When comparing the regression coefficients generated by the HSRL-AHI IOT comparison during PISTON to the MODIS-AHI and VIIRS-AHI comparisons for IOT < 1.5, the coefficients suggest these results may be applicable to MODIS and VIIRS.

Although the validation effort outlined in this thesis showed positive results for the assumed phase function, more HSRL validation efforts are required. The motivation for further validation is the current phase function implemented in the retrievals was determined by bringing the MODIS C6 visible retrieval into an agreement with an infrared retrieval in a global statistical sense (Holz *et al.*, 2016), but did not account for regional or seasonal variation. To account for varying ice crystal morphology, which as been shown to be dependent on atmospheric conditions such as temperature and ice saturation (Bailey and Hallett, 2009) the comparison should be repeated in different locations and seasons that may contain different ice crystals under well-quantified surface BRDF conditions.

Although for optically thick ice clouds, polarimeter studies by Van Diedenhoven et al. 2020 have shown slight global variation in the annual asymmetry parameter. By utilizing polarimeter measurements such as these or in-situ measurements obtained by a cloud particle imager combined with knowledge of well-quantified surface BRDF environments (such as ocean and grasslands) strategic locations can be chosen to validate different ice cloud morphologies. It is difficult to choose a location with different ice cloud morphologies without having available information on the ice crystal morphology of regions by season. Furthermore, different seasons may bring more difficult surface BRDF environments to account for such as snow or ice, which must be considered. An in-depth analysis should be performed to choose the most optimal locations for HSRL deployment that considers both a variation in ice crystal morphology and a well-quantifiable surface BRDF to validate different ice cloud morphologic environments. Based on the results of a future validation effort, a global phase function assumption may be maintained or a regional or conditional phase function assumption may be adopted. The HSRL site of the southern great plains good data record under a well-quantified surface BRDF for validation,

however, the ice crystal morphology should be shown to be different than in this study so that a unique ice crystal morphology can be validated.

The results of this work suggest that the surface BRDF of urban environments needs to be re-visited. To improve the surface BRDF assumption from geostationary orbit one can use a lidar such as the HSRL in combination with the highest high-resolution channel (red band) to find cloud and aerosol-free measurements within the region of interest and map the surface BRDF. This clear sky BRDF can then be used as an assumption within the retrieval to attempt to make a visible IOT retrieval.

Acknowledgments

This thesis is dedicated to my partner, family, and friends who have supported me during my time at UW-Madison. It has been a life goal of mine to be a scientist since I saw the launch of the TERRA at Vanderburg Airforce Base when I was 4 years old and receiving this M.S.degree is a step on that journey. I want to specifically thank my partner Chelsy for always standing by me and supporting me. I also want to specifically thank my father for his mentorship in life, peaking my interest in science at a young age, and for showing me how to appreciate nature. I also want to thank my committee for their comments as well as my research advisor Bob Holz for working with me.

References

1. Bailey, M. P. and Hallett, J. (2009) 'A Comprehensive Habit Diagram for Atmospheric Ice Crystals: Confirmation from the Laboratory, AIRS II, and Other Field Studies', *Journal of the Atmospheric Sciences,* 66(9), pp. 2888-2899.
2. Baran, A. J. (2012) 'From the single-scattering properties of ice crystals to climate prediction: A way forward', 112, pp. 45-69.
3. Barnes, W. L., Pagano, T. S. and Salomonson, V. V. (1998) 'Prelaunch characteristics of the Moderate Resolution Imaging Spectroradiometer (MODIS) on EOS-AM1', *IEEE Transactions on Geoscience and Remote Sensing,* 36(4), pp. 1088-1100.
4. Baum, B. A., Heymsfield, A. J., Yang, P. and Bedka, S. T. (2005) 'Bulk Scattering Properties for the Remote Sensing of Ice Clouds. Part I: Microphysical Data and Models', 44(12), pp. 1885-1895.
5. Cesana, G. and Storelvmo, T. (2017) 'Improving climate projections by understanding how cloud phase affects radiation', *Journal of Geophysical Research: Atmospheres,* 122(8), pp. 4594-4599.
6. Chahine, M. T. (1974) 'Remote Sounding of Cloudy Atmospheres. I. The Single Cloud Layer', *Journal of the Atmospheric Sciences,* 31(1), pp. 233-243.
7. Cooper, S. J., L'Ecuyer, T. S. and Stephens, G. L. (2003) 'The impact of explicit cloud boundary information on ice cloud microphysical property retrievals from infrared radiances', *Journal of Geophysical Research: Atmospheres,* 108(D3).

8. Da, C. (2015) 'Preliminary assessment of the Advanced Himawari Imager (AHI) measurement onboard Himawari-8 geostationary satellite', *Remote Sensing Letters,* 6(8), pp. 637-646.
9. Eloranta, E. (2005) 'High Spectral Resolution Lidar', *Springer Series in Optical Sciences*. Springer, New York, NY.: Springer.
10. Fauchez, T., Platnick, S., Sourdeval, O., Wang, C., Meyer, K., Cornet, C. and Szczap, F. (2018) 'Cirrus Horizontal Heterogeneity and 3-D Radiative Effects on Cloud Optical Property Retrievals From MODIS Near to Thermal Infrared Channels as a Function of Spatial Resolution', *Journal of Geophysical Research-Atmospheres,* 123(19), pp. 11141-11153.
11. Fu, Q. (2007) 'A New Parameterization of an Asymmetry Factor of Cirrus Clouds for Climate Models', 64(11), pp. 4140-4150.
12. Goldsmith, J. (2016) *High Spectral Resolution Lidar*
13. *Instrument Handbook.* U.S Department of Energy, Office of Sciences.
14. Heidinger, A. 2015. Algorithm Theoretical Basis Document: AWG Cloud Height Algorithm (ACHA).
15. Heidinger, A. 2020. Advanced Theoretical Document: NOAA Enterprise Cloud Mask.
16. Heidinger, A., Sullivan, J. and Rao, C. N. (2003) 'Calibration of visible and near-infrared channels of the NOAA-12 AVHRR using time series of observations over deserts', *International Journal of Remote Sensing,* 24(18), pp. 3635-3649.
17. Heidinger, A. K., Cao, C. and Sullivan, J. T. (2002) 'Using Moderate Resolution Imaging Spectrometer (MODIS) to calibrate advanced very high resolution radiometer

reflectance channels', *Journal of Geophysical Research: Atmospheres,* 107(D23), pp. AAC 11-1-AAC 11-10.

18. Heidinger, A. K., Li, Y., Baum, B. A., Holz, R. E., Platnick, S. and Yang, P. (2015) 'Retrieval of Cirrus Cloud Optical Depth under Day and Night Conditions from MODIS Collection 6 Cloud Property Data', *Remote Sensing,* 7(6), pp. 7257-7271.
19. Heidinger, A. K. and Pavolonis, M. J. (2009) 'Gazing at Cirrus Clouds for 25 Years through a Split Window. Part I: Methodology', *Journal of Applied Meteorology and Climatology,* 48(6), pp. 1100-1116.
20. Hillger, D. W., Schmit, T. J. and Daniels, J. M. 2003. Imager and sounder radiance and product validations for the.
21. Hlavka, D. L., Yorks, J. E., Young, S. A., Vaughan, M. A., Kuehn, R. E., McGill, M. J. and Rodier, S. D. (2012) 'Airborne validation of cirrus cloud properties derived from CALIPSO lidar measurements: Optical properties', *Journal of Geophysical Research: Atmospheres,* 117(D9).
22. Holz, R. E. (2002) *Measurements of cirrus backscatter phase functions using a high spectral resolution lidar.* M s, University of Wisconsin--Madison.
23. Holz, R. E., Platnick, S., Meyer, K., Vaughan, M., Heidinger, A., Yang, P., Wind, G., Dutcher, S., Ackerman, S., Amarasinghe, N., Nagle, F. and Wang, C. (2016) 'Resolving ice cloud optical thickness biases between CALIOP and MODIS using infrared retrievals', 16(8), pp. 5075-5090.

24. Hong, Y., Liu, G. and Li, J. L. F. (2016) 'Assessing the Radiative Effects of Global Ice Clouds Based on CloudSat and CALIPSO Measurements', *Journal of Climate,* 29(21), pp. 7651-7674.

25. ICCP 2021. STATEMENT ON THE ROLE OF CLOUDS AND PRECIPITATION ON CLIMATE CHANGE.

26. Inoue, T. 1985. On the temperature and effective emissivity determination of semi-transparent cirrus clouds by bispectral measurements in the 10 micron window region.

27. Jiang, J. H., Su, H., Zhai, C., Perun, V. S., Del Genio, A., Nazarenko, L. S., Donner, L. J., Horowitz, L., Seman, C., Cole, J., Gettelman, A., Ringer, M. A., Rotstayn, L., Jeffrey, S., Wu, T., Brient, F., Dufresne, J.-L., Kawai, H., Koshiro, T., Watanabe, M., LÉcuyer, T. S., Volodin, E. M., Iversen, T., Drange, H., Mesquita, M. D. S., Read, W. G., Waters, J. W., Tian, B., Teixeira, J. and Stephens, G. L. (2012) 'Evaluation of cloud and water vapor simulations in CMIP5 climate models using NASA “A-Train” satellite observations', *Journal of Geophysical Research: Atmospheres,* 117(D14).

28. Johnson, E., Galang, K., Ranshaw, C. and Robinson, B. (2010) *NPP Visible/Infrared Imaging Radiometer Suite (VIIRS) radiometric calibration emissive bands: tested performance. SPIE Optical Engineering + Applications*: SPIE, p. OPO.

29. Kalluri, S., Alcala, C., Carr, J., Griffith, P., Lebair, W., Lindsey, D., Race, R., Wu, X. and Zierk, S. (2018) 'From Photons to Pixels: Processing Data from the Advanced Baseline Imager', *Remote Sensing,* 10(2), pp. 177.

30. King, M. D. (1987) 'Determination of the Scaled Optical Thickness of Clouds from Reflected Solar Radiation Measurements', *Journal of the Atmospheric Sciences,* 44(13), pp. 1734-1751.
31. King, M. D., Platnick, S., Yang, P., Arnold, G. T., Gray, M. A., Riedi, J. C., Ackerman, S. A. and Liou, K.-N. (2004) 'Remote Sensing of Liquid Water and Ice Cloud Optical Thickness and Effective Radius in the Arctic: Application of Airborne Multispectral MAS Data', *Journal of Atmospheric and Oceanic Technology,* 21(6), pp. 857-875.
32. Klett, J. D. (1981) 'Stable analytical inversion solution for processing lidar returns', *Applied Optics,* 20(2), pp. 211-220.
33. Lee, J., Yang, P., Dessler, A. E., Gao, B.-C. and Platnick, S. (2009) 'Distribution and Radiative Forcing of Tropical Thin Cirrus Clouds', 66(12), pp. 3721-3731.
34. Liou, K.-N. (1986) 'Influence of Cirrus Clouds on Weather and Climate Processes: A Global Perspective', 114(6), pp. 1167-1199.
35. Liou, K. N., Gu, Y., Yue, Q. and McFarguhar, G. (2008) 'On the correlation between ice water content and ice crystal size and its application to radiative transfer and general circulation models', *Geophysical Research Letters,* 35(13).
36. Marais, W. 2021. UW-Madison High Spectral Resolution Lidar (HSRL) Documentation.
37. Matus, A. V. and L'Ecuyer, T. S. (2017) 'The role of cloud phase in Earth's radiation budget', *Journal of Geophysical Research: Atmospheres,* 122(5), pp. 2559-2578.
38. Menzel, W. P., Frey, R. A., Zhang, H., Wylie, D. P., Moeller, C. C., Holz, R. E., Maddux, B., Baum, B. A., Strabala, K. I. and Gumley, L. E. (2008) 'MODIS Global Cloud-Top Pressure

and Amount Estimation: Algorithm Description and Results', *Journal of Applied Meteorology and Climatology,* 47(4), pp. 1175-1198.

39. Menzel, W. P., Holt, F. C., Schmit, T. J., Aune, R. M., Schreiner, A. J., Wade, G. S. and Gray, D. G. 1998. Application of GOES-8/9 soundings to weather forecasting and nowcasting.
40. Meyer, K., Platnick, S., Holz, R., Dutcher, S., Quinn, G. and Nagle, F. (2020) 'Derivation of Shortwave Radiometric Adjustments for SNPP and NOAA-20 VIIRS for the NASA MODIS-VIIRS Continuity Cloud Products', *Remote Sensing,* 12(24).
41. Miller, S., Stephens, G., Drummond, C., Heidinger, A. and Partain, P. (2000) 'A multisensor diagnostic satellite cloud property retrieval scheme', *Journal of Geophysical Research: Atmospheres,* 105(D15), pp. 19955-19971.
42. Nagaraja Rao, C. R. and Chen, J. (1995) 'Inter-satellite calibration linkages for the visible and near-infared channels of the Advanced Very High Resolution Radiometer on the NOAA-7, -9, and -11 spacecraft', *International Journal of Remote Sensing,* 16(11), pp. 1931-1942.
43. Nakajima, T. and King, M. D. (1989) 'Determination of the Optical Thickness and Effective Particle Radius of Clouds from Reflected Solar Radiation Measurements. Part I: Theory', *Journal of the Atmospheric Sciences,* 47(15), pp. 1878-1893.
44. Pagano, T. S., Ballard, M., De Forrest, A. L., Hudyma, R. M., Julian, R. L. and Tessmer, A. L. 'Development of the Moderate-Resolution Imaging Spectroradiometer (MODIS) protoflight model'. *Optics & Photonics*.

45. Platnick, S., King, M., Ackerman, S., Menzel, W., Baum, B., Riedi, J. and Frey, R. (2003) 'The MODIS cloud products: Algorithms and examples from Terra', 41, pp. 459-473.

46. Platnick, S., Meyer, K., Wind, G., Holz, R. E., Amarasinghe, N., Hubanks, P. A., Marchant, B., Dutcher, S. and Veglio, P. (2021) 'The NASA MODIS-VIIRS Continuity Cloud Optical Properties Products', *Remote Sensing,* 13(1), pp. 28.

47. Platnick, S., Meyer, K. G., King, M. D., Wind, G., Amarasinghe, N., Marchant, B., Arnold, G. T., Zhang, Z., Hubanks, P. A., Holz, R. E., Yang, P., Ridgway, W. L. and Riedi, J. (2017) 'The MODIS Cloud Optical and Microphysical Products: Collection 6 Updates and Examples From Terra and Aqua', *IEEE Transactions on Geoscience and Remote Sensing,* 55(1), pp. 502-525.

48. Prabhakara, C., Fraser, R. S., Dalu, G., Wu, M.-L. C., Curran, R. J. and Styles, T. (1988) 'Thin Cirrus Clouds: Seasonal Distribution over Oceans Deduced from Nimbus-4 IRIS', *Journal of Applied Meteorology,* 27, pp. 379-399.

49. Razenkov, I. 2010. CHARACTERIZATION OF A GEIGER-MODE AVALANCHE PHOTODIODE DETECTOR FOR HIGH SPECTRAL RESOLUTION LIDAR. Ph.D.

50. dissertation, UNIVERSITY OF WISCONSIN-MADISON.

51. Reid, J. S., Maring, H. B., Narisma, G. T., van den Heever, S., Di Girolamo, L., Ferrare, R., Lawson, P., Mace, G. G., Simpas, J. B., Tanelli, S., Ziemba, L., van Diedenhoven, B., Bruintjes, R., Bucholtz, A., Cairns, B., Cambaliza, M. O., Chen, G., Diskin, G. S., Flynn, J. H., Hostetler, C. A., Holz, R. E., Lang, T. J., Schmidt, K. S., Smith, G., Sorooshian, A., Thompson, E. J., Thornhill, K. L., Trepte, C., Wang, J., Woods, S., Yoon, S., Alexandrov, M., Alvarez, S., Amiot, C. G., Bennett, J. R., Brooks, M., Burton, S. P., Cayanan, E., Chen,

H., Collow, A., Crosbie, E., DaSilva, A., DiGangi, J. P., Flagg, D. D., Freeman, S. W., Fu, D., Fukada, E., Hilario, M. R. A., Hong, Y., Hristova-Veleva, S. M., Kuehn, R., Kowch, R. S., Leung, G. R., Loveridge, J., Meyer, K., Miller, R. M., Montes, M. J., Moum, J. N., Nenes, T., Nesbitt, S. W., Norgren, M., Nowottnick, E. P., Rauber, R. M., Reid, E. A., Rutledge, S., Schlosser, J. S., Sekiyama, T. T., Shook, M. A., Sokolowsky, G. A., Stamnes, S. A., Tanaka, T. Y., Wasilewski, A., Xian, P., Xiao, Q., Xu, Z. and Zavaleta, J. (2023) 'The coupling between tropical meteorology, aerosol lifecycle, convection, and radiation, during the Cloud, Aerosol and Monsoon Processes Philippines Experiment (CAMP2Ex)', *Bulletin of the American Meteorological Society*.

52. Sassen, K., Wang, Z. and Liu, D. (2008) 'Global distribution of cirrus clouds from CloudSat/Cloud-Aerosol Lidar and Infrared Pathfinder Satellite Observations (CALIPSO) measurements', *Journal of Geophysical Research: Atmospheres,* 113(D8).
53. Schaaf, C. B., Liu, J., Gao, F. and Strahler, A. H. (2011) 'Aqua and Terra MODIS Albedo and Reflectance Anisotropy Products', pp. 549.
54. Schmit, T. J., Li, J., Li, J., Feltz, W. F., Gurka, J. J., Goldberg, M. D. and Schrab, K. J. (2008) 'The GOES-R Advanced Baseline Imager and the Continuation of Current Sounder Products', 47(10), pp. 2696-2711.
55. Schnaiter, M., Järvinen, E., Vochezer, P., Abdelmonem, A., Wagner, R., Jourdan, O., Mioche, G., Shcherbakov, V. N., Schmitt, C. G., Tricoli, U., Ulanowski, Z. and Heymsfield, A. J. (2016) 'Cloud chamber experiments on the origin of ice crystal complexity in cirrus clouds', 16(8), pp. 5091-5110.

56. Sobel, A. H., Sprintall, J., Maloney, E. D., Martin, Z. K., Wang, S., de Szoeke, S. P., Trabing, B. C. and Rutledge, S. A. (2021) 'Large-Scale State and Evolution of the Atmosphere and Ocean during PISTON 2018', *Journal of Climate,* 34(12), pp. 5017-5035.

57. Stephens, G. L. and Kummerow, C. D. (2007) 'The Remote Sensing of Clouds and Precipitation from Space: A Review', *Journal of the Atmospheric Sciences,* 64(11), pp. 3742-3765.

58. Stephens, G. L., Tsay, S.-C., Stackhouse, P. W., Jr. and Flatau, P. J. (1990) 'The Relevance of the Microphysical and Radiative Properties of Cirrus Clouds to Climate and Climatic Feedback', *Journal of Atmospheric Sciences,* 47, pp. 1742.

59. Turner, D. D. and Eloranta, E. W. (2008) 'Validating Mixed-Phase Cloud Optical Depth Retrieved From Infrared Observations With High Spectral Resolution Lidar', *IEEE Geoscience and Remote Sensing Letters,* 5(2), pp. 285-288.

60. Twomey, S. and Seton, K. J. 1980. Inferences of gross microphysical properties of clouds from spectral reflectance measurements.

61. van Diedenhoven, B., Ackerman, A. S., Fridlind, A. M., Cairns, B. and Riedi, J. (2020) 'Global Statistics of Ice Microphysical and Optical Properties at Tops of Optically Thick Ice Clouds', *Journal of Geophysical Research-Atmospheres,* 125(6), pp. 21.

62. Vermote, E. and Kaufman, Y. J. (1995) 'Absolute calibration of AVHRR visible and near-infrared channels using ocean and cloud views', *International Journal of Remote Sensing,* 16(13), pp. 2317-2340.

63. Waliser, D. E., Li, J.-L. F., Woods, C. P., Austin, R. T., Bacmeister, J., Chern, J., Del Genio, A., Jiang, J. H., Kuang, Z., Meng, H., Minnis, P., Platnick, S., Rossow, W. B., Stephens, G.

L., Sun-Mack, S., Tao, W.-K., Tompkins, A. M., Vane, D. G., Walker, C. and Wu, D. (2009) 'Cloud ice: A climate model challenge with signs and expectations of progress', *Journal of Geophysical Research: Atmospheres,* 114(D8).

64. Walther, A. and Heidinger, A. K. (2012) 'Implementation of the Daytime Cloud Optical and Microphysical Properties Algorithm (DCOMP) in PATMOS-x', *Journal of Applied Meteorology and Climatology,* 51(7), pp. 1371-1390.
65. Walther, A., Straka, W., Heidinger, A.K (2013) *GOES-R Advanced Baseline Imager (ABI) Algorithm Theoretical Basis Document for Daytime Cloud Optical and Microphysical Properties (DCOMP)*.
66. Wang, C., Platnick, S., Zhang, Z., Meyer, K., Wind, G. and Yang, P. (2016) 'Retrieval of ice cloud properties using an optimal estimation algorithm and MODIS infrared observations: 2. Retrieval evaluation', *Journal of Geophysical Research: Atmospheres,* 121(10), pp. 5827-5845.
67. Wielicki, B. A., Young, D. F., Mlynczak, M. G., Thome, K. J., Leroy, S., Corliss, J., Anderson, J. G., Ao, C. O., Bantges, R., Best, F., Bowman, K., Brindley, H., Butler, J. J., Collins, W., Dykema, J. A., Doelling, D. R., Feldman, D. R., Fox, N., Huang, X., Holz, R., Huang, Y., Jin, Z., Jennings, D., Johnson, D. G., Jucks, K., Kato, S., Kirk-Davidoff, D. B., Knuteson, R., Kopp, G., Kratz, D. P., Liu, X., Lukashin, C., Mannucci, A. J., Phojanamongkolkij, N., Pilewskie, P., Ramaswamy, V., Revercomb, H., Rice, J., Roberts, Y., Roithmayr, C. M., Rose, F., Sandford, S., Shirley, E. L., Smith, W. L., Soden, B., Speth, P. W., Sun, W., Taylor, P. C., Tobin, D. and Xiong, X. (2013) 'Achieving Climate Change Absolute Accuracy in Orbit', 94(10), pp. 1519-1539.

68. Wind, G., Platnick, S., Meyer, K., Arnold, T., Amarasinghe, N., Marchant, B. and Wang, C. X. (2021) 'The CHIMAERA system for retrievals of cloud top, optical and microphysical properties from imaging sensors', *Computers & Geosciences,* 149, pp. 7.

69. Xiao, H., Zhang, F., He, Q., Liu, P., Yan, F., Miao, L. and Yang, Z. (2019) 'Classification of Ice Crystal Habits Observed From Airborne Cloud Particle Imager by Deep Transfer Learning', *Earth and Space Science,* 6(10), pp. 1877-1886.

70. Yang, P., Bi, L., Baum, B. A., Liou, K.-N., Kattawar, G. W., Mishchenko, M. I. and Cole, B. (2013) 'Spectrally Consistent Scattering, Absorption, and Polarization Properties of Atmospheric Ice Crystals at Wavelengths from 0.2 to 100 μm', *Journal of the Atmospheric Sciences,* 70(1), pp. 330-347.

71. Yang, P., Wei, H. L., Huang, H. L., Baum, B. A., Hu, Y. X., Kattawar, G. W., Mishchenko, M. I. and Fu, Q. (2005) 'Scattering and absorption property database for nonspherical ice particles in the near- through far-infrared spectral region', *Applied Optics,* 44(26), pp. 5512-5523.

72. Zhang, Y., Macke, A. and Albers, F. (1999) 'Effect of crystal size spectrum and crystal shape on stratiform cirrus radiative forcing', 52(1), pp. 59-75.

73. Zhang, Z. B., Platnick, S., Yang, P., Heidinger, A. K. and Comstock, J. M. (2010) 'Effects of ice particle size vertical inhomogeneity on the passive remote sensing of ice clouds', *Journal of Geophysical Research-Atmospheres,* 115, pp. 16.

Appendix

A. List of Equations and Symbols

Visible retrieval Theory Equations

Symbols

R : Reflection function observed at the sensor

R_{atm}Reflectance function of the atmosphere as a function of τ_c

R_c: Reflectance function of the cloud

R_∞: Reflection function of a semi-infinite atmosphere

A_g: Surface albedo in accordance with Lamberts law

A_v: Virtual surface albedo parameter

$\overline{r_{atm}}$: Spherical Albedo of Atmosphere as a function of τ_c

S: Cloud Albedo

t_{atm}: Transmission of the atmosphere as a function of τ_c

τ_c : Cloud Optical Thickness

μ_o: cosine of the solar zenith angle

μ: absolute value of the cosine of the solar zenith angle

ϕ: relative azimuth angle

K: Escape Function

g: Asymmetry Parameter

q_o: Extrapolation length for conservative scattering

R_e: Equivalent reflectance value

- $R(\tau_c,\ \mu\,\mu_o,\phi) =\ R_{atm}(\tau_c,\ \mu\,\mu_o,\phi) + \frac{\boldsymbol{A_g}}{1-\boldsymbol{A_g}\overline{r_{atm}}(\tau_c)}\, t_{atm}(\tau_c,\mu)\ t_{atm,o}(\tau_c,\mu_o)$
- $R_{atm}(\tau_c,\ \mu\,\mu_o,\phi)\ = R_{\infty}(\mu\,\mu_o,\phi) - \frac{4K(\mu)K(\mu_o)}{3(1-g)(\tau_c+2q_o)}$
- $t_{atm}(\tau_c;\mu\,\mu_o,\phi) =\ \frac{4K(\mu)K(\mu_o)}{3(1-g)(\tau_c+2q_o)}$
- $F(x) = R_c(x) + \frac{A_v t_{atm,o}(x) t_{atm}(x)}{1-A_v S(x)} + R_e(x)$

Citations: Walther and Heidinger 2012, King et al. 1987

Infrared Retrieval Equations

Symbols

I_{calc}: Top of the atmosphere spectral radiances

I_{clr}: Clear sky radiances (surface contribution)

I_{ac}: Above cloud radiance contribution

ϵ_c: Emissivity of the cloud

$B(T_c)$: Emitted radiances by the cloud from the Planck function

τ_{vis} : Optical depth as visible wavelength

σ_{vis}: Extinction coefficient at the visible wavelength

$\sigma_{11\mu m}$: Extinction coefficient at 11 μm

$\omega_{11\mu m}$: Single scattering albedo at 11μm

$g_{11\mu m}$: Asymmetry parameter at 11μm

- $I_{calc} = \epsilon_c I_{ac} + T_{ac}\epsilon_c B(T_c) + I_{clr}(1 - \epsilon_c)$
- $\tau_{vis} = \frac{\sigma_{vis}}{\sigma_{11\mu m}}\left[\frac{-\mu ln\,(1-\epsilon_C)}{1-\omega_{11\mu m}g_{11\mu m}}\right]$

Citations: Heidinger and Pavolonis 2009, Heidinger 2015

HSRL Equations

Basic Principles

Symbols

P : Received power

E_o: Laser Pulse energy

c : Speed of light

A_r: Collection area of receiver

R : Range to scattering vol ume

β_a : Aerosol back scattering cross section

β_m : Molecular back scattering cross section

$\frac{P(\pi,r)}{4\pi}$: Backscatter phase function

$\frac{3}{8\pi}$: Molecular backscatter phase function

$\tau(r)$: Optical thickness

S_m: Molecular signal

r: Range of target

ρ: Atmospheric density

- $P(r) = E_o \frac{cA_r}{2r^2}(\beta_a(r)\frac{P(\pi,r)}{4\pi} + \beta_m(r)\frac{3}{8\pi})e^{-2\tau(r)}$
- $\tau = \int_0^r \beta_e(r)dr$
- $P_m(r) = E_o \frac{cA_r}{2r^2}\beta_m(r)\frac{3}{8\pi}e^{-2\tau(r)}$
- $P_a(r) = E_o \frac{cA_r}{2r^2}\beta_a(r)\frac{P(\pi,r)}{4\pi}e^{-2\tau(r)}$

- $\beta_m = C\rho(r)$
- $S_m(r) = \frac{P_m(r)\, r^2}{E_o}$
- $\tau(r) - \ \tau(r_o) = \frac{1}{2} ln(\frac{\rho(r)}{\rho(r_o)}) - \frac{1}{2} ln(\frac{S_m(r)}{S_m(r_o)})$
- $\tau = \ \int_0^r \beta_e(r) dr$
- $R(r) = \frac{P_a(r)}{P_m(r)}$
- $\beta_a(r) \frac{P(\pi,r)}{4\pi} = R(r)\beta_m(r) \frac{3}{8\pi}$

Citations: https://lidar.ssec.wisc.edu/

Calibration of HSRL Data

Symbols

$N_{corrected}$: After pulse corrected photon counts for a given channel

N_{total}: Total n umber of photon counts measured for a given channel

$N_{baseline}$: Baseline correction

$N_{background}$: Background correction

N_{mol}: N umber of molecular photon counts

N_a: N umber of aerosol photon counts

S_{cmb}: Signal in the combined channel

S_{mol}: Signal in the molecular channel

C_{am}: Corrects for the leakage of aerosol photons that are not removed by the iodine filter

C_{mm}: Corrects for the attenuation of the molecular photons through the iodine filter

C_{ac}: Relative contribution of the aerosol onto the combined channel

C_{mc}: Relative contribution of molecules onto the combined channel

- $N_{corrected} = N_{total} - N_{baseline} - N_{background}$
- $S_{mol} = C_{am}N_a + C_{mm}N_{mol}$
- $S_{cmb} = C_{ac}N_a + C_{mc}N_{mol}$
- $N_{mol} = \frac{S_{mol} - S_c C_{am}}{C_{mm} - C_{am}C_{mc}}$
- $N_a = \frac{S_{cmb}C_{mm} - S_m C_{mc}}{C_{mm} - C_{am}C_{mc}}$

Citations: Razenkov 2010, Marias 2021

Geophysical Parameters

Symbols

δ_p: Particulate depolarization ratio

N_{pol}: N umber of photon counts in cross-polarization channel

G: Combined to cross polarization gain ratio

v_a: particulate backscatter cross-section

S_{pol}: Signal in the cross-polarization channel

S_{cmb}: Signal in the combined channel

C_0: Polarization cross talk

δ_m: Molecular depolarization

$v_{mol}^{\|}$: molecular backscatter

0: Geometric overlap function

μ: Mean

σ: Standard deviation

τ_{abv_cld}: Photon averaged optical depth above cloud

τ_{cbh}: Lowest optical depth of cloud

- $\delta_p = \frac{N_{pol}}{N_{cmb}}$
- $N_{pol} = G\left(S_{pol} - C_0 S_{cmb}\right) - C_{mc} N_{mol} \delta_m$
- $v_a = \frac{v_{mol}^{\|}(N_{cmb} C_{mm} - N_{mol} C_{mc})}{N_{mol} - N_{cmb} C_{am}} (1 + \delta_p)$

- $\tau = -\frac{1}{2}\log(\frac{(N_{cmb}C_{am}-N_{mol})r^2}{0v_{mol}^{\parallel}(C_{am}C_{mc}-C_{mm})e^{-2t_m}})$
- $SNR = \frac{\mu}{\sigma}$
- $\sigma(N) = \sqrt{N}$
- $\sigma(v_a)^2 = \sqrt{\left(\frac{\partial v_a}{\partial N_{cmb}}\right)^2 \sigma(N_{cmb})^2 + \left(\frac{\partial v_a}{\partial N_{mol}}\right)^2 \sigma(N_{mol})^2 + \left(\frac{\partial v_a}{\partial N_{pol}}\right)^2 \sigma(N_{pol})^2}$
- $SNR_{part} = \frac{v_a}{\sigma(v_a)}$
- $\tau_{abv\_cld} = -\frac{1}{2}\log(\frac{mean(r^2(N_{cmb}C_{am}-N_{mol})[cth{:}atten\_level])}{mean(0v_{mol}^{\parallel}(C_{am}C_{mc}-C_{mm})e^{-2t_m}\,[cth{:}atten\_level])})$
- $IOT = \tau_{abv\_cld} - \tau_{cbh}$

Citations: Holz 2002; Marais 2021

B. List of Acronyms

ABI - Advanced Baseline Imager

ACCP - Aerosols Clouds Convection Precipitation

AHI - Advanced Himawari Imager

AIRS - Atmospheric Infrared Sounder

AOS - Atmospheric Observing System

APDs - Avalanche Photodiodes

AVHRR - Advanced Very High-Resolution Radiometer

BRDF - Bidirectional Reflectance Distribution Function

CALIPSO - Cloud-Aerosol LIDAR and Infrared Pathfinder Satellite Observations

CAMP2EX - Cloud-Aerosol and Monsoon Process Philippines Experiment

CER - Effective Radius

CrIS - Cross-track Infrared Sounder

COT - The Cloud Optical Thickness

DARDAR - CloudSat Data Processing Center and Radar/Lidar Product

DISTORT - Discrete Ordinates Radiative Transfer Model

ECM - Enterprise Cloud Mask

FMA - Four Mirror Anastigmat

FPM - Focal Plane Modules

GCMs - Global Climate Models

GEO - Geostationary Earth Orbit

HSRL - High Spectral Resolution Lidar

ICOTR - Ice Cloud Optical Thickness Retrieval

IOT - Ice Cloud Optical Thickness

IRIS - Infrared Inter-ferrometer Spectrometer

ITCZ - Inter-Tropical Convergence Zone

LEO - Low Earth Orbit

MODIS - Moderate Resolution Imaging Spectroradiometer

NASA CLDPROP - NASA Cloud Property Algorithm

PISTON - Propagation of Intra-Seasonal Tropical Oscillations

SIPS - Science Investigator-led Processing System

TOA - Top of the Atmosphere

VIIRS - Visible Infrared Imaging Suite